



THE UNIVERSITY *of* EDINBURGH

This thesis has been submitted in fulfilment of the requirements for a postgraduate degree (e.g. PhD, MPhil, DClinPsychol) at the University of Edinburgh. Please note the following terms and conditions of use:

This work is protected by copyright and other intellectual property rights, which are retained by the thesis author, unless otherwise stated.

A copy can be downloaded for personal non-commercial research or study, without prior permission or charge.

This thesis cannot be reproduced or quoted extensively from without first obtaining permission in writing from the author.

The content must not be changed in any way or sold commercially in any format or medium without the formal permission of the author.

When referring to this work, full bibliographic details including the author, title, awarding institution and date of the thesis must be given.

Development of Micro and Nano Resonators for Acoustic Sensing Applications

by

Asaad Kareem Edaan Al-mashaal



A thesis submitted for the degree of Doctor of Philosophy

Institute for Integrated Micro and Nano Systems

School of Engineering

The University of Edinburgh

2018

Abstract

Suspended vibrating structures play a significant role as basic building blocks for mechanical resonators and form the foundation of modern acoustic transducers. The practical use of mechanical resonators is not limited to acoustic technology but also includes a wide range of applications for sensing and actuation purposes. The ultimate goal of this project has been set to realise highly tunable and sensitive resonators that have operating frequencies covering the audible range (20 Hz – 20 kHz). In this thesis, two distinct types of mechanical resonators have been developed, dedicated mainly to hearing assistive devices and acoustic microphones. The overall performance of mechanical resonators is governed by their structural elements design, material properties, and dimensions. Inspired by their unique mechanical properties, a refractory metal of tantalum and a two-dimensional (2D) material of graphene have been utilised as vibrating structural elements for the developed resonators.

In the first parts of this project, mechanical resonators of tantalum tunable to audio frequencies have been developed. First, a comprehensive investigation of the influence of fabrication process parameters on the residual stress of tantalum thin-films has been implemented. Based on the residual stress characterisation, an array of suspended microbeams of tantalum has been created and their mechanical static deflection has been investigated. Accordingly, the design and fabrication process of the resonators have been optimised, and hence straight and undeformed free-standing microbeams with lengths of 1 – 3.4 mm have been created and actuated electrostatically. The resonators have achieved a low resonant frequency (1.4 kHz) tuned over the audio range. Unlike the conventional microphones that have their vibrating membranes made of stressed and stiff materials, the graphene-based resonators developed here from ultra-large and thin bilayer membranes have the advantages of possessing enhanced durability and high frequency tuning sensitivity. A simple and reproducible fabrication process has been demonstrated to create millimetric membranes composed of a multilayer graphene and a thin polymeric film. The novelty of the developed resonators lies in the exceptional area to thickness aspect ratios of $\sim 10,000$, and the implementation of electrothermal actuation to drive the membranes into resonance and tune their resonant frequencies.

Lay summary

An acoustic transducer is an instrument that converts a sound signal into an electrical output. Microphones and hearing assistive devices are the best examples of acoustic transducers. Most of the current hearing assistive devices such as conventional hearing aids and cochlear implants contain a microphone as an external component. In real life applications, the commercially-available acoustic transducers suffer from a number of problems that can influence their practical usability. Some of these common problems are related to the device performance such as low sensitivity, high power consumption, frequent recharging, background noise, feedback-cancellation effects and unstable operating frequency range. There are also some other issues associated with the device production such as design complexity, large size, damage, limited material selection, and high cost. For example, the large size of hearing aids components introduces social stigma as well as reliability concerns for users. Although there has been intensive research dedicated to addressing some of these mentioned problems, each effort has its own merits and drawbacks. For instance, size reduction of microphones and other acoustic transducers can be achieved at the expense of high background noise and high frequency response, which make such device unsuitable for real acoustic applications. Therefore, any practical attempt to improve the device performance and optimise its characteristics further is considered to be of great interest.

This research aims to develop transducers that can be used effectively for hearing aids and microphone-like devices. The first feature that this thesis aims to achieve for the developed mechanical resonators is to operate at low frequencies within the audio range (20 Hz – 20 kHz). Therefore, the focus of this work has been directed mainly on optimising the resonator design, selecting proper materials, improving the fabrication process and characterising the devices outputs. Simplicity is the attribute that marks the design of the developed resonators. Instead of using fragile, stressed and relatively thick materials such as that used in traditional microphones, a stress controlled metal of tantalum and a flexible low-dimensional semimetal of graphene have been chosen to act as the vibrating structures of the resonators. Attempts have been made to tackle issues such as stress and graphene transfer. It is hoped that the resonators developed here could contribute positively to produce more reliable acoustic transducers.

Declaration of originality

I hereby declare that research work described and reported in this thesis has been composed and originated entirely by myself in the Institute for Integrated Micro and Nano Systems, School of Engineering, The University of Edinburgh.

Asaad Kareem Edaan Al-mashaal

Acknowledgements

I would like to express my thanks and gratitude to all those people who contributed in many ways to the success of my project and made this thesis possible. First of all, I would like to thank my supervisor, Professor Rebecca Cheung, for the encouragement, thoughtful guidance and immense support throughout the last four years of my PhD. I also would like to thank my assistant supervisor Dr Enrico Mastropaolo for his valuable recommendations, discussion and technical advice on device fabrication and measurement. I greatly acknowledge the financial support of the Iraqi Ministry of Higher Education and Scientific Research (MOHESR) for granting me a PhD scholarship without which the work presented in this thesis would not have been accomplished.

I am deeply thankful to all fellow PhD students, research, academic and administrative staff of the Scottish Microelectronics Centre for their positive support and help during my PhD journey in Edinburgh. I would like to thank the technical support team of the cleanroom, Dr Andrew Bunting, Dr Peter Lomax, Dr Camelia Dunare, Richard Blair, Stewart Ramsay, Ewan MacDonald and Brian Neilson for their help, advice, support and training. I must also acknowledge all the help I received from Dr Graham Wood, Dr Alberto Torin and Dr Michael Newton during my work with them on the GMAAT project. Particular thanks must be given to my colleagues Rui Zhang, Hanning Mai, Chandrasekaran Gunasekaran, Nadira Jamil, Rui Song, Karina Jeronimo, Anthony Bulling, Noor Amalina, Riza Bashri, Atif Syed, Tarek Al Abbas and Zaki Hussein for their continuous support and valuable friendship. A big thank

you is due to Dr Daniel Drysdale for his help using MEMSSTAR tools to fabricate my devices.

Finally, and most importantly, I would like to express my wholehearted gratitude and special thanks to my lovely wife, Zahraa, for her unconditional support and continued encouragement. My dearest daughter, Jana, you are the greatest blessing of my life. Restarting my laptop, your beautiful smile and your funny video calls while I was working have just made my PhD an unforgettable experience. My acknowledgement would be incomplete without thanking the biggest source of my strength, my family: my parents, my brothers, my sisters, nephews, and nieces.

Dedication

This thesis is dedicated to whom I owe everything

My Parents

My Wife

My Daughter

My Brothers

My Sisters

For their unconditional love, support, company and encouragement

Publications

Parts of the contents of this thesis have been published in peer-reviewed journals:

1. **Asaad K. Al-mashaal**, G. S. Wood, A. Torin, E. Mastropaolo, M. J. Newton, R. Cheung, “Tunable Graphene-Polymer Resonators for Audio Frequency Sensing Applications ,” *IEEE Sensors Journal*, vol. pp, issue 99, 2018.
2. **Asaad K. Al-mashaal**, G. S. Wood, E. Mastropaolo, and R. Cheung, “Electrostatically driven long-microbeams for low-frequency applications,” *Electron. Lett.*, vol. 54, no. 6, pp. 372–374, 2018.
3. **Asaad K. Al-mashaal**, G. S. Wood, A. Torin, E. Mastropaolo, M. J. Newton, and R. Cheung, “Dynamic behavior of ultra large graphene-based membranes using electrothermal transduction,” *Appl. Phys. Lett.*, vol. 111, no. 24, p. 243503, 2017.
4. **Asaad K. Al-mashaal**, E. Mastropaolo, A. Bunting, C. Dunare, and R. Cheung, “Fabrication and characterisation of suspended microstructures of tantalum,” *J. Micromechanics Microengineering*, vol. 27, no. 1, p. 015020, 2017.

5. **Asaad K. Al-mashaal**, A. Bunting, and R. Cheung, “Evaluation of residual stress in sputtered tantalum thin-film,” *Appl. Surf. Sci.*, vol. 371, pp. 571–575, 2016.
6. Luca Camellini, A. Torin, **Asaad K. Al-mashaal**, G. S. Wood, M. Newton, R. Cheung, and E. Mastropaolo, “Fabrication and modal characterisation of large-area polymer membranes for acoustic MEMS devices,” *Micro Nano Lett.*, 2018.

Glossary

Acronyms and Abbreviations

ABMs	Artificial Basilar Membranes
AFM	Atomic Force Microscopy
BHF	Buffered Hydrofluoric Acid
BM	Basilar Membrane
CC	Clamped-Clamped
CI	Cochlear Implants
CMOS	Complementary Metal-Oxide-Semiconductor
CTE	Coefficient of Thermal Expansion
FEA	Finite Element Analysis
FFT	Fourier Transform
IC	Integrated Circuit
LDV	Laser Doppler Vibrometer
MDOF	Multi Degree-Of-Freedom
MEMS	Microelectromechanical Systems
NEMS	Nanoelectromechanical Systems
PECVD	Plasma-Enhanced Chemical Vapour Deposition
PI	Polyimide
PMMA	Poly(Methyl Methacrylate)
RF	Radio Frequency
RGTs	Resonant Gate Transistors
RIE	Reactive Ion Etching
SDOF	Single-Degree-Of-Freedom
SEM	Scanning Electron Microscopy
SNR	Signal to Noise Ratio
WHO	The World Health Organization

Variables and Constants

D	Bending Rigidity
σ_{cr}	Critical Stress
A	Cross-Sectional Area
I	Cross-Sectional Moment of Inertia
ζ	Damping Ratio
M_{eff}	Effective Mass
K_{eff}	Effective Stiffness
C_{eff}	Effective Total Losses
\hat{E}	Effective Young's Modulus
E	Elastic Modulus
P_c	Euler Buckling Limit
l	Length
ρ	Mass Density
ω_{res}	Natural Resonant Frequency
ε_0	Permittivity of Free Space
V_{PI}	Pull-In Voltage
Q	Quality Factor
R	Radius of Circular Membrane
f_n	Resonant Frequency
a	Side Length of Square Membrane
σ	Stress
ΔT	Temperature Gradient
N	Tension
τ	Thermal Response Time
t	Thickness
w	Width
d_0	Zero-Voltage Gap

Contents

Abstract	I
Lay summary	II
Declaration of originality	III
Acknowledgements	IV
Dedication	VI
Publications	VII
Glossary	IX
1 Introduction	1
1.1 Electromechanical systems	1
1.2 Motivation of research	5
1.3 Research aim	6
1.3.1 Research objectives	7
1.4 Thesis organisation	10
2 Literature Review, Design and Actuation of Resonators	11
2.1 Introduction	11
2.2 Acoustic transducers: literature review	11
2.2.1 MEMS for hearing assistive systems	12
2.2.2 MEMS microphones for audio applications	15
2.3 Mechanical resonator	18
2.3.1 Discrete model	18

2.3.2	Continuous model: Euler-Bernoulli beam	22
2.4	Tantalum-based resonators	25
2.4.1	Design of tantalum beams	25
2.4.2	Why tantalum?	28
2.4.3	Influence of beam geometry on resonant frequency	30
2.5	Graphene-based resonators	32
2.5.1	Why graphene?	32
2.5.2	Resonant frequency of membranes and plates	32
2.5.3	Influence of film geometry on resonant frequency	34
2.6	Electrostatic actuation of tantalum beams	37
2.7	Actuation of graphene-based resonators	40
2.7.1	Electrothermal actuation of graphene-PMMA	42
2.8	Summary	45

3 Fabrication and Characterisation of Tantalum

Structures		47
3.1	Introduction	47
3.2	Thin film stress	48
3.2.1	Residual stress of tantalum thin film	52
3.3	Fabrication of tantalum thin-films	53
3.4	Characterisation of tantalum thin-films	55
3.4.1	Stress measurement procedure	56
3.4.2	Effect of sputtering pressure and power	56
3.4.3	Effect of annealing in oxygen ambient	58
3.4.4	Effect of atmospheric exposure	60
3.4.5	Effect of Argon energy exposure	63
3.5	Suspended beams of tantalum	66
3.5.1	Stress-related deflection	67

3.5.2	Beams fabrication procedure	69
3.6	Beams Characterisation	72
3.6.1	Deflection measurements	72
3.6.2	Initial residual stress measurement	74
3.6.3	Model description: mechanical static analysis	76
3.6.4	Effect of initial film stress	81
3.6.5	Effect of etch release process	83
3.6.6	Effect of beam dimension	85
3.7	Summary	90
4	Dynamics of Tunable Tantalum-based Resonators	92
4.1	Introduction	92
4.2	Design of tantalum-based resonators	93
4.3	Fabrication of ultralong-beams of tantalum	94
4.4	Characterisation of fabricated structures	96
4.5	Mechanical dynamics of fabricated beams	98
4.5.1	Resonant frequency of tantalum beams	99
4.5.2	Resonant frequency of stressed-beam resonators	101
4.5.3	Pull-in voltage analysis	105
4.5.4	Frequency tuning: experimental measurements	110
4.6	Summary	114
5	Properties and Transfer Challenges of Graphene	115
5.1	Introduction to graphene	115
5.2	Properties of graphene	117
5.2.1	Electrical properties of graphene	118
5.2.2	Mechanical properties of graphene	119
5.2.3	Thermal properties of graphene	120
5.3	Fabrication of graphene films	120

5.3.1	Graphene on shallow cavities: Wet transfer . .	121
5.3.2	Graphene on shallow cavities: dry transfer . .	132
5.4	Graphene transfer challenges	135
5.4.1	Optimisation of graphene transfer and design	136
5.4.2	Post-fabrication characterisation	139
5.5	Summary	141
6	Fabrication and Characterisation of Tunable Graphene Resonators	143
6.1	Introduction	143
6.2	Fabrication procedure of large resonators of graphene-PMMA	144
6.2.1	Preparation of target substrate	146
6.2.2	Transfer of graphene-PMMA films	147
6.2.3	Post-transfer characterisation	149
6.3	Dynamics of graphene-PMMA resonators	149
6.3.1	Measurements setup	150
6.3.2	Effect of actuation configuration	151
6.3.3	Effect of film thickness	158
6.3.4	Analysis of membrane and plate	160
6.4	Tuning of graphene-PMMA resonators	165
6.4.1	Frequency tuning: circular and square membranes	167
6.4.2	Tuning sensitivity	172
6.5	Summary	177
7	Conclusions and Scope of Future Work	179
7.1	Tantalum-based Resonators	179
7.2	Graphene-based Resonators	182

7.3 Scope of future work 185

7.3.1 Design of resonant element 186

7.3.2 Graphene microphone 186

Bibliography **188**

Chapter 1

Introduction

In this chapter, a brief description of devices based on electromechanical systems and their potential applications will be given. Acoustic technologies of hearing assistive devices and modern microphones will be presented as a motivation for the research provided in this thesis. The development of mechanical resonators based on tantalum metals and graphene membranes will be stated in the aim and objectives section of this chapter. Finally, the outline of the thesis will be provided.

1.1 Electromechanical systems

The desire to explore our world has led to unlimited innovations that help in finding solutions to a number of problems and challenges we face in our daily lives. These innovations have been reflected realistically in the ongoing development of technology that has affected every aspect of life, making it better and easier than ever before. Practically, technology has been formed into different kinds of devices that have found their way into real-life applications. Miniaturisation, a general trend of making ever smaller devices, is one of the fastest growing technologies that has revolutionised the shape of our modern life. In addition, decades of intense

research in solid-state electronics and materials have paved the way to significant advancement in integrated circuit (IC) technology.

With the advances in miniaturisation technology, the feature size of transistors has been shrunk to a few nanometres, following the well-known prediction of Gordon Moore (i.e. Moore's law) [1] who expected a double increase in the transistor density of integrated circuits every two years. Compared to the 7-nm node technology in 2018, the downscaling of transistors is expected to reach the 2.5-nm and 1.5-nm nodes in 2027 and 2030, respectively [2]. The achievement of miniaturisation technology has revolutionised the size of electronic devices, leading to the practical use of these devices in more convenient ways. For example, billions of modern silicon transistors can now be packed into a fingernail-sized chip. The shrinking of transistors has lead to the scaling down of room-sized computers into small units such as laptops and mobile phones.

In fact, the progress of miniaturisation technology and the key role of the semiconductor industry in developing batch-fabrication techniques to produce a diverse set of devices in very small sizes have given rise to the well-known field of microelectromechanical systems (MEMS) [3]. In general, MEMS are devices and systems that consist of electrical and mechanical components, with typical dimensions ranging from several micrometres to hundreds of micrometres. Despite the fact that the majority of MEMS devices have moving parts, there are many other devices that have no moving elements at all [4]. The motion of moving components in MEMS devices is usually actuated or detected using electrical signals. Scanning electron microscopy (SEM) images of some examples of MEMS devices are shown in [Figure 1.1](#).

Today, the practical use of MEMS devices is increasing enormously and covers a wide range of applications, including

optical switches for data communications, accelerometers for airbag deployment, mirror arrays for displays, radio frequency (RF) switches for wireless communications, electromechanical actuators, tunable filters, inkjet printing heads, electromechanical resonators and an enormous diversity of sensors. As all modern technological sectors step forward rapidly, the demand for smaller devices is becoming ever stronger. The progress of miniaturisation technology and monolithic integration of MEMS and complementary metal-oxide-semiconductor (CMOS) processes has led to the production of small devices within the nanoscale. The systems and devices with critical dimensions between 100 and 1 nm are called nanoelectromechanical systems (NEMS) [5].

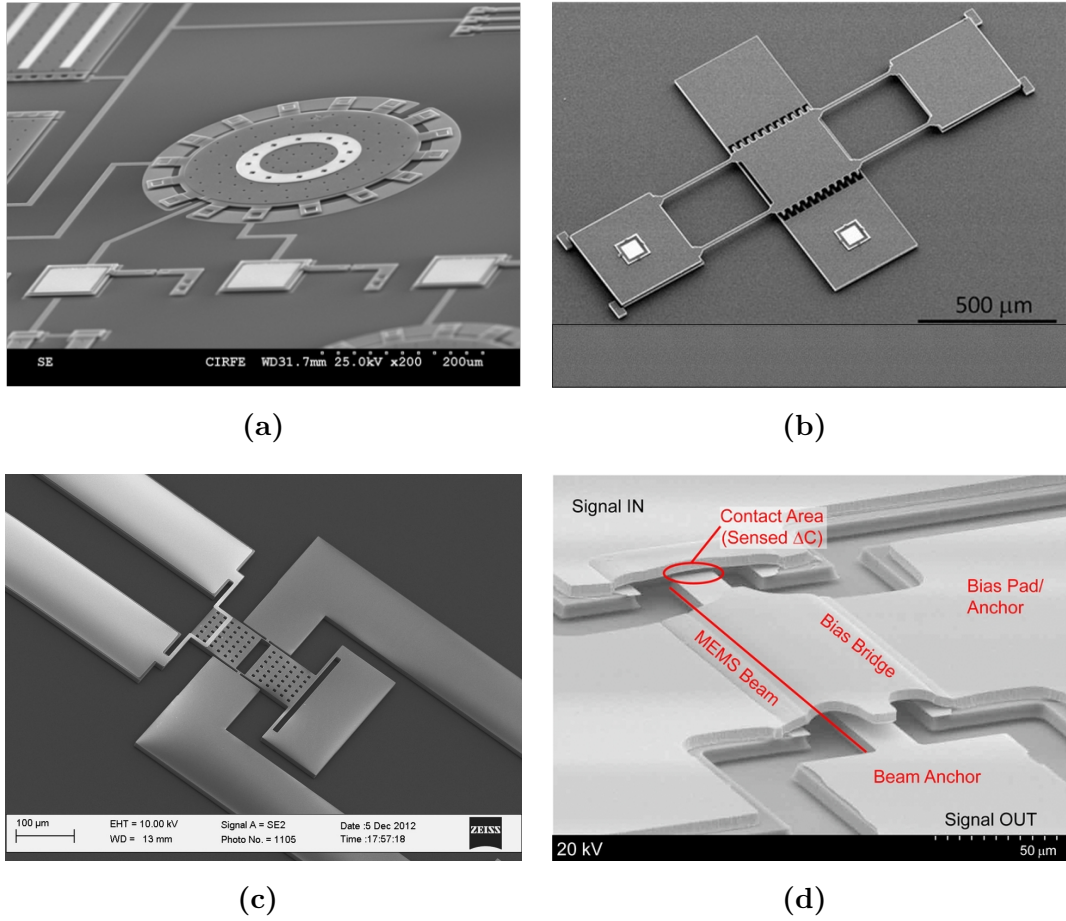


Figure 1.1: SEM images of MEMS devices. (a) Temperature sensor based on membrane structure. Image taken from [6]. (b) Capacitive actuator/sensor based on two comb drive microstructures. Image taken from [7]. (c) Thermally actuated resonant sensor. Image taken from [8]. (d) RF switch. Image taken from [9].

Although the NEMS field is still facing many technological challenges associated with fabrication and packaging, NEMS devices have already made their way into a variety of applications such as mass/force sensors, biological sensors, signal processing components and a host of resonators and actuators. SEM images of some examples of NEMS resonators based on silicon are shown in Figure 1.2.

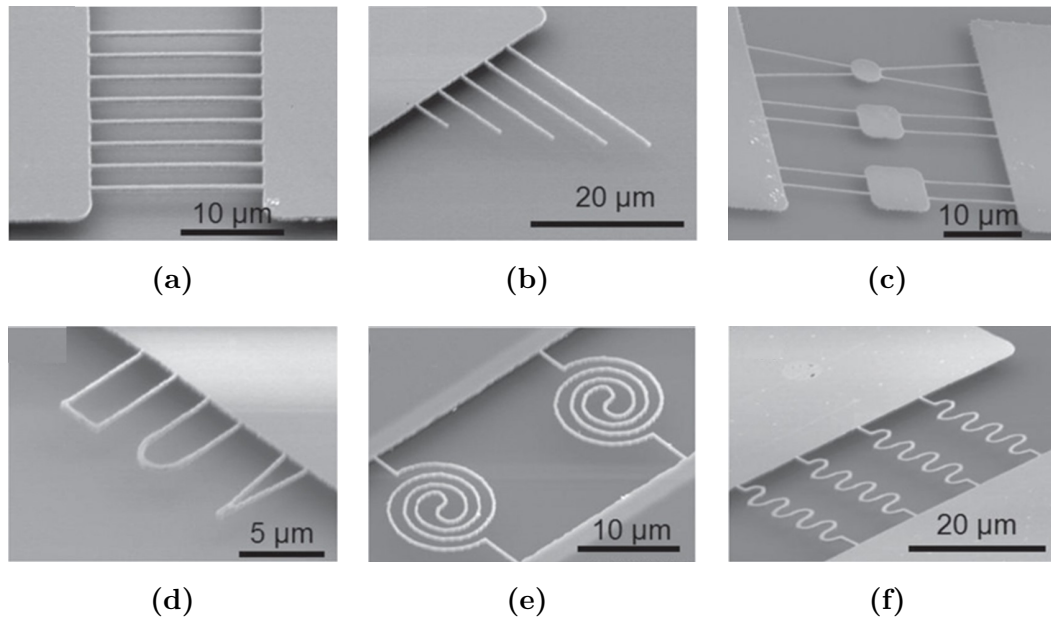


Figure 1.2: SEM images of several silicon-based NEMS resonators with a thickness of 400 nm and different geometrical layouts. **(a)** Clamped-clamped resonators with a length of 18 μm and a width of 500 nm. **(b)** Clamped-free resonators with lengths ranging from 5 to 20 μm . **(c)** Spider-like resonators with different pads (the beam width is 500 nm while the pad size is 4.3 μm). **(d)** Double-armed with different shapes resonators with a width of 500 nm. **(e)** Spiral-shaped resonators with a width of 300 nm. **(f)** Serpentine-shaped clamped-clamped resonators with a width of 500 nm. Images taken from [10].

1.2 Motivation of research

Although every device based on MEMS/NEMS performs a specific function, resonance is the common phenomenon of devices that involve moveable components. A device with moveable parts that vibrates in response to a stimulus is called a resonator. In short, a MEMS-based mechanical resonator can be used as an acoustic transducer when its integrated mechanical and electrical components work together to convert mechanical signals into electrical signals or vice versa. Unlike quartz-based resonant elements, MEMS resonators have the advantages of being batch-fabricated at low cost and can be integrated with other electronics components [11]. Since the first introduction of the

resonant gate transistor by Nathanson et al. [12], MEMS-based micro resonators have received growing interest from the scientific community and industrial sectors.

An important parameter associated with mechanical resonators is their operating frequency range. Typically, the resonant frequencies of micro resonators are in the kHz to MHz range [11]. However, as device size reduces to the nanoscale, the resonant frequencies can reach the GHz range [13–15]. Other parameters that seem of great importance for some applications are frequency tunability and tuning sensitivity of the resonator. In hearing aids devices, for example, the resonant elements have to be designed in such a way that the audio frequency range (20 Hz – 20 kHz) is covered fully. In other words, the resonators are required to be tunable to the audio frequencies with a sufficient sensitivity.

One possible way to cover the entire audible frequency range is to make an array of resonant structures with different dimensions [16–22], so that each individual structure vibrates at a certain frequency band. To cover the low band of audio range (2 Hz – 5 kHz), the length (area) of the vibrating structures should be increased. From the fabrication point of view, making large suspended structures is challenging, as effects of residual stress and fabrication processes on the intrinsic mechanical properties of the resonator’s material are somewhat difficult to control. Also, the tunability feature of a resonator can be achieved by using a proper actuation mechanism. For example, the majority of currently available MEMS microphones [23–25] rely on capacitive-type transduction.

1.3 Research aim

The main goal of this research is to develop electromechanical transducers for audio frequency applications. The contribution of

this project includes the design, fabrication and characterisation of two different mechanical resonators. The first resonators are based on doubly clamped microbeams made from tantalum metal, while the second resonators are made from thin and flexible circular and square membranes of graphene. Motivated by their promising properties, tantalum and graphene have been chosen as structural components for the developed resonators. The developed resonators are dedicated to hearing assistive devices to hearing assistive devices, microphones and other acoustic transducers.

1.3.1 Research objectives

This research contributes to the progress of developing MEMS mechanical resonators for audio applications by employing suspended structures of microbeams of tantalum and flexible membranes of graphene. The main objectives of this thesis are provided schematically in [Figure 1.3](#). The design of tantalum mechanical resonators is based on an array of clamped-clamped (CC) microbeams. Tantalum has been chosen as a vibrating structural element due to its high melting point, corrosion-resistance, high fracture toughness and low ratio of Young's modulus to mass density. To achieve low frequency within the audible range, the length to thickness aspect ratio should be maximised. However, it is extremely challenging to make straight structures from long and thin beams without controlling the fabrication process effects and optimising the resonator's design. Therefore, the first part of this thesis is devoted to the optimisation of the fabrication process by studying the effect of deposition conditions on the residual stress developed in the deposited thin-films and suspended beams of tantalum metal. The mechanical static behaviour of tantalum beams will be examined optically to evaluate the influence of the etching release process and

initial residual stress on the final deflection profile of the beams. In addition, the design of the resonators will be optimised further in such a manner that a large bottom actuation electrode will be included, hence electrostatic transduction will be used as an operating mechanism.

Another developed resonator is based on atomically-thin films of the two-dimensional (2D) material of graphene. Graphene has unique mechanical properties such as large Young's modulus, low mass density and very high mass sensitivity that would make it a promising material for highly sensitive acoustic transducers. In addition to its strength, graphene has a special stretching capacity of 20 – 25 % of its length. Such resonators made of graphene and supported by a polymeric thin-film can be considered as potential structures for the development of more sensitive artificial hearing aids and modern microphones. Instead of using thick and stressed materials such as that in conventional acoustic transducers, the use of structural elements made of an ultra-thin, lightweight and durable membrane of graphene would have the benefits of achieving an improved spectral response with high sensitivity. Moreover, a simple design has been proposed and optimised to enable the graphene-based membranes to be actuated electrothermally.

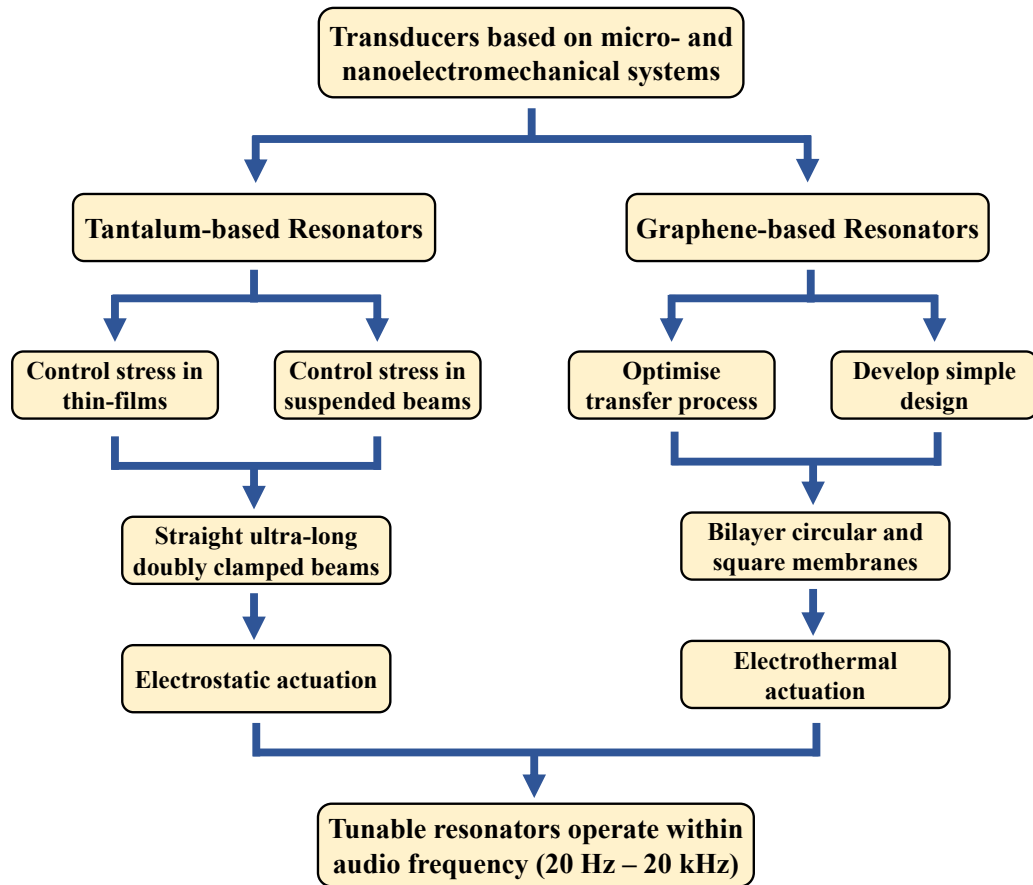


Figure 1.3: Main objectives of the thesis showing the development stages of audio resonators based on tantalum metal and graphene membranes.

In the last part of this thesis, the mechanical and dynamic behaviour (resonant frequency, amplitude of vibration, tunability and tuning sensitivity) of graphene-based resonators under electrothermal actuation will be investigated comprehensively. The practical exploitation of graphene's unique properties and the possibility to transfer large and high-quality membranes will be a major contribution of this project. The ability to make large aspect ratio devices of graphene can be considered as an advanced step towards the development of highly sensitive and tunable graphene resonators for reliable acoustic transducers.

1.4 Thesis organisation

The thesis is divided into seven chapters as follows: **Chapter 1** introduces MEMS and NEMS fields and gives an overview of the motivation of this project with a focus on acoustic transducers and their potential applications. **Chapter 2** provides analytical models based on proposed designs of doubly clamped beams and membranes structures. Also, an overview of electrostatic and electrothermal actuation mechanisms will be given. **Chapter 3** is dedicated to the fabrication and characterisation of suspended structures of tantalum microbeams. The focus of this chapter will be on evaluating the effects of residual stress and etching release processes on the final structure of fabricated resonators. **Chapter 4** is devoted to fabricating and characterising an array of ultra-long beams of tantalum. The use of electrostatic actuation to drive the resonators into resonance and tune their resonant frequencies will be presented. **Chapter 5** describes briefly the importance of graphene and current fabrication methods used to transfer graphene membranes from growth substrate to other substrates. The limitations of the transfer approaches as well as characterising the transferred membranes will be discussed. **Chapter 6** is dedicated to the design, fabrication and characterisation of ultra-large graphene-based resonators. Electrothermal transduction will be presented as an actuation approach to investigate the dynamic behaviour of the devices. **Chapter 7** concludes the main achievements of this research work with recommendations and suggestions for future work.

Chapter 2

Literature Review, Design and Actuation of Resonators

2.1 Introduction

This chapter is dedicated to covering the design and analytical models used to predict the performance of tantalum- and graphene-based resonators. First, an overview of current trends in acoustic transducers, hearing aids and microphones, will be presented. Two different models based on clamped-clamped beams of tantalum and circular and square thin-films of graphene will be introduced. The dynamic vibration behaviour of the proposed models will be predicted using different geometrical characteristics and material properties. Moreover, an overview of electrostatic and electrothermal actuation mechanisms will be provided in this chapter.

2.2 Acoustic transducers: literature review

Mechanical or acoustic transducers have been in commercial use for decades. Today, modern acoustic technology expands to cover a wide range of industrial sectors. The hearing aids market, which

is expected to exceed more than \$9 billion by 2023 [26], is one of the largest consumers of acoustic transducers. The microphones sector whose current global market reaches \$1 billion [27] is also expanding to include a diversity of devices such as mobile phones, video cameras, computers, wearables, hearing aids and a range of medical devices. In the following subsections, a literature review on the development of artificial cochlear models and MEMS-based microphones is presented.

2.2.1 MEMS for hearing assistive systems

Hearing loss is the most widespread sensory impairment in humans, and one of the most common global disease burden in the world [28]. The World Health Organization (WHO) estimates that approximately 5 % of the world's population suffers from hearing loss [29]. There are already more than 360 million people (328 million adults and 32 million children) having disabling hearing loss. This number is expected to increase to more than 1 billion, especially among young adults and teenagers, because of the excessive and improper use of audio devices. Conventional hearing aids could help in restoring mild-to-moderate hearing loss. Patients who suffer from deafness or severe-to-profound hearing loss cannot benefit from standard hearing aid devices. Instead, an artificial system composed of electronic elements called cochlear implants (CIs) [30], shown in [Figure 2.1](#), can be used to provide sound sensations by replacing the main functions of the impaired inner ear.

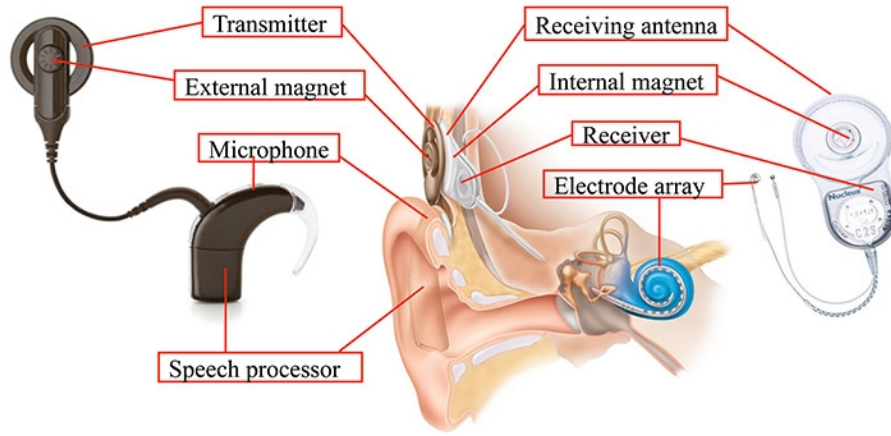


Figure 2.1: Schematic illustration of cochlear implants showing the internal and external components. Image taken from [31].

In fact, the key biological structure that is responsible for the transduction of vibrational signals into neurological signals and determine the performance of hearing is a spiral-shaped organ in the inner ear called the cochlea. The two main functions of the cochlea are frequency selectivity and acoustic-to-electric signal conversion. The wide range of time-domain frequencies of acoustic signals from the outside surroundings will be decomposed into patterns of frequencies components by a flexible membrane called the basilar membrane (BM). The acoustic-to-electric signal conversion feature of the cochlea is achieved by $\sim 30,000$ hair cells that transmit mechanical vibrations into neural impulses. Therefore, the cochlea can be considered as a real-time mechanical frequency analyser due to its striking capability of splitting more than 3500 channels of frequency components from the incoming acoustic signals [32–34].

In order to provide suitable solutions for hearing loss impairments, it is important to understand and possibly reproduce the physiological characteristics of the cochlea. Biomechatronic devices such as artificial cochlear implants have been developed to reproduce the hearing functions of the damaged cochlea.

As fabrication technologies advance more, MEMS-based physical cochlear models have been introduced [16].

MEMS-based models of the cochlea have the advantages of achieving enhanced features such as life-sized dimensions, low power consumption and biocompatibility. Different types of structures, designs and materials are involved in the construction of physical models of the cochlea. Most models that exist rely on structural elements such as beam arrays, plates and membranes. In particular, extensive efforts have been made for the development of artificial basilar membranes (ABMs) that can reproduce the frequency selectivity and acoustic-to-electric signal conversion features of the cochlea. A schematic diagram comparing the characteristics between a biological system and an artificial cochlea is illustrated in Figure 2.2.

The frequency selective feature of the cochlea can be reproduced by utilising structural components with dimensions that vary in length [17–19], width [20, 21] and thickness [22]. The reason behind varying the structural parameters is that the basilar membrane varies in its width, thickness and stiffness; hence the hair cells can detect high frequencies near the base of the cochlea and low frequencies near the apex part [32]. The structural elements used for the realisation of artificial basilar membranes can be constructed in the form of beams array or membranes. To achieve the acoustic-to-electric signal conversion feature of the cochlea, structural elements made from piezoelectric [21], piezoresistive [35], and optical [36] materials have been employed.

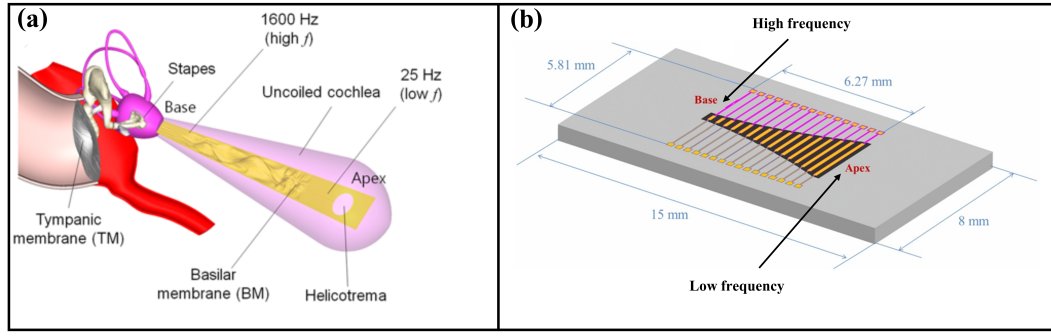


Figure 2.2: Schematic illustration of frequency selectivity of the cochlea to different regions of the uncoiled (a) and artificial (b) basilar membrane. Images taken from [17, 37].

2.2.2 MEMS microphones for audio applications

A microphone is an electromechanical transducer that converts acoustical signals into electrical signals. The operating frequency of microphones is within the audible range (20 Hz – 20 kHz). The advancement in semiconductor technologies has led to MEMS-based microphones [23–25]. A MEMS-based microphone consists of a vibrating diaphragm suspended over a fixed backplate with an air gap of a few microns between the two plates, as shown in Figure 2.3. When the acoustic waves pass through the perforated backplate and strike the flexible diaphragm, the suspended diaphragm will vibrate because of the change in air pressure. Due to the deformation of the diaphragm, the capacitance between the diaphragm and the backplate will change, and thus an electrical voltage signal will be produced and amplified.

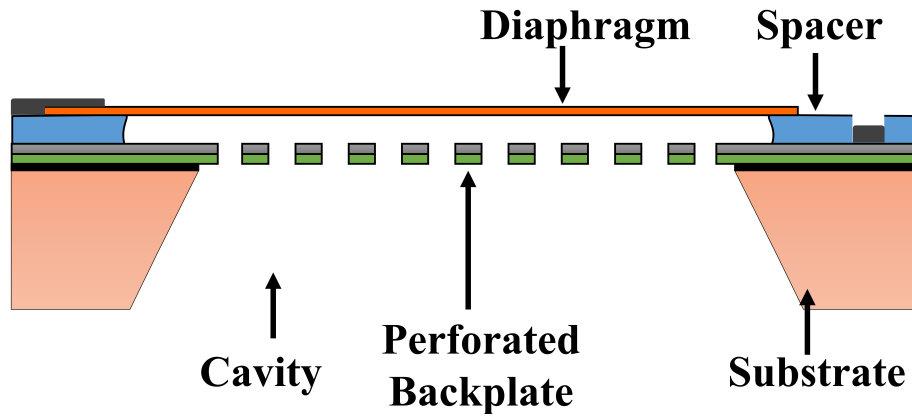


Figure 2.3: Cross section of a MEMS microphone showing the vibrating diaphragm and backplate.

The size, design and materials of microphones can be adjusted, depending on the desired device function and the application of focus. Although MEMS microphones use different transduction methods [25, 38–41], capacitance-based microphones, however, are the most popular microphones due to their desirable characteristics such as high sensitivity, low noise level and proper frequency response [25]. For the resonators reported here, the proper frequency response should include, for example, resonant frequencies within the audio range, high amplitude of vibration and high quality (Q) factors that meet the operational requirements of audio transducers. From a materials point of view, the existing microphones are made mainly from silicon [42] or polysilicon [24].

The growing use of MEMS microphones, compared to the conventional electret condenser microphones, is attributed to their enhanced performance, small form factor, low power consumption, excellent frequency response, good sensitivity, high signal to noise ratio (SNR) and high level of integration with other electronics components. These excellent characteristics have paved the way for MEMS microphones to substitute effectively the traditional electret condenser microphones. Today, MEMS microphones are

used extensively in mobile phones, cars, video cameras, computers, wearables, hearing aids, digital assistants and medical devices.

2.3 Mechanical resonator

Mechanical resonator is one of the most important MEMS/NEMS devices and can be considered as a main building block for many types of small sensors and actuators. Simply, a resonator is a physical component that oscillates at its resonant frequency and different harmonics with different amplitudes of vibration. As the mechanical elements of the system vibrate, the vibration will take a particular pattern. The patterns represent the shape of the resonant mode. The resonant frequency is a fundamental characteristic that can be used to define the sensitivity and precision of vibrational systems. For example, a mechanical resonator can be used as a sensor in such a manner that a shift in the resonant frequency is observed as a response to a measurand such as pressure, acceleration and temperature. In general, the resonant frequency of a resonator depends strongly on a set of parameters, most important of which are the resonator geometry, mechanical properties, especially mass and stiffness of resonator materials, and damping effects [3, 4]. In order to describe the dynamics of the mechanical resonators proposed in this project, discrete (lumped) and continuous models will be presented briefly.

2.3.1 Discrete model

A discrete model can be used to model the periodic motion of a mechanical resonator by considering the resonator as an idealised system, in which the mechanical properties of the resonator are intensified at discrete points (uncoupled). In this case, the discrete model is capable of predicting accurately the system performance characteristics such as modal frequencies and mechanical displacements of a finite number of the system discrete

points. In fact, a resonator structure can be treated as a simple harmonic oscillator. In this case, a mechanical mass–spring–damper system is used to describe the mass and stiffening of the resonator. Therefore, the vibration of the resonator could be modelled accurately via single-degree-of-freedom (SDOF) theory [43].

Figure 2.4 shows a schematic illustration of a typical mass-spring-damper model of a SDOF oscillator system. When an excitation force of $F(t)$ is applied to a mass-spring-damper system, the system will respond as a shift in the displacement. In general, the equation of motion for such a system is given in the time domain as follows:

$$M_{eff} \frac{\partial^2 x}{\partial t^2} + C_{eff} \frac{\partial x}{\partial t} + K_{eff} x(t) = F(t) \quad (2.1)$$

where M_{eff} is the effective mass of the system, C_{eff} is the effective total losses in the system (damping coefficient), K_{eff} is the effective stiffness (spring constant), and $x(t)$ is the displacement response of the oscillator.

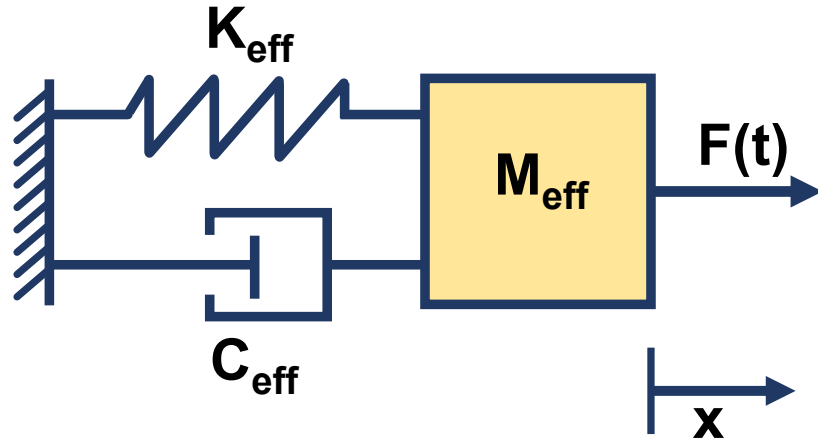


Figure 2.4: Schematic diagram of mass-spring-damper model of a SDOF resonator system.

When no external force is applied to the system (i.e. $F(t) = 0$), the undamped natural frequency (ω_0) for an ideal undamped system (i.e. $C_{eff} = 0$) is given as follows [44]:

$$\omega_0 = \sqrt{\frac{K_{eff}}{M_{eff}}} \quad (2.2)$$

In addition to the resonant frequency attribute, the quality factor

(Q) is another essential characteristic that determines the intrinsic energy dissipation in the resonator system. In general, the quality factor can be expressed respectively in terms of energy dissipation and damping ratio (ζ) as follows [11]:

$$Q = 2\pi \frac{\text{average energy stored}}{\text{energy lost per cycle}} \quad (2.3)$$

$$Q = \frac{1}{2\zeta} = \frac{\sqrt{KM}}{C} \quad (2.4)$$

For an ideal damped system, the damped natural frequency (ω_d) is defined as follows [43]:

$$\omega_d = \omega_0 \sqrt{1 - \zeta^2} \quad (2.5)$$

The undamped natural frequency is usually greater than the damped counterpart. However, when the damping ratio is small (i.e. Q is large), the damped and undamped natural frequencies are nearly equivalent (i.e. $\omega_d \approx \omega_0 = \sqrt{K/M}$). There is a case when the applied actuation force is periodic in such a way that it has an amplitude of F_0 and frequency of ω . Therefore, the governing equation of motion and resonant frequency (ω_{res}) corresponding to the peak of resonance that results in a maximum displacement can be written respectively as follow:

$$M_{eff} \frac{\partial^2 x}{\partial t^2} + C_{eff} \frac{\partial x}{\partial t} + K_{eff} x(t) = F_0 \sin \omega t \quad (2.6)$$

$$\omega_{res} = \omega_0 \sqrt{1 - 2\zeta^2} \quad (2.7)$$

Figure 2.5 shows an analytical comparison between the damped

natural frequency ω_d (Equation (2.5)) and the resonant frequency ω_{res} (Equation (2.7)) with respect to the damping ratio. It can be seen that as the damping ratio increases, the frequency decreases. Also, with the use of the same damping ratio, the damped natural frequency seems to increase (upward shift) compared to the resonant frequency, as shown in the inst in Figure 2.5.

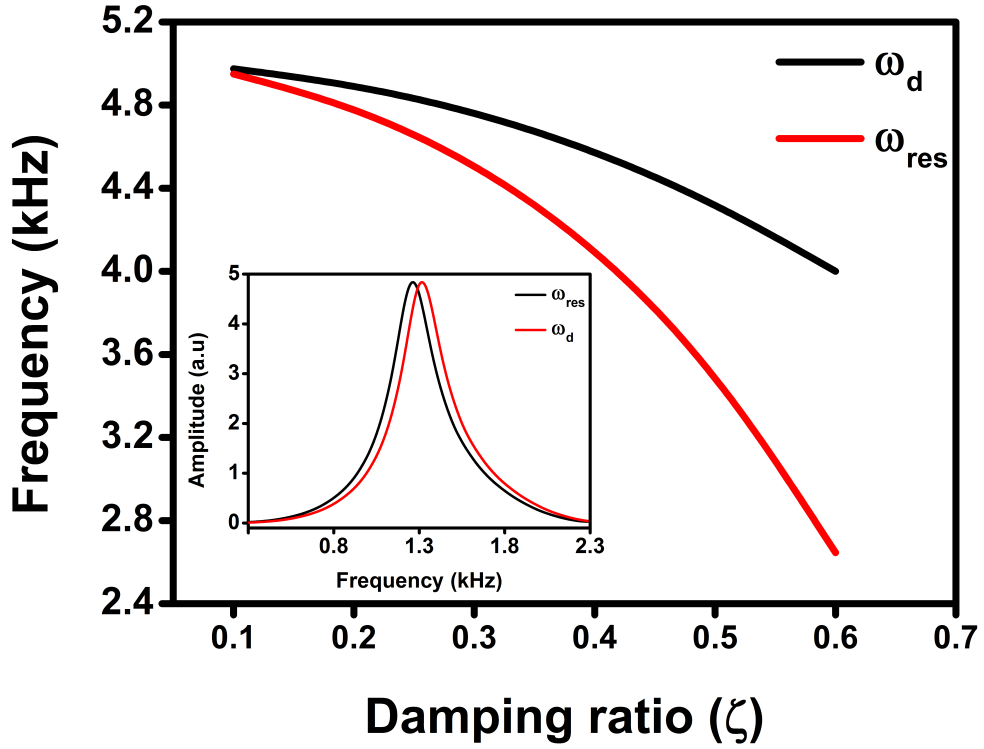


Figure 2.5: Calculated damped natural frequency and resonant frequency of a system as a function of the damping ratio. Inset shows the frequency response curves of damped natural and resonant frequencies. The value of ω_0 used in the calculations is 5 kHz.

2.3.2 Continuous model: Euler-Bernoulli beam

A mechanical resonator structure can be treated as a continuous system by assuming that the mechanical properties, i.e. mass and stiffness, of the structure are distributed rather than discrete. In other words, the system is considered to have multi degree-of-freedom (MDOF) for motion and its properties are independent of time and frequency [45]. In this case, the vibrational

motion of the system can be interpreted as modal vibrations and mechanical displacements from continuous variables point of view. For example, the mechanical deflection of a mechanical resonator that has a length varying from 0 to l can be captured as a function of the continuous variable length.

When the resonator's longitudinal geometrical dimensions (i.e. length) are much larger than the transverse counterparts (i.e. thickness and width), the vibrational response of the resonator is governed by flexural motion. In general, the structure will experience an elastic deformation in the form of bending along its length. Therefore, Bernoulli–Euler beam theory can be used to describe the governing equation of the flexural modes of vibration as follows [46]:

$$EI \frac{\partial^4 w(x, t)}{\partial x^4} - N \frac{\partial^2 w(x, t)}{\partial x^2} + \rho A \frac{\partial^2 w(x, t)}{\partial t^2} = f(x, t) \quad (2.8)$$

where $w(x, t)$ is the time dependent transverse deflection, $f(x, t)$ is the externally applied force, E is the elastic modulus, I is the cross-sectional moment of inertia, ρ is the mass density, A is the cross-sectional area, N is the tension, and (x, t) are the spatial (x) and time (t) coordinates.

Now, consider the free vibrations of an elastic beam, the external excitation force is assumed to be zero (i.e. $f(x, t) = 0$), and hence the dimensionless equation of motion (Equation (2.8)) of stress-free system is given by:

$$EI \frac{\partial^4 w(x, t)}{\partial x^4} + \rho A \frac{\partial^2 w(x, t)}{\partial t^2} = 0 \quad (2.9)$$

The above equation (Equation (2.9)) can be rewritten for a

uniform beam as follows [47]:

$$c^2 \frac{\partial^4 w(x, t)}{\partial x^4} + \frac{\partial^2 w(x, t)}{\partial t^2} = 0 \quad (2.10)$$

where $c = \sqrt{EI/\rho A}$.

It is worth pointing out that the analytical calculations and numerical simulations provided in this chapter and the rest of the thesis are based on discrete models. In the next sections of this chapter, a discrete-based models will be used to predict the resonant frequencies of tantalum and graphene resonators. The calculations will provide a platform to choose a design that satisfies the operational requirements of audio frequency resonators.

2.4 Tantalum-based resonators

The properties of materials involved in fabricating vibrational-based structures are also important. In order to achieve a specified operating frequency range, it is necessary to use a material with proper mechanical properties. Tantalum microbeams have been chosen to create mechanical resonators with an aim to contribute to the development of biomechatronic devices such as hearing aids and artificial cochlear systems. The physical properties of tantalum and more details about the resonators' design will be given in the following subsections.

2.4.1 Design of tantalum beams

The design of tantalum-based resonators has been proposed in the form of an array of clamped-clamped beams. A doubly clamped beam structure with length of l , width of w and thickness of t is shown in [Figure 2.6](#).

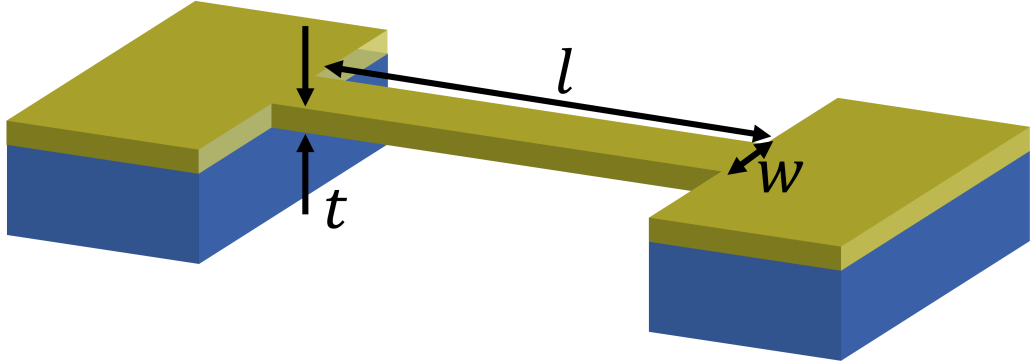


Figure 2.6: Schematic diagram of a clamped-clamped beam resonator.

When an array of clamped-clamped beams of tantalum with different lengths are actuated, the vibration of the beams will be seen as a band of different resonant frequencies. Motivated

by the mechanism of the basilar membrane, it is possible, for example, to mimic the frequency separation function of the basilar membrane by controlling the geometrical parameters: length, width and thickness. Since the narrow part of the basilar membrane detects high frequencies while the wide part detects low frequencies, see [Figure 2.7](#), which suggests that changing the beams length could be an effective way to achieve the frequency-selective characteristic.

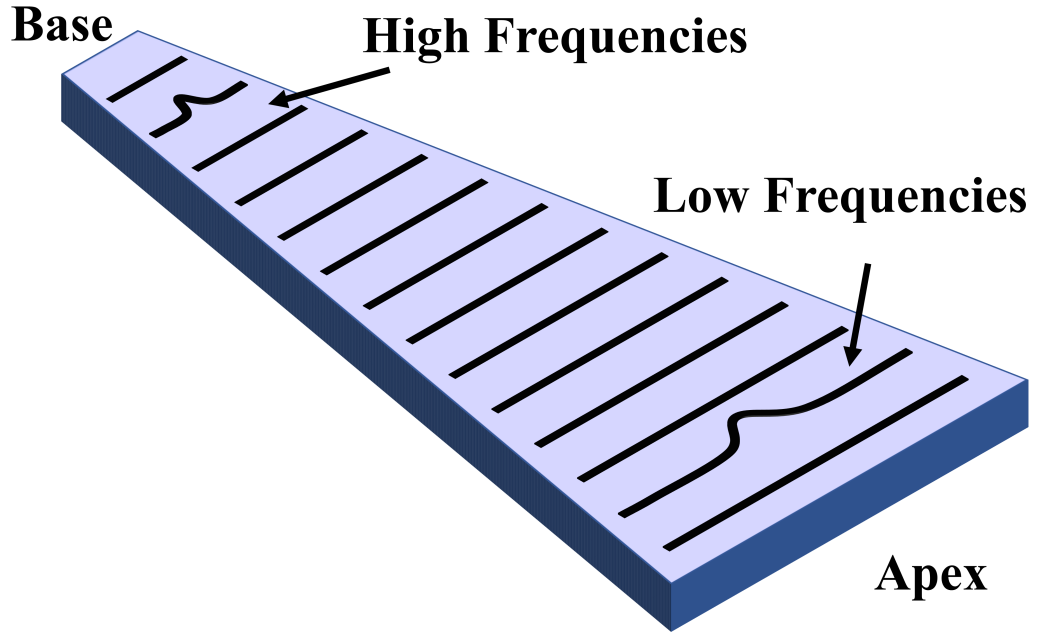


Figure 2.7: The schematic diagram of a basilar membrane showing the frequency response along the membrane length.

In general, the resonant frequency (f_n) of a clamped-clamped beam can be expressed as follows [47]:

$$f_n = \frac{\omega_n}{2\pi} = \frac{\lambda_n^2}{2\pi l^2} \sqrt{\frac{EI}{\rho A}} \quad (2.11)$$

where $\lambda_n \cong (2n + 1)\pi/2$ is the dimensionless coefficient of the resonant mode (n). For the first four resonant modes, $\lambda_1 = 4.73$, $\lambda_2 = 7.85$, $\lambda_3 = 10.99$ and $\lambda_4 = 14.13$.

In the case of the beam's width being relatively larger than the thickness (i.e. $w > 5t$), Young's modulus (E) is replaced with an effective Young's modulus (\hat{E}) by including the Poisson's ratio of the beam material (ν) as follows [43]:

$$\hat{E} = \frac{E}{1 - \nu^2} \quad (2.12)$$

Equation (2.11) can be further reduced by using the cross-sectional area of the beam as $A = wt$ and the moment of inertia as $I = wt^3/12$, where w is the beam width and t is the beam thickness. Therefore, the resonant frequency of a doubly clamped beam is given the final form by:

$$f_n = \frac{\lambda_n^2 t}{4\pi l^2} \sqrt{\frac{E}{3\rho}} \quad (2.13)$$

The above Equation (2.13) indicates that the resonant frequency of the beam can be tuned (shifted upwards or downwards) by adjusting t , l and E/ρ parameters. The analytical calculations of the resonant frequency of doubly clamped beams of tantalum in the following subsections are based on the geometrical dimensions and mechanical properties provided in Table 2.1.

Table 2.1: Parameters of geometrical dimension and mechanical properties [48, 49] for the resonant frequency calculations of tantalum clamped-clamped beams.

Parameter	Value	Unit
Length	100 – 3400	μm
Thickness	0.5, 1.0	μm
Width	20	μm
Young's modulus	186	GPa
Density	16.65	g/cm^3
Poisson's ratio	0.34	–

2.4.2 Why tantalum?

Tantalum (Ta) is a versatile refractory metal with atomic number 73. The physical and chemical properties of tantalum are undoubtedly attractive. One of the main exceptional characteristics of tantalum is its resistance to corrosion [50]. This feature has enabled the use of tantalum for corrosion-resistant applications such as chemical-processing equipment and tools for anti-corrosion buildings and constructions [51]. Along with its corrosion-resistance attribute, tantalum has other excellent physical properties such as high thermal and electrical conductivities. The outstanding properties of tantalum have been employed practically in electronic devices such as tantalum-based electronic capacitors. Tantalum capacitors have played a significant role in shrinking the size of telecommunications and personal ubiquitous electronic equipment such as mobile phones, hard drives, hearing aids, DVD players and laptops. Other unique properties of tantalum include high melting point (3290 K), high density, high ductility and high fracture toughness [52].

With all these unique properties, tantalum can be considered as a promising material in bio-medical, MEMS devices and high-temperature applications. Most of the applications rely on tantalum in the thin-film form. For example, tantalum thin-films have been playing an important role in electronic devices acting as a diffusion barrier between deposited metals and silicon substrate [53–55], as an alternative of hazardous electrodeposited chromium coatings [56], and an excellent x-ray mask absorber [57]. The use of tantalum has also been extended to cover the health-related field thanks to its mechanical strength and high biocompatibility features. For instance, tantalum can be utilised as a hardener coater on titanium surfaces for orthopaedic and other implants applications

[58].

Mechanically, tantalum has an elastic modulus (E) of 186 GPa and density (ρ) of 16.65 g/cm³. Compared to other metals, tantalum owns a smaller E/ρ , which can be considered a crucial characteristic for achieving low frequency response. To examine the effect of mechanical properties of a material on the frequency response, the fundamental resonant frequency for a set of metals with different values of E/ρ has been estimated from Equation (2.13) and plotted in Figure 2.8.

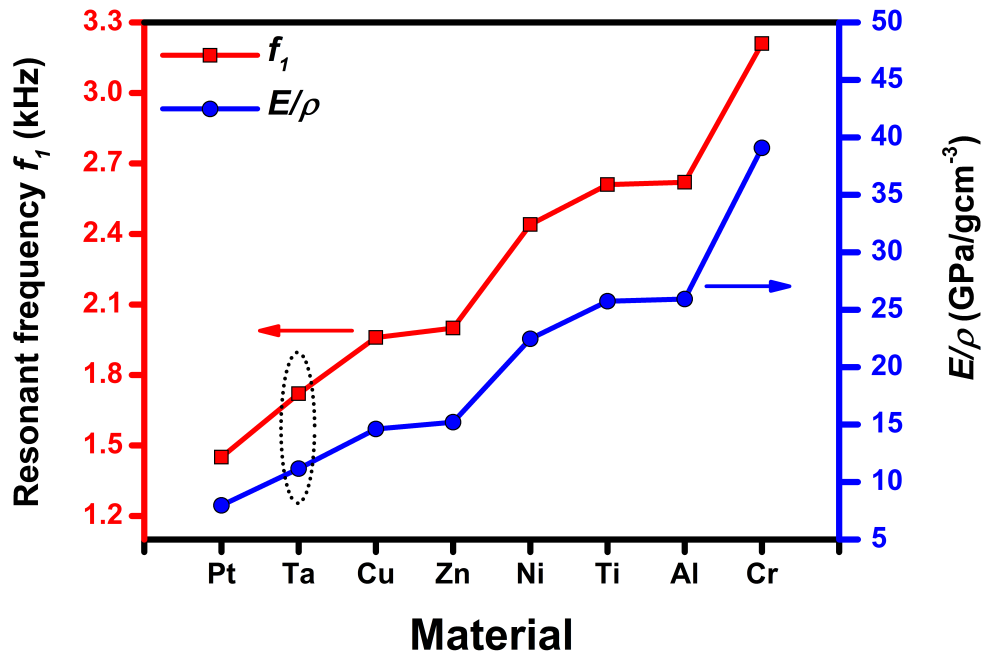


Figure 2.8: The effect of E/ρ on the first resonant frequency for different metals beams with a length of 1000 μm and thickness of 0.5 μm . The metals are: platinum (Pt), tantalum (Ta), copper (Cu), zinc (Zn), nickel (Ni), titanium (Ti), aluminium (Al), and chromium (Cr).

It can be seen that as the ratio of E/ρ decreases, the resonant frequency decreases. Out of the shown metals, tantalum possesses a small ratio of E/ρ , which in turn would make a tantalum-based resonator vibrate at low frequency. From a fabrication point of view, tantalum is easy to fabricate. Comparatively, metals such as platinum face a number of challenges and difficulties that are mostly

associated with the cost of the manufacturing process. In addition, some of the metals are either incompatible with other electronics circuits or they vibrate at high frequency.

Despite all the important applications mentioned, the mechanical properties of tantalum have not yet been exploited fully in resonance-based MEMS and NEMS devices. For example, two studies have been reported using tantalum metal to create bridge-like beams that can act as a suspended gate for resonant gate transistors (RGTs) [59] or it can be simply employed to study the buckling deformation in the fabricated beams [60].

2.4.3 Influence of beam geometry on resonant frequency

The geometrical dimensions of vibrating structures play a key role in determining the resonant frequency of a resonator device. Length and thickness are the most influential parameters of doubly clamped beam resonators. [Figure 2.9](#) shows the fundamental resonant frequency of doubly clamped beams of tantalum calculated with respect to different values of length (100 μm to 3.4 mm) and thickness (100 nm – 1.5 μm). Note that the provided calculations are based on stress-free structures. It can be seen that the resonant frequency decreases with the increase of the beam length. The relatively short beams (i.e. 100, 200 and 300 μm) have covered frequencies outside the audio range. On the other hands, the long beams (400 – 3400 μm) cover low frequencies within the audio range. If we assume that the stress in the beam is controlled, it can be concluded that the design of clamped-clamped beams with length of 500 μm or longer is appropriate for acoustic-based resonators.

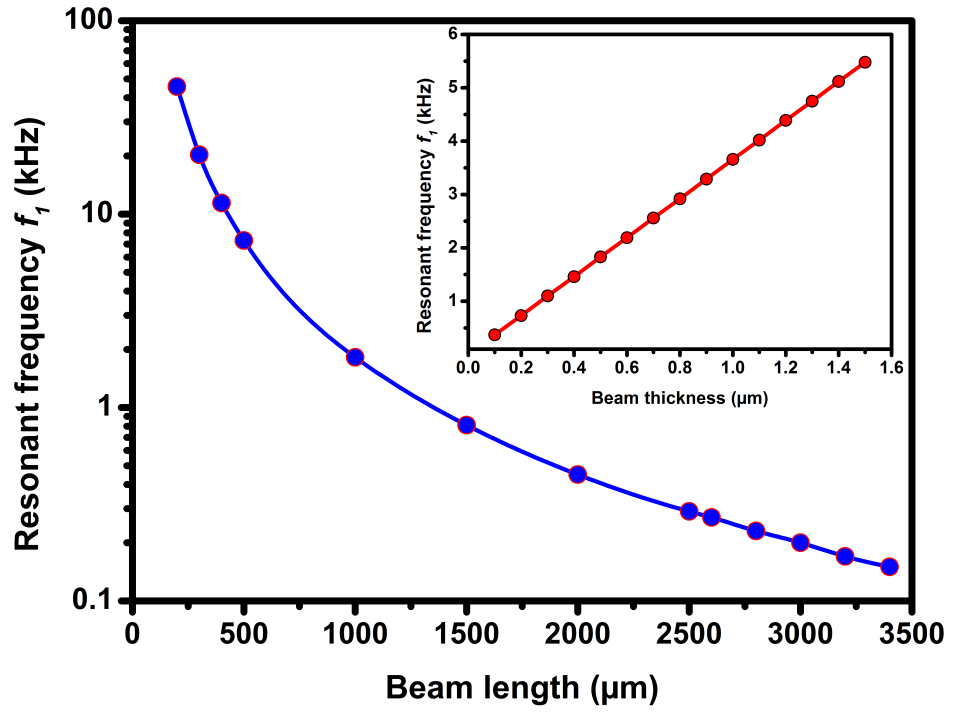


Figure 2.9: Calculated fundamental resonant frequency as a function of the beam length. Note that the thickness of the beams has been held at a constant value of 0.5 μm for frequency-length calculations. Inset shows the calculated fundamental resonant frequency as a function of the beam thickness while fixing the beam's length at 1000 μm .

The analytical calculations plotted in the inset in Figure 2.9 show that as the beam thickness increases, the resonant frequency increases accordingly. It can be also noted that the estimated resonant frequencies, especially the first and second modals, cover the first quarter of the audio range (i.e. up to ~ 5 kHz). For example, the fundamental resonant frequency has been estimated to be 370 Hz for the thinnest beam (100 nm) compared to ~ 5 kHz for the thickest beam (1.5 μm). Although the estimated frequencies are within the audio range, the influence of the beam thickness on the resonant frequency is less than that of the beam length.

2.5 Graphene-based resonators

Modern acoustic transducers such as microphones, eardrums and loudspeakers rely on free-standing thin-film structures to produce vibration. For audio applications, thin films-based vibrational devices are required to be designed in such a way that resonant frequencies within the audible range are achievable. However, the dynamic behaviour of a thin-film structure may vary, depending on whether the structure behaves as a membrane or as a plate. In general, the resonant frequency of a thin-film depends on several parameters, most important of which are: geometrical dimensions, boundary conditions and material properties. In a similar way to the previously discussed analytical models of beam-based structures, the effect of geometrical design and material properties of graphene thin-films on the resonant frequency will be investigated.

2.5.1 Why graphene?

A major motivation for developing graphene-based resonators is that graphene is one of the thinnest, lightest and strongest materials to ever exist. The exceptional mechanical properties of graphene such as high strength of ~ 130 GPa [61], high Young's modulus of ~ 1 TPa, and ultra-low mass density of 2200 kg/m^3 [62] would make a graphene film an ideal candidate for highly sensitive resonators. More details about graphene properties are presented in [Chapter 5](#).

2.5.2 Resonant frequency of membranes and plates

When the thickness of a film is extremely small, the film behaves as a membrane. For a membrane-like system, the in-plane initial pre-tension (N) is dominant while the out-of-plane bending rigidity (D) can be negligible. The resonant frequencies (f_{mn}) of ideal

clamped circular and square membranes under initial pre-tension are given as follows [63]:

$$f_{mn}(\text{circular membrane}) = \frac{\alpha_{mn}}{2\pi R} \sqrt{\frac{N}{\rho t}} \quad (2.14)$$

$$f_{mn}(\text{square membrane}) = \frac{\alpha_{mn}}{2\pi a} \sqrt{\frac{N}{\rho t}} \quad (2.15)$$

where R is the radius of the circular membrane, a is the side length of the square membrane, t is the thickness of the membrane, ρ is the density of the material, and α_{mn} is a dimensionless coefficient of the resonant mode (m, n are the number of nodal lines). For the first three modal frequencies, the values of α_{mn} are respectively 2.405, 3.832 and 5.135 for circular membranes and 4.443, 7.025 and 8.886 for square membranes [43].

For some vibrational devices, it is necessary for the thickness of the structural material to be relatively thick. As the thickness of a film structures increases, the dynamic behaviour changes accordingly. When the structural material of a film is relatively thick, the in-plane tensions can be neglected, as the bending rigidity (D) becomes the more dominant restoring force. In this case, the resonant frequencies of clamped and stress-free circular and square plate can be written as [64]

$$f_{mn}(\text{circular plate}) = \frac{\beta_{mn}^2}{2\pi R^2} \sqrt{\frac{D}{\rho t}} \quad (2.16)$$

$$f_{mn}(\text{square plate}) = \frac{\beta_{mn}^2}{2\pi a^2} \sqrt{\frac{D}{\rho t}} \quad (2.17)$$

where β_{mn}^2 is a dimensionless coefficient of the resonant mode. The values of β_{mn}^2 for the first three modes are respectively 10.22, 21.26 and 34.88 for circular plates and 35.99, 73.41 and 108.3 for square

plates. For plate with Young's modulus of E and Poisson's ratio of ν , the bending rigidity takes the following form [43]:

$$D = \frac{Et^3}{12(1 - \nu^2)} \quad (2.18)$$

The major difference between the resonant frequencies of the membrane and plate models is related to their different dependence on parameters of diameter, thickness and tension. For example, the resonant frequency of a circular membrane is inversely proportional to the membrane radius and thickness (i.e. $f \propto (1/Rt^{1/2})$). For the plate model, on the other hand, $f \propto t/R^2$.

2.5.3 Influence of film geometry on resonant frequency

To provide a proper design that could make graphene-based resonators tunable to the audio frequencies, it is necessary to determine how geometrical parameters such as diameter, thickness and tension influence the dynamic response of the resonator. From equations (2.14 – 2.17), it can be perceived that the resonant frequency of circular or square thin films depends on dimensions (e.g. thickness and diameter/side length) and mechanical parameters (e.g. tension and elastic modulus) of the resonator. Therefore, analytical calculations have been performed to estimate the resonant frequency of graphene films with respect to the film diameter and tension, see [Figure 2.10](#). The calculations are based on graphene's mechanical properties of Young's modulus of 1 TPa [61], mass density of 2.2 g/cm³ [62] and Poisson's ratio of 0.16 [61].

It can be seen clearly that the resonant frequency decreases with the increase of the diameter. Although both membrane and plate models have shown frequencies outside the audio range, the resonant

frequencies in the plate case have been found to be extremely small. The reason behind this is that the plate model is only valid for relatively thick materials; thus, the ultra-small thickness of monolayer graphene would make graphene act as a membrane rather than a plate.

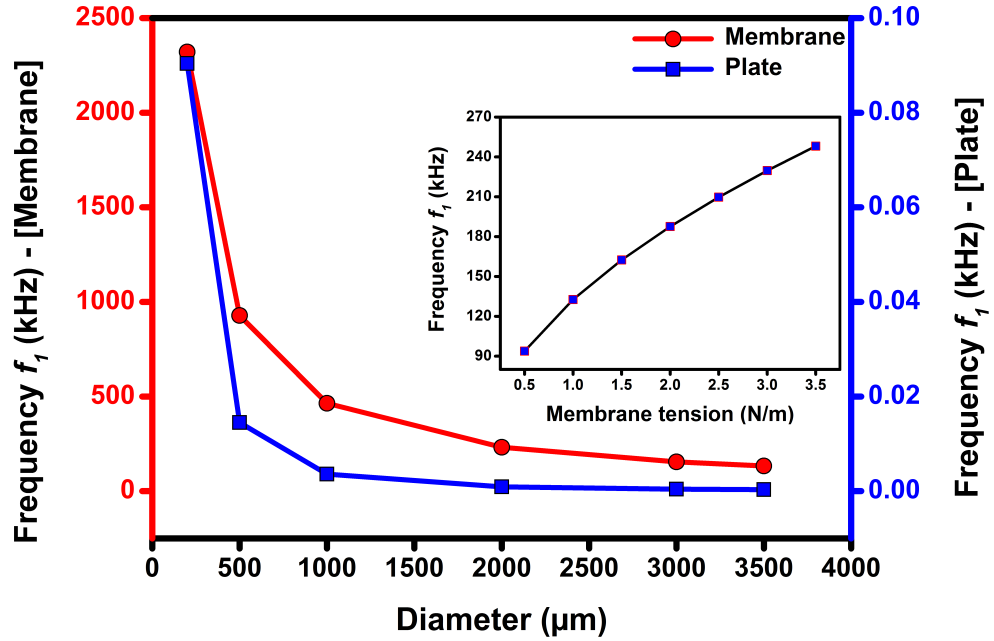


Figure 2.10: Calculated fundamental resonant frequency of circular graphene films as a function of the film diameter using membrane and plate models. Note that monolayer graphene films have been used in the calculations. For the membrane model, the tension has been fixed at 1 N/m. Inset shows the calculated fundamental resonant frequency as a function of the membrane tension.

With regards to the effect of thickness of graphene film, it can be deduced that increasing the number of graphene layers leads to a decrease of resonant frequency for the membrane model (Equation (2.14)). In the case of the plate model (Equation (2.16)), on the other hand, the calculation indicates an increase of the resonant frequency with an increase of the number of graphene layers. From a practical point of view, it seems that it is more viable for audio sensing applications-to design graphene-based resonators from a membrane structure rather than a plate one. For membrane-like vibrating structures, the impact of membrane

tension should be taken into consideration ([Equation \(2.14\)](#)). The inset in [Figure 2.10](#) shows the fundamental resonant frequency of a monolayer graphene membrane calculated as a function of the membrane tension. It has been found that increasing the membrane tension leads to an upward shift of the resonant frequency. It can be concluded that graphene-based resonators can be made tunable by modifying their induced tension. The dynamic behaviour of graphene-based resonators will be discussed in more detail in [Chapter 6](#).

2.6 Electrostatic actuation of tantalum beams

In MEMS transducers, one form of an input energy is converted into another form of output energy. Free-standing MEMS structures can be set into motion by applying an excitation force. The driving mechanism plays a significant role in exciting vibrating structures into resonance and detecting their motion. In transduction systems, several transduction mechanisms such as electrostatic, electromagnetic, optical, piezoelectric, piezoresistive and electrothermal are used for actuation and /or sensing. In general, appropriate transduction technique is employed when particular physical or chemical quantities need to be sensed or controlled. Electrostatic is the most commonly used actuation and sensing approach in MEMS because of its inherent advantages, including fast actuation rates, large travel distances, low power consumption and compatibility with micro-fabrication processes [65].

In general, a MEMS-based resonator can be actuated electrostatically by using a capacitor structure of movable and stationary parallel electrodes. One of the electrodes is stationary while the other one is movable. Figure 2.11 shows a schematic diagram of an electrostatic resonator consisting of a suspended moveable plate separated from a fixed bottom electrode by a dielectric spacer. The moveable plate is a clamped-clamped beam structure with a length of l , width of w and thickness of t . The initial air gap between the two plates is d_0 .

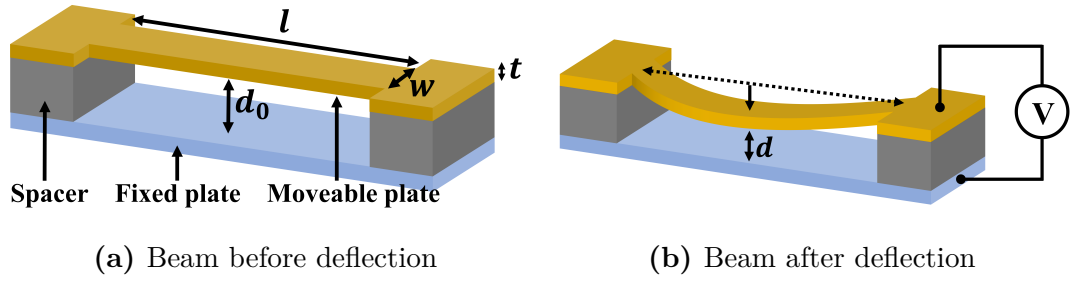


Figure 2.11: Conceptual diagram of capacitively-transduced resonator of a clamped-clamped beam. (a) Before deflection. (b) Beam deflected due to applied voltage across the fixed electrode and movable top plate.

When no voltage is applied across the plates, the suspended beam will be in its static position, see [Figure 2.11a](#). When a constant actuation voltage, V , is applied across the beam and actuation electrode, a potential difference will be created, and thus an electrostatic force (F_{ele}) will be induced. The induced electrostatic force will pull the suspended beam down towards the actuation electrode underneath, see [Figure 2.11b](#).

Since the suspended beam behaves like a spring with stiffness of K , the developed electrostatic attractive force will stretch the spring and result in a decrease of the air gap spacing between the two conductors. When actuated, the initial gap spacing decreases from d_0 to d . Accordingly, the electrostatic force between the beam resonator and actuation electrode is given by [\[43\]](#)

$$F_{ele} = \varepsilon \frac{AV^2}{2d^2} \quad (2.19)$$

where A is the overlapping surface area between the plates and ε is the permittivity of free space.

It can be seen from [Equation \(2.19\)](#) that the electrostatic force is proportional to the resonator area, and to the square of the actuation voltage. The resonator can be driven into resonance by applying an actuation voltage of a combination of an

alternating current (AC) and a direct current (DC). Accordingly, the corresponding V^2 is given by

$$V^2 = 2V_{ac}V_{dc}\sin\omega_{ac}t + 0.5V_{ac}^2(1 - \cos 2\omega_{ac}t) + V_{dc}^2 \quad (2.20)$$

where ω_{ac} is the angular frequency of the input voltage V_{ac} . Therefore, the resonator will be driven into resonance when the driving frequency (f_{ac}) of the input voltage matches the mechanical frequency of the beam resonator (f_0), so that $f_{ac} = f_0$. The matching occurs when both V_{ac} and V_{dc} are applied, so that $f_0 = \omega_{ac}/2\pi$. When the applied voltage is only V_{ac} , the resonance will take place at $f_{ac} = 1/2f_0$.

2.7 Actuation of graphene-based resonators

One of the outstanding challenges in graphene-based vibrational devices is driving them into resonance and tuning their resonant frequencies over a desired range. In general, the function of transduction systems is to convert electrical signals into mechanical displacements of a vibrating structure and vice versa. In addition to the actuation mechanism, different readout methods (optical, electrical and scanning probe microscopy) are used to detect the dynamic response (resonant frequency and oscillation amplitude) of vibrating structures [62].

Electrical driving is the most effective mechanism for 2D materials-based devices [62]. So far, graphene-based vibrational devices can be driven/actuated mainly either electrostatically [66, 67] or acoustically [68]. Electrostatic actuation, in particular, is the most widely used driving/tuning method in most existing graphene-based resonators. Although these actuation techniques have their merits (e.g. for some MEMS-based resonators), they have limitations also. For example, design complexity, nonlinearity, short circuiting and large driving voltage are the main disadvantages of electrostatic actuation [69]. Compared to MEMS structures that can be made suspended by etching the sacrificial layer underneath, graphene films transfer manually to the target substrate, which could lead to short circuiting if the transferred film bends downward.

Importantly, electrostatic actuation requires an actuation electrode separated from the suspended membrane by a distance of a few micrometres. The membrane is driven into resonance by inducing an electrostatic field between the suspended membrane and the bottom electrode. However, the resonators that have been fabricated for the work in this thesis do not include an actuation electrode as in electrostatic-based devices, and thus the

electrostatic actuation cannot be used. Instead, the devices have been designed in such a way that electrothermal transduction could be used effectively. Electrothermal actuation has the advantages of possessing simple design, achieving relatively large driving displacement when operated under low actuation voltage and therefore can be very efficient for vibration excitation.

2.7.1 Electrothermal actuation of graphene-PMMA

Compared to other conventional materials, graphene has superior thermal conductivity and a negative coefficient of thermal expansion (CTE) that make it a promising material for electrothermal actuation. Electrothermal actuation of a bilayer system relies on the difference in the coefficient of thermal expansion for different materials. When a film of graphene is integrated with another material with a different CTE, the graphene layer may act as a heating and conduction thin film simultaneously.

In electrothermal actuation, a physical expansion is induced by a local increase of temperature from the Joule heating phenomenon. Depending on the material thermal expansion, a transverse displacement can be achieved for single layer or multilayer structures. In this work, a bilayer structure consisting of graphene and PMMA membranes with different coefficients of thermal expansion has been used. The mechanical response of the system is illustrated schematically in [Figure 2.12](#).

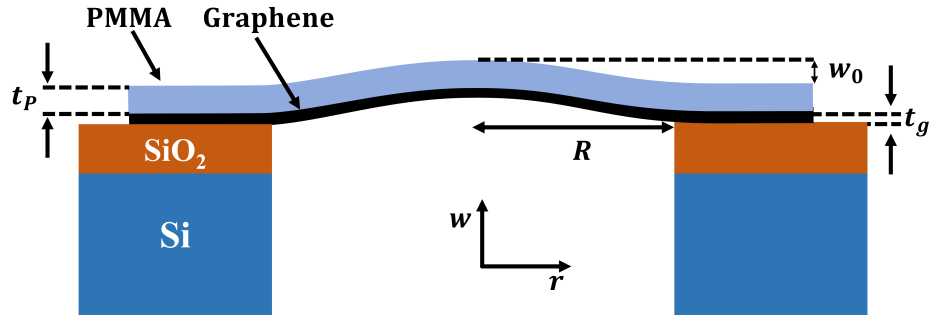


Figure 2.12: Schematic diagram of electrothermally actuated graphene-based resonators showing the mechanical deflection of the bilayer membrane suspended over a cavity of SiO₂/Si substrate.

When a voltage (V) is applied across the membrane, an electric current will pass through the membrane layers, and Joule heating will be generated. The generated heat causes a temperature

gradient (ΔT) within the bilayer structure. Due to the difference in the materials' CTE, the temperature gradient within the entire membrane thickness will induce a mechanical strain, hence a thermal tension in the membrane. Then, the thermally-induced stress will force the entire structure to expand/contract, resulting in a transverse mechanical deflection. For example, the deflection $w(r)$ at radial distance r from the centre of a thin circular membrane with radius R can be described as [70]

$$w(r) = w_0 \left(1 - \frac{r^2}{R^2}\right) \quad (2.21)$$

where w_0 is the maximum deflection at the centre of the membrane. For a square membrane with side length a , the assumed deflection in x-y direction can be expressed as follows [70]:

$$w(x, y) = w_0 \left(1 - 4\frac{x^2}{a^2}\right)^2 \left(1 - 4\frac{y^2}{a^2}\right)^2 \quad (2.22)$$

The change in the membrane deflection Δw depends on the temperature gradient ΔT and thermal expansion difference $\Delta\alpha$ of the materials. For example, a linear relationship between the deflection of a cantilever beam of graphene-epoxy and temperature has been reported [71]. The change in the average temperature can be influenced by the thermal conductivity and dissipated power. Since graphene has higher thermal conductivity than PMMA and due to the inverse proportionality of thermal response time τ to the average thermal diffusivity d_{avg} (i.e. $\tau = 1/d_{avg}$) [72], it is possible to achieve a fast thermal response (i.e. within the operational frequency range of 20 Hz - 20 kHz) to the conductive heat.

The bilayer membranes of graphene and PMMA can be driven into vibration by applying a combination of alternating current (V_{ac}) and direct current (V_{dc}) voltages across the membrane. It

is expected that there will be power dissipation in the membrane, which affects the Joule heating-induced force. The relationship between the applied voltage V and dissipated power P in a resistance R is given as $P = V^2/R$. In a similar way to electrostatic actuation (see [Equation \(2.20\)](#)), the vibration of the membrane can be identified from the peaks of large amplitude of oscillation that appear when the driving signal frequency is swept across the resonant frequency of the membrane.

2.8 Summary

In this chapter, a brief literature review of the development of acoustic transducers used in hearing aids systems and microphones has been given. In addition, design and analytical calculations based on clamped-clamped beams of tantalum and circular and square membranes of graphene have been described. Furthermore, a short description of electrostatic and electrothermal actuation of tantalum and graphene resonators has been outlined. The outcomes of this chapter are summarised as follows:

It is possible to make electromechanical resonators suitable for acoustic applications by considering a proper design and selecting appropriate materials. Tantalum and graphene have been chosen as structural elements for the design of two different types of resonators based on clamped-clamped beams and membranes in circular and square shapes. Compared to other metals, tantalum has unique mechanical properties that make it an ideal structural material for MEMS beams-based resonators. Analytical description of the influence of geometrical parameters on the resonant frequency of the resonators has been performed. For instance, it has been shown that the length and thickness characteristics of doubly clamped beams influence significantly the resonant frequency of the tantalum beam resonators. In order to achieve low resonant frequencies within the audible range, the analytical calculations have shown that the length of tantalum beams has to increase while decreasing the resonator thickness.

Graphene has special mechanical properties that enable tunable and highly sensitive graphene-based resonators to be fabricated and possibly used in a hearing aid device or an acoustic microphone. It has been shown analytically that the diameter, tension and number of layers of a circular thin-film of graphene plays an important role in

determining the resonant frequency of the resonators. For thin-films of graphene with a thickness of a few layers, it has been shown that graphene-based resonators are more likely to behave as membranes rather than plates.

Chapter 3

Fabrication and Characterisation of Tantalum Structures

3.1 Introduction

This chapter is devoted to the fabrication and characterisation of an array of suspended microstructures of tantalum. The first part of this chapter will be focused mainly on the influence of deposition conditions on the residual stress of sputtered tantalum thin-films. A general overview of thin-film stress will be given before describing the experimental procedure to fabricate tantalum thin films. Then, the influence of the deposition and post-deposition conditions on the residual stress of tantalum thin-films will be studied comprehensively. The second part of this chapter will be allotted to the realisation and mechanical static characterisation of suspended fixed-fixed beams of tantalum. The influence of film deposition and post-fabrication processes on the final structures of the fabricated beams will be investigated by using a deflection-based metrology. In addition to the experimental characterisations, analytical and numerical models will be employed to describe the final deflection profiles of the fabricated beams.

3.2 Thin film stress

Devices based on MEMS and NEMS rely on free-standing structures to produce mechanical vibration. The induced vibration is influenced by the geometrical design and mechanical properties of the suspended structure. For example, micromachined beams based on clamped-free and clamped-clamped structures are used as building-blocks for many MEMS-based vibrational devices [73]. The first step to create a suspended beam is to deposit a layer or layers of films on a substrate of interest. However, suspended beams face stress-related issues that can affect the device performance and reliability.

A residual stress is introduced to the beams material during the fabrication or post-fabrication processes. The mechanism by which the residual stress is developed in thin-film materials determines the nature of the stress. In general, the residual stress can be divided into intrinsic stress and extrinsic stress. The intrinsic residual stress, also known as growth stress, is generated from nucleation and growth processes during the film deposition on the substrate [74]. The degree of the intrinsic residual stress may vary when factors such as impurities and oxidation are incorporated. The extrinsic residual stress is generated in the film material due to post-deposition processing or when external factors such as chemical reaction and precipitation are imposed [75]. In addition to the intrinsic and extrinsic stresses, a thermal stress might be developed in a thin film material. The thermal stress, sometimes categorised as an example of the extrinsic residual stress, arises in the materials due to a mismatch in thermal expansion coefficients between the deposited film and the underlying substrate [76]. Therefore, the

total stress (σ) in thin-film materials can be expressed as follows:

$$\sigma = \sigma_{in} + \sigma_{ex} + \sigma_{th} \quad (3.1)$$

where σ_{in} , σ_{ex} , and σ_{th} are the intrinsic, extrinsic, and thermal stresses, respectively.

The deposited/grown films are usually stressed. The stress can be either tensile or compressive. As shown in [Figure 3.1](#), the film that tends to expand on a substrate is in the compressive stress state, while the film that tends to shrink is in the tensile stress state. Typically, the magnitude of the stress in thin films is within the range of MPa – GPa.

In some cases when the films are subjected to an extremely high level of stress, the resultant effects can be deleterious. For example, it is highly possible that film cracking will occur if the film is under high tensile stress [\[75\]](#). On the other hand, films that under high compressive stress are more susceptible to buckling delamination, peeling or blistering [\[75, 77\]](#). Overall, the presence of residual stress in thin films materials and subsequently suspended structures could degrade the functionality or modify the performance of the fabricated devices. An entire failure of devices is also possible if an excessive residual stress is developed. Therefore, investigating the residual stress is of great importance for successful operation and reliable performance of MEMS-based resonators.

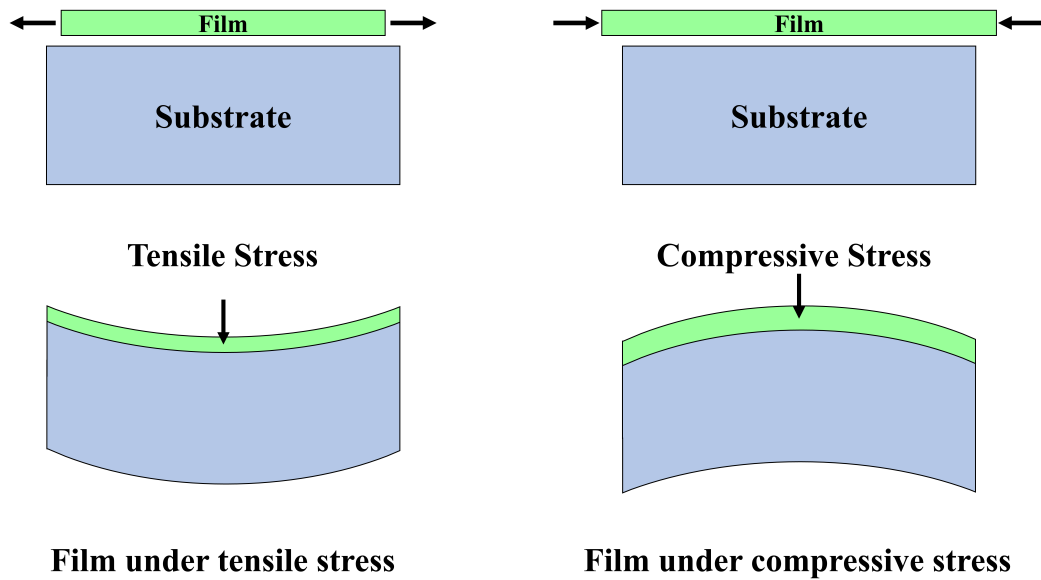


Figure 3.1: Illustration of compressive and tensile stresses developed during thin-film deposition on a substrate.

Prior to fabricating suspended microstructures of tantalum beams, the residual stress in tantalum thin films will be investigated. This is an important reliability matter because understanding how the residual stress is developed in tantalum thin-films will help in realising more robust structures. Also, a comprehensive study of the residual stress resulting from deposition processes will aid in controlling and optimising the fabrication process and therefore avoid possible mechanical failure. In the next sections, comprehensive investigations will be performed to explore the effect of deposition parameters and post-deposition conditions on the development of residual stresses in tantalum thin films. After characterising the thin films stresses, tantalum suspended microstructures will be fabricated, and their final deflection profile will be characterised from stress effects points of view.

3.2.1 Residual stress of tantalum thin film

In the previous chapter, it has been shown that tantalum metal is a suitable material for low frequency-operated resonators. It is expected that the audio frequency can be achieved by choosing the proper design and dimensions. To fully exploit the excellent properties of tantalum, it is necessary to investigate and control stress-related effects.

One of the main obstacles that may lead to functional failure in a device based on tantalum is the residual stress of the metal material. For example, issues such as wafer curvature, buckling delamination, films cracking and a change in the device functions have been attributed to undesirable stress effects [78, 79]. In fact, despite numerous attempts to characterise the stress in thin-film materials, the real mechanism is not well understood. Several approaches have been reported to control the residual stress or improve the physical properties of a tantalum thin-film for a specific application. It has been found that the residual stress and crystallographic structure of tantalum thin-films can be manipulated in various ways, such as annealing at different temperatures, using different substrates and deposition techniques and changing the deposition conditions.

Extensive efforts have been made to investigate the influence of the annealing process, thermal cycling and oxygen diffusion on the intrinsic stress and phase transformation between alpha (α) and beta (β) of tantalum thin-films [80–85]. In addition, the residual stresses of tantalum films have been examined by taking into consideration the effect of the underlying substrate. For these investigations, tantalum thin-films have been deposited on different substrates including silicon [80, 81], silicon dioxide [80, 82], stainless steel [56, 86], glass [79, 87] and titanium [88]. Furthermore, the residual stress of tantalum thin-films has been studied as a

function of substrate bias voltage [57, 86], film deposition system [57, 84, 86, 87, 89], film deposition conditions [84, 87, 90–92], substrate temperature [57], ion bombardment [93] and film thickness [56, 78].

However, previous studies have limited their research to a particular aspect of films deposition or annealing conditions and the conditions' influence on the phase transformation of the tantalum films. This work aims to provide a comprehensive investigation of the residual stress of tantalum thin-films as a function of sputtering (deposition) conditions, annealing treatment and exposure of annealed and unannealed films to atmospheric ambient and ion bombardment exposure. Importantly, the main objective of this study is to identify the conditions of sputtering, annealing and air or ion bombardment exposures under which the residual stress will behave in a more compressive or tensile manner.

3.3 Fabrication of tantalum thin-films

To evaluate how the residual stress develops in tantalum thin-films due to the effect of the fabrication process, a set of tantalum thin-films has been deposited on a substrate using different deposition parameters. The fabrication steps of tantalum thin-films are shown in Figure 3.2. To begin with, about a 500-nm-thick layer of silicon dioxide has been grown thermally on both sides of a silicon substrate (4-inch, p-type), Figure 3.2a. The purpose of oxide growth step is to obtain a clear measurement of the substrate curvature.

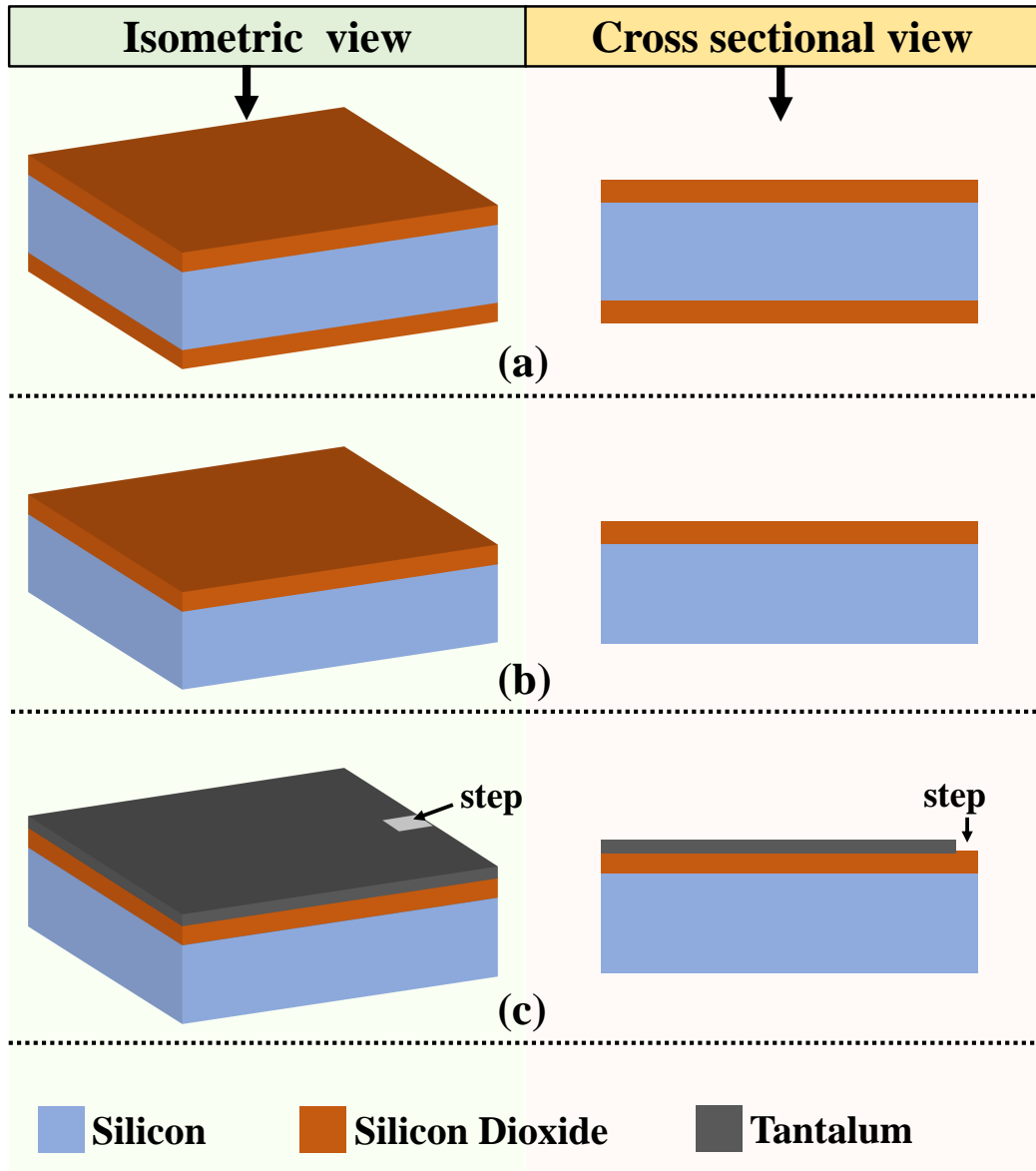


Figure 3.2: Fabrication process flow for tantalum thin-film. (a) Silico dioxide grown thermally. (b) Back side oxide etched. (c) Tantalum thin-film sputtered. A step has been created by attaching a polyimide tape on the substrate, which can be removed after film deposition.

Next, the backside of the oxide has been etched via reactive ion etching (RIE), see [Figure 3.2b](#). Before the thin-films deposition step, an initial curvature measurement has been performed. Then, a set of 50-nm-thick films of tantalum have been sputtered on the top oxide using a DC magnetron sputtering system, see [Figure 3.2c](#). The sputtering conditions parameters are presented in [Table 3.1](#). In this process, a step has been created which enables film thickness

to be measured by atomic force microscopy (AFM) and a Dektak profilometer.

Table 3.1: Sputtering parameters of tantalum thin-films in DC magnetron system using argon (Ar) as sputtering gas with flow rate of 50 sccm.

Sample number	Power (W)	Pressure (mTorr)
1	300	3.5
2	300	7.5
3	300	11.5
4	300	19
5	300	24
6	400	3.5
7	400	7.5
8	400	11.5
9	400	19
10	400	24
11	500	3.5
12	500	7.5
13	500	11.5
14	500	19
15	500	24

3.4 Characterisation of tantalum thin-films

The residual stress of tantalum thin-films has been investigated as a function of five parameters: sputtering pressure, sputtering power, annealing at different temperatures, exposure to ambient conditions and exposure to ion bombardment. For sputtering pressure and sputtering power experiments, 15 samples have been used. For the rest of other experiments, 5 samples have been utilised for each experiment.

3.4.1 Stress measurement procedure

The present work utilises the curvature method to determine the total residual stress of tantalum thin-films. After removing the backside layer of the oxide, an initial set of curvature measurement has been performed using a profilometer. For this step, the initial substrate radius of curvature has been measured. After the films deposition, a second set of curvature measurement has been carried out and the radius of curvature of the thin-film on the substrate has been measured. To estimate the residual stress of the thin-films (σ^f), Stoney's formula has been used as follows:

$$\sigma^f = \frac{E_s t_s^2}{6(1 - \nu_s) t_f} \left(\frac{1}{R_{s+f}} - \frac{1}{R_0} \right) \quad (3.2)$$

where E_s is Young's modulus of the substrate (MPa), ν_s is Poisson's ratio of the substrate, t_s is the substrate thickness (μm), t_f is the film thickness (μm), R_0 is the initial substrate radius of curvature (μm) and R_{s+f} is the final radius of curvature (μm) of the substrate plus the thin-film.

3.4.2 Effect of sputtering pressure and power

The residual stress measurements of as-deposited tantalum films as a function of sputtering pressure for powers of 300, 400 and 500 W are shown in [Figure 3.3](#). Three main regions of the residual stress in the films are shown in the figure: compressive stress (regions **a** and **c**) and tensile stress (region **b**). It can be seen that the effect of sputtering power on the degree of residual stress in the films have been found to be significantly larger in the tensile state region. In the compressive stress regions, on the other hand, increasing the power has produced a slight change in the residual stress of the

films.

Consistent with literature findings [60, 90, 91, 94], the residual stress has been observed in a compressive state (region **a**) at low pressure (3.5 mTorr) and as the sputtering pressure increases, the trend of stress has been observed to switch to a tensile state (region **b**) at pressures of 7.5 and 11.5 mTorr before shifting back again to the compressive state (region **c**) at pressure of 19 and 24 mTorr.

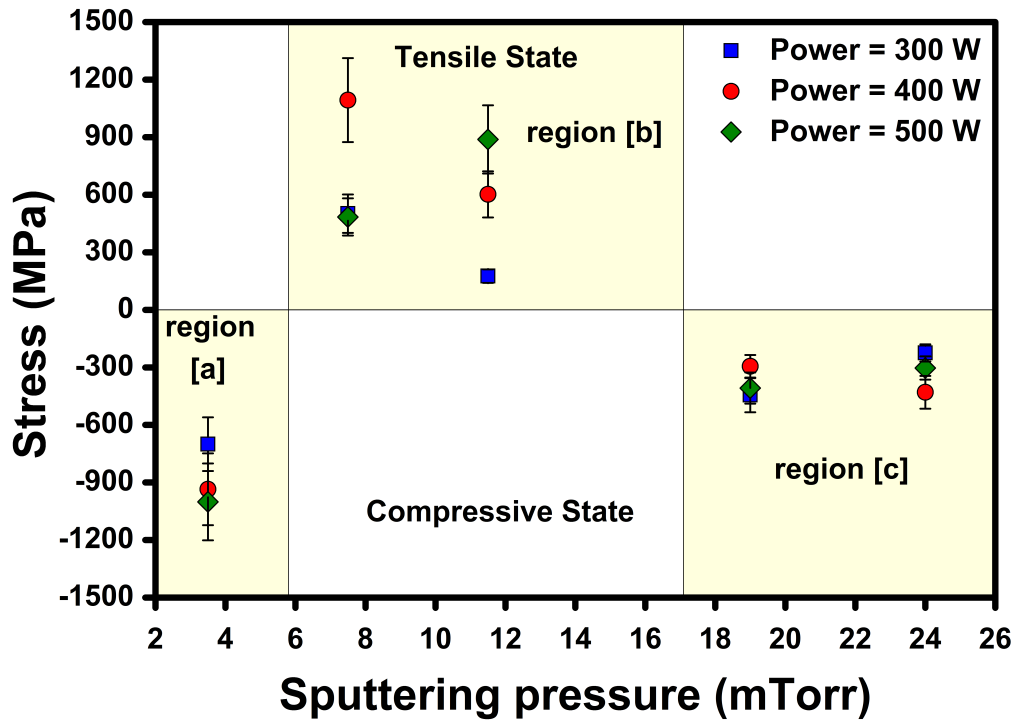


Figure 3.3: The residual stress of tantalum thin-films as a function of sputtering pressure for different sputtering powers. A standard deviation of 30 MPa, 50 MPa and 28 MPa has been estimated for sputtering power and pressure measurements at regions **a**, **b** and **c**, respectively.

The mechanism that lead to compressive or tensile stresses is somehow relevant to the adatom surface mobility of the used materials. The compressive stress exhibited in tantalum thin-films at low sputtering pressure (region **a**) could be because of the atomic peening. The atomic peening mechanism has been described in more detail elsewhere [87, 92, 95]. In such a scenario, the argon and target atoms have long mean free path and high momentum with fewer

collisions, thus causing a compressive stress in the deposited film. Therefore, the compressive-stressed film at low sputtering pressure might have dense fibrous structures as described by Yoshihara et al. [96].

In the second region (b), the stress of tantalum films is observed to change from compressive to tensile at sputtering pressure of around 7.5 mTorr. It seems that the tensile-stressed films could possess ultra-small columnar grains with low density grain boundaries at the film/substrate interface, and this abrupt transition toward the tensile state region could be attributed to constrained grain boundary relaxation [94]. In addition, this transition in the stress between compressive and tensile stress states could be associated to phase transformation between α and β as reported previously [56, 90]. For instance, Navid and Hodge [90] have found that the α phase has been developed in the compressive region, whereas β or mixed phases have been developed in the tensile state.

The third region of transition from tensile to compressive stress at higher sputtering pressures (19 and 24 mTorr) could be related to the mechanism of impurity incorporation, where oxygen-based contaminants are desorbed from the deposition chamber [91, 95]. In general, at high deposition pressure (from 11.5 to 24 mTorr), energy and flux of particles are decreased because of the increase of collisions with non-directional ion bombardment. Consequently, adjacent columnar grains and porous microstructures are developed.

3.4.3 Effect of annealing in oxygen ambient

Annealing is another parameter that can affect the residual stress of the deposited films. Figure 3.4 shows the measured residual stress

as a function of sputtering pressure for tantalum films annealed at different temperatures. Firstly, the stress measurement of the as-deposited thin-films has been carried out at room temperature (24 °C). After that, the sputtered thin-films have been subjected to annealing processes at temperatures of 90, 150, 200 and 300 °C in oxygen ambient. The residual stress measurements of the annealed films have been performed directly after each annealing step. It can be seen that the impact of annealing on the change in the residual stress is largest for films deposited at lower pressure (3.5 – 11.5 mTorr) and annealed at 300 °C.

The transition towards the compressive stress at low sputtering pressures could be attributed to the formation of a tantalum pentoxide Ta_2O_5 layer at the film surface because of the ability of oxygen content to penetrate easily into the unit cell of the films during annealing [91]. It is possible that the amount of Ta_2O_5 increases as the annealing temperature increases and therefore increases the compressive stress [83]. In the case of the films that have been deposited at higher sputtering pressure (19 and 24 mTorr), the stress tends to be less compressive after annealing treatment at 300 °C. These observations could be related to the annealed columnar structures that prevent the oxygen diffusion from penetrating easily into the grain boundaries [96]. However, many published works have revealed different interpretations on the relationship between stress shifting and phase transformation. It is possible that phase transformation may take place at high annealing temperatures up to 600 °C [81]. Since the tantalum films in the present study have been sputtered on a SiO_2/Si substrate, there is a possibility that $\alpha\text{-Ta}$ might react with the thermal oxide, and hence layer of Ta_2O_5 and Ta_5Si_3 are created [82]. However, the process in which oxygen atoms to diffuse into the tantalum layer by penetrating the native oxide can only occur at high annealing

temperatures as reported [80–82]. Therefore, it seem unlikely that a phase transformation can take place at an annealing temperature of only 300 °C.

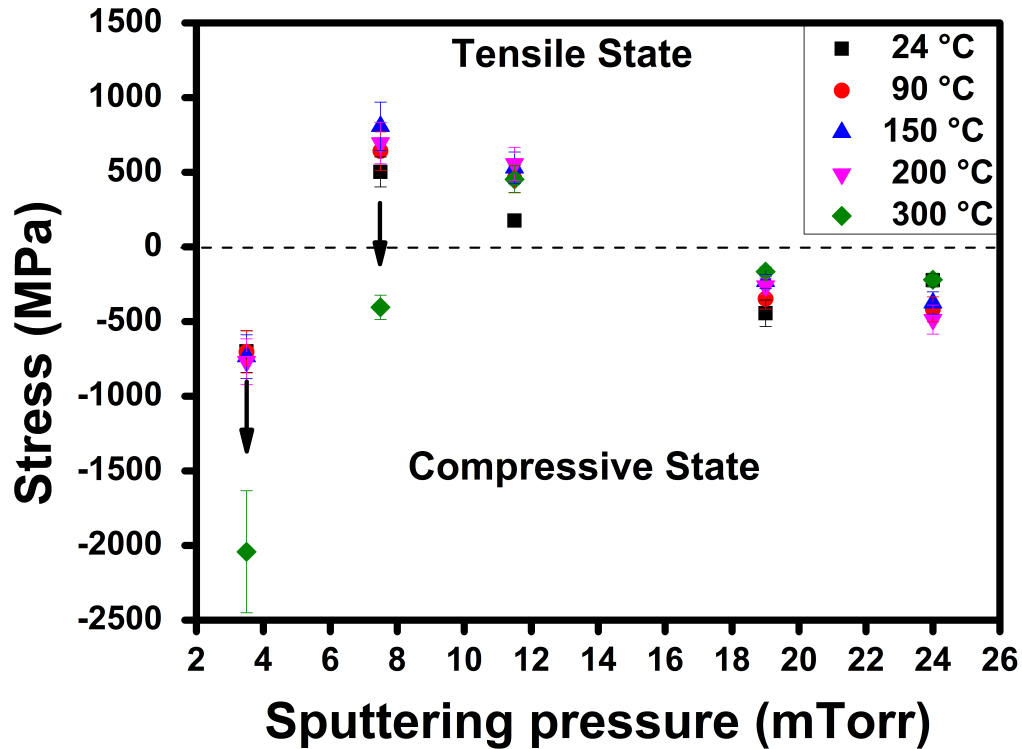


Figure 3.4: The residual stress of tantalum thin-films as a function of sputtering pressure for tantalum films annealed at different temperatures. The sputtering power of the deposited films is 300 W. Arrows indicate shifting of the residual stress of the thin-films deposited at low pressure. A standard deviation of 35 MPa has been estimated.

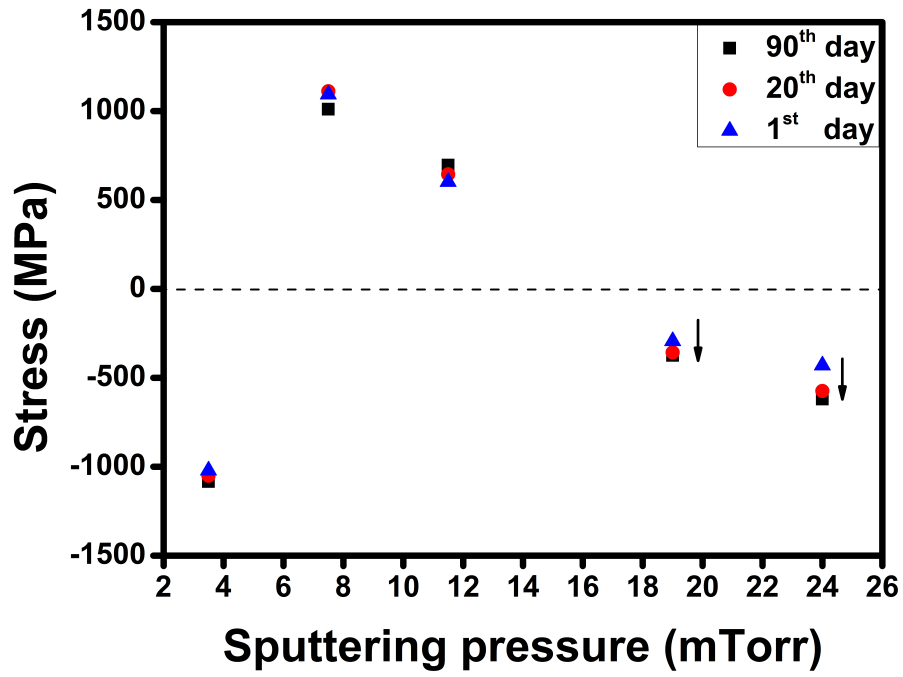
3.4.4 Effect of atmospheric exposure

The realised devices will be exposed to different external environmental conditions during or after the fabrication process. The exposure to atmospheric conditions may change the characteristics of the device. Therefore, further investigation has been performed to examine the impact of atmospheric conditions on the residual stress of both annealed and unannealed films. The measured stress with respect to the sputtering pressure for different exposure time of unannealed and annealed films is shown

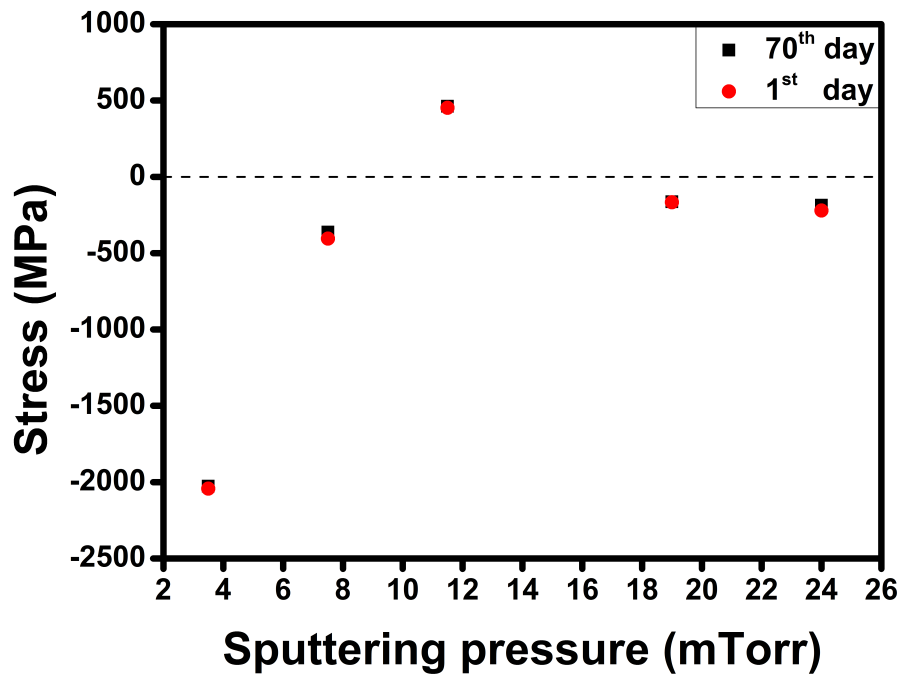
in [Figure 3.5](#).

In the case of the unannealed films, three main measurements of stress have been carried out in cleanroom ambient at 24 °C: after deposition directly, after 20 days and after 90 days, see [Figure 3.5a](#). For all exposure periods, a modest change has been observed in the residual stress of the unannealed films that have been deposited at low sputtering pressure. However, the films that have been deposited at higher pressures, i.e. 19 and 24 mTorr, exhibit a noticeable increase in the compressive stress after 90 days of the exposure. For example, the residual stress at 24 mTorr has been observed to shift from -430 MPa on the first exposure day to -620 MPa on the 90th day.

In the case of the annealed films (at 300 °C only), residual stress measurements have been conducted in cleanroom ambient at 24 °C on the first and the 70th day after the annealing process, as shown in [Figure 3.5b](#). In fact, no significant change has been observed in the films after 70 days of the exposure. For example, a small shift in the compressive stress from -180 MPa on the first day to -220 MPa on the 70th day has been observed for annealed films deposited at 24 mTorr. As reported [[57](#), [60](#)], the residual stress of tantalum thin-films can be minimised or will remain stable over time after annealing the films at temperature of 300 °C or higher. It is also possible that exposing the films to ambient conditions for long time (device reliability) could have the same effect obtained through annealing.



(a) Unannealed films



(b) Annealed films

Figure 3.5: The residual stress as a function of sputtering pressure for (a) unannealed and (b) annealed films exposed to atmosphere. The sputtering power of the as-deposited films is 300 W. Atmospheric exposure for annealed films has been performed for the films annealed at 300 °C only. Arrows indicate shifting of the residual stress. A standard deviation of 25 MPa has been estimated.

Our results agree with the general trend of stress that has been reported by Yoshihara and Suzuki [96], where the as-deposited films at low pressure might have fibrous structures, while the films deposited at high pressure could possess columnar structures. As a result, the fibrous structures in the thin-films could hinder the oxygen diffusion from penetrating freely into the grain boundaries as a function of time. In this case, no highly influential stress will be developed in the thin-films. On the other hand, the columnar structures in the unannealed films could allow a quick diffusion along the grain boundaries of tantalum thin-films and show a distinguishable increase in the compressive stress when exposed to atmosphere for a long time. It may appear that the annealing process makes both the fibrous and the columnar structures less permeable to oxygen diffusion as a function of time. To fully understand the mechanism behind the observations reported here, further investigations could be a potential future work.

3.4.5 Effect of Argon energy exposure

Energetic particles play an important role in fabrication processing systems and can affect the characteristics of the involved materials. The residual stress of thin-films can be modified by exposing the film to energetic particles. Therefore, an inert-gas of argon (Ar) has been employed to investigate the effect of ion bombardment on the residual stress relaxation of tantalum thin-films. [Figure 3.6](#) compares the stress measurements for unexposed and exposed films to different ion bombardment parameters.

In general, all exposure conditions have been found to exhibit a change towards the compressive stress region. For example, with the use of an exposure power of 100 W and a flow rate of 20 sccm, the residual stress has been found to become more compressive by

around two orders of magnitude compared to the unexposed films, see [Figure 3.6a](#). When the exposure power is doubled to 200 W while keeping the Ar gas flow rate at 20 sccm, a significant shift of the residual stress towards the compression region has been observed, see [Figure 3.6b](#). For instance, the film deposited at 7.5 mTorr has exhibited a shift in the residual stress from + 1000 MPa in the tension side (unexposed) to – 475 MPa in the compression side (exposed).

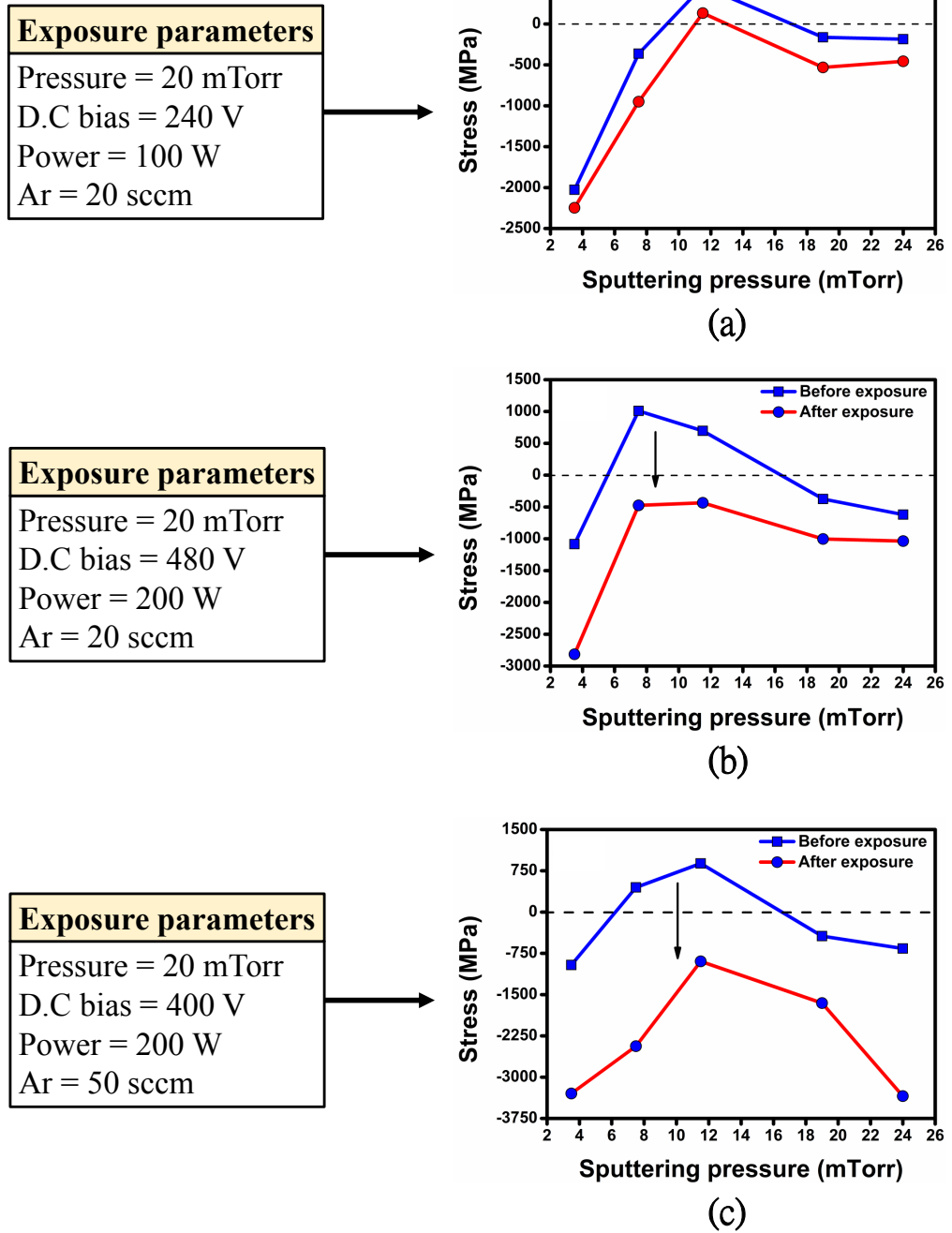


Figure 3.6: Comparison of tantalum thin-films residual stress as a function of sputtering pressure for different conditions of exposure to ion bombardment. Arrows indicate shifting of the residual stress. A standard deviation of 50 MPa has been estimated.

In addition to the exposure power effect, the flow rate of the inert gas is another influential parameter. The increase of Ar flow rate to 50 sccm leads to an extreme shift towards the compression state region, as shown in [Figure 3.6c](#). Under these exposure conditions, the residual stress of exposed films becomes more compressive by more than three orders of magnitude compared to the unexposed films. Such observations suggest that a stress relaxation might occur depending on the degree of ion bombardment on the surface of tantalum thin-films, whereby the atoms of the material surface are affected by the energy and the amount of bombardment [93, 97].

Based on all the aforementioned observations, it is concluded that the residual stress of tantalum thin-films can be controlled and possibly minimised by controlling the fabrication process conditions. The investigation has shown how the fabrication conditions such as sputtering conditions, annealing treatment, oxygen exposure and ion bombardment exposure influence the residual stress developed in the deposited films of tantalum. The observed behaviour will be employed in the next part of this chapter to study the effect of stress on the final structure of beam-based devices of tantalum. The anticipated outcomes of the present work are very valuable and could be employed in the fabrication of stress-free or stress-controlled structures for more reliable sensing and actuation applications.

3.5 Suspended beams of tantalum

Suspended microstructures are essential elements for resonance-based devices. Suspended structures based on microbeams have been extensively used in a wide range of MEMS devices for different application areas including pressure

sensors [98] , electrostatic actuators [99], RF switches [100] and resonant gate transistors [59]. From design and performance points of view, doubly clamped beams are possible structures for dynamic vibration of actuators and sensors in resonant MEMS devices. The performance of suspended structures can be affected when stress-related deformations such as buckling and bending are produced in the final fabricated structure. Moreover, the beams might break when an extreme stress develops in the beam material. Such stress-related deformations are generated during thin-film deposition or post-fabrication processes. Therefore, the residual stress in tantalum metal beams is a problematic issue and can influence the performance and stability of the final fabricated devices.

3.5.1 Stress-related deflection

In order to obtain robust and reliable resonator devices, the mechanical properties of structural metal beams should be improved by controlling the residual stress that develops in tantalum metal beams. Although there has been plenty of research on analysing or controlling the residual stress in different materials [60, 101–109], the behaviour of beams based on compressive or tensile-stressed films under different etch release conditions has not yet been addressed in the literature. Moreover, the deflection profile of structural metal materials such as tantalum has not been studied satisfactorily as much as semiconductor processing materials such as Si, SiO₂ and Poly-Si.

The performance of suspended structures can be affected when stress-related deformations such as buckling and bending are produced in the final fabricated structure. Moreover, the beams might break when an extreme stress develops in the beam material.

Such stress-related deformations are generated during thin-film deposition or post-fabrication processes. Therefore, the residual stress in tantalum metal beams is a problematic issue and can influence the performance and stability of the final fabricated devices.

In the first part of this chapter, it has been shown that the residual stress of tantalum thin-films depends strongly on sputtering conditions and other fabrication processing parameters. Here, in the second section of this chapter, the influence of deposition and post-fabrication processes on the final mechanical structure of tantalum microbeams will be investigated. In other words, the final deflection profiles of doubly clamped microbeams made from compressive and tensile-stressed films will be studied experimentally. Also, the effect of wet and dry etching processes on the final deflection profile of the fabricated microbeams will be examined. In addition, an optimum finite element model will be developed to predict numerically the buckling behaviour of the produced beams by considering the boundary conditions in the form of a compressive stress and an applied load. Further investigation will be performed to examine the influence of beam geometry, length, width and thickness on the final deflection profile of the fabricated and simulated structures.

3.5.1.1 Buckling analysis

For a clamped-clamped beam structure ([Figure 2.6](#)), the fixed ends have stringent configuration, and thus the axial residual stress cannot be relaxed. However, buckling takes place when the axial load exceeds the Euler buckling limit and the beam will be under compressive stress. The Euler buckling limit (P_c) of

clamped-clamped beams is given as follows [102]:

$$P_c = \frac{4\pi^2 EI}{l^2} \quad (3.3)$$

where l and EI are respectively the length and flexural rigidity of the beam. The buckling occurs at a particular length according to the critical stress (σ_{cr}):

$$\sigma_{cr} = \frac{E\pi^2 t^2}{3l^2} \quad (3.4)$$

where E, t, l denote respectively the elastic modulus, thickness and length of the beam. Therefore, once the beam is released from the substrate, it will buckle according to the magnitude of the residual stress (σ_{ris}) as follows:

$$\sigma_{ris} = -\frac{\pi^2 E}{l^2} \left[\frac{A^2}{4} + \frac{t^2}{3} \right] \quad (3.5)$$

where A is the amplitude of buckling. Note that the buckling takes place when the residual stress exceeds the critical stress (i.e. $\sigma_{ris} > \sigma_{cr}$).

3.5.2 Beams fabrication procedure

To fabricate suspended microbeams of tantalum, a sacrificial layer is required to be deposited beneath the structural layer. As the sacrificial layer is etched, the structural layer will be suspended freely. For the fabrication of the devices in this work, a low stress polymer of polyimide and plasma-enhanced chemical vapour deposition (PECVD) of silicon oxide (SiO_2) have been used as sacrificial layers. Surface micromachining methods have been utilised to fabricate an array of fixed-fixed beams of tantalum on a 4-inch p-type (100) silicon wafer. The fabrication process flow is

shown in Figure 3.7. As mentioned earlier, the microbeams will be made from tensile and compressive-stressed films. The deposition parameters of the deposited films are provided in Table 3.2.

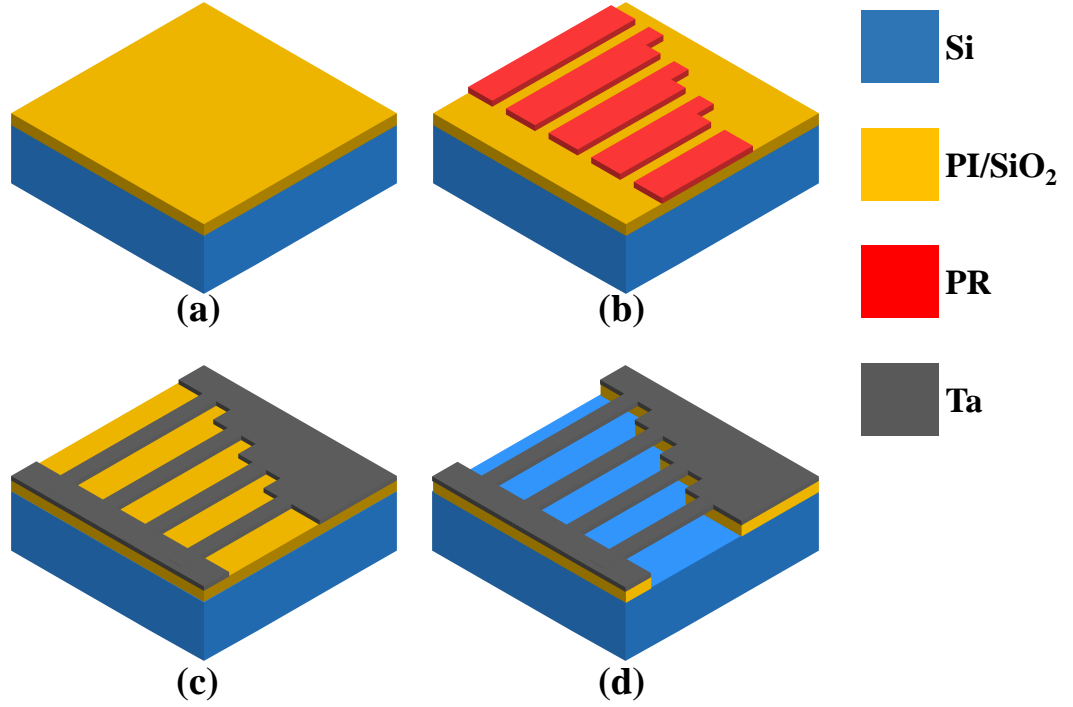


Figure 3.7: Fabrication process flow for an array of fixed-fixed microbeams of tantalum. (a) Sacrificial layer of polyimide (PI) or silicon dioxide (SiO_2) applied. (b) Photoresist (PR) spin coated and patterned. (c) Tantalum sputtered, and microbeams patterned. (d) Sacrificial layer etched, and beams released.

Table 3.2: Sputtering parameters of tantalum films and their thicknesses and initial stress states.

Sputtering power (W)	Sputtering pressure (mTorr)	Film thickness (nm)	Film stress
300	7.5	500	tensile
300	11.5	500	tensile
300	19	500	compressive

3.5.2.1 Polyimide as sacrificial layer

For the first sacrificial layer, an approximately 8- μm -thick layer of polyimide has been spin coated (Figure 3.7a) and soft-baked

on a hotplate at 90 °C and 150 °C for 90 sec. To remove any solvents and imidise the polyimide completely, the films have been subjected to a curing temperature of 350 °C for 30 minutes. In this step, the temperature has been set to increase slowly at a rate of 4 °C/minute, and then cool down to room temperature. Afterwards, a 3- μ m-thick layer of photoresist has been coated and patterned photolithographically (Figure 3.7b). Tantalum films with thickness of 500 nm have been deposited using a DC magnetron sputtering system, according the sputtering parameters presented in Table 3.2. Once the deposition step has been performed, a lift-off process has taken place to define the fixed-fixed beams, thus exposing the polyimide layer underneath the metal (Figure 3.7c). Thereafter, the beams structure has been released (Figure 3.7d) by etching the polyimide with two dry-based etching systems; oxygen plasma-ashing (Barrel Asher) and oxygen plasma-downstreaming (MEMSSTAR).

3.5.2.2 Silicon oxide as sacrificial layer

For the second sacrificial layer, \sim 3- μ m-thick layer of silicon oxide has been deposited at a low temperature of 120 °C using a PECVD system. The same photolithography and deposition processes as in the polyimide case have been applied. The oxide layer has been etched isotropically by a wet etching process in diluted buffered hydrofluoric acid (BHF). After the etching step, the samples have been transferred and soaked in the following order: in deionised water (DI) for 10 minutes, isopropanol (IPA) for 5 minutes and methanol for 10 minutes. The final release stage has been carried out in a critical point dryer chamber and left to dry.

Based on the fabrication procedures mentioned, an array of fixed-fixed structures of tantalum microbeams with a width of 15

μm , a thickness of 500 nm and lengths of 100, 200, 300 and 400 μm have been created.

3.6 Beams Characterisation

After the fabrication procedure, the fabricated beams have been characterised to inspect whether the beams are released completely. In addition, the effects of stress and other fabrication-related factors have been investigated and analysed.

3.6.1 Deflection measurements

A scanning electron microscope (SEM) and a white light interferometer (WLI, Zygo) have been used to verify the complete release of the microbeams. [Figure 3.8](#) shows SEM images of an array of the released fixed-fixed microbeams after the removal of the sacrificial layer.

It can be visually verified that the sacrificial layer has been removed completely and the fabricated beams are released fully by observing suspended structures along the beams length. All fabricated beams have demonstrated vertical deflection along the length. However, the tantalum microbeams that have been released in a dry etching process ([Figure 3.8a](#), [Figure 3.8b](#)) have been found to exhibit larger vertical deflection than the beams released in a wet etching process ([Figure 3.8c](#), [Figure 3.8d](#)).

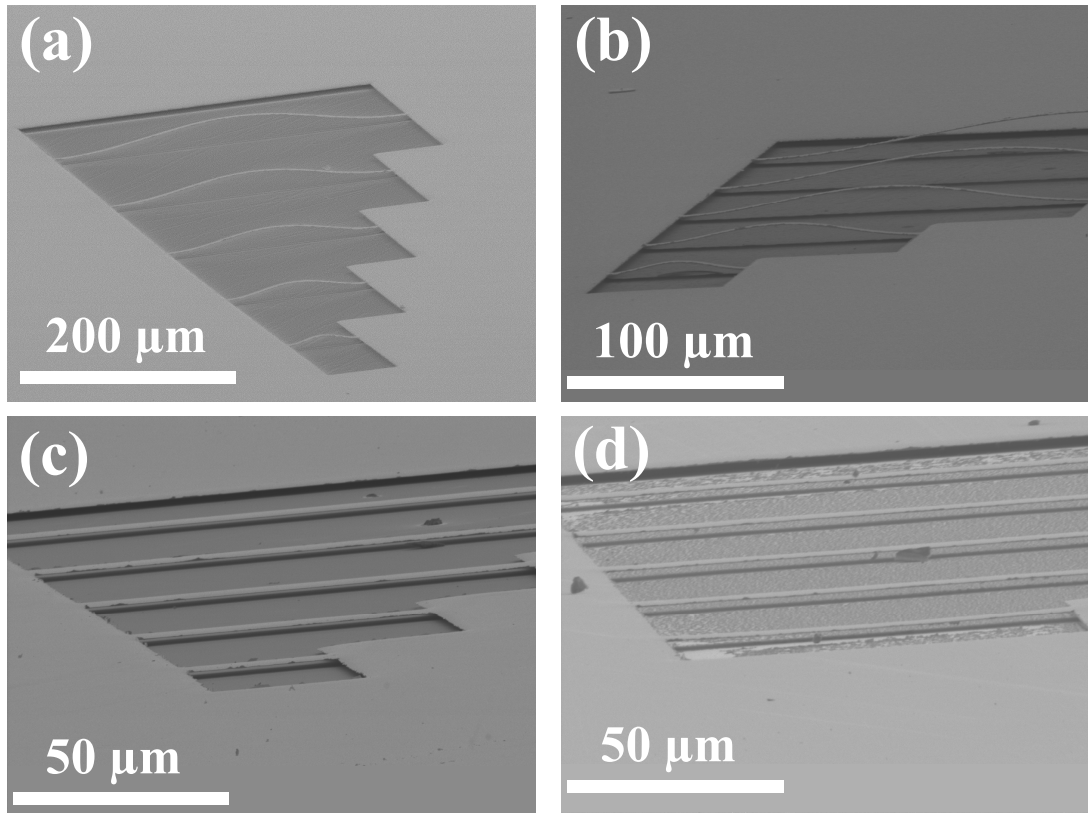


Figure 3.8: SEM images of suspended microbeams of tantalum after removing the sacrificial layer using dry-etch release (a, b) and wet-etch release (c, d).

To determine the final deflection profile of the fabricated beams, optical measurements have been performed using a WLI that can precisely measure the actual profile of the suspended devices. Figure 3.9 illustrates 3D reconstructed interferometry images of tantalum beams with lengths ranging from 100 to 400 μm . The illustrated microbeams are released in a dry etching process. A clear vertical deflection along the beams length can be observed. It seems that the beams exhibit upward buckling deformation. The optical measurements have been applied for all fabricated beams. Based on the profiles obtained from the interferometry output, the deflection amplitude of suspended beams has been evaluated.

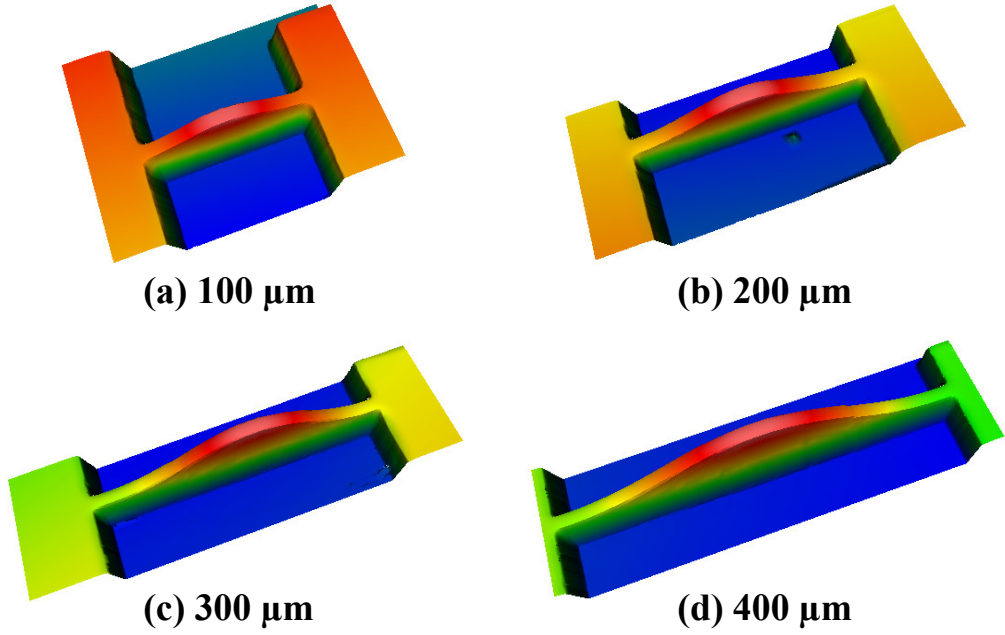


Figure 3.9: Examples of reconstructed 3D topology images of white light interferometry measurements of tantalum beams after removing the sacrificial layer. The interferometry images show the deflection profile of microbeams with lengths of 100, 200, 300 and 400 μm .

3.6.2 Initial residual stress measurement

The initial stress measurements of as-deposited films have been conducted according to Stoney's curvature method, see [Equation \(3.2\)](#). To determine the residual stresses of the suspended beams, [Equation \(3.5\)](#) has been used. First, the deflection profile of the released beams has been measured. Then, the maximum deflection (A) of the beams has been extracted from the interferometry data. The maximum amplitude of beams buckling deflection has been measured for the highest deflected points at the middle section of the beam. The maximum vertical deflection and residual stress for different microbeams made from compressive and tensile-stressed films and released in wet and dry-etch release processes are shown in [Table 3.3](#). The material properties of tantalum used in the residual stress calculations are

Young's modulus of 176 GPa [89] and Poisson's ratio of 0.34. The beam dimensions that have been used are a width of 15 μm and a thickness of 0.5 μm .

Table 3.3: The maximum deflection (A) and residual stress (σ_{ris}) measured for 400- μm -long beams made from tensile and compressive stressed-films and released in wet and dry etching.

Beams fabrication parameters	l (μm)	Experimental	
		A (μm)	σ_{ris} (MPa)
Tensile-stressed films (wet)*	400	8.40	-192.21
Tensile-stressed films (dry)*	400	12.70	-438.22
Tensile-stressed films (dry-O ₂ ashing)**	400	12.81	-445.83
Tensile-stressed films (dry-O ₂ downstream)**	400	16.96	-780.81
Compressive-stressed films (wet)	400	23.90	-1549.67
Compressive-stressed films (dry)	400	24.51	-1629.74

*Beams made from films deposited at sputtering power of 300 W and sputtering pressure of 7.5 mTorr.

**Beams made from films deposited at sputtering power of 300 W and sputtering pressure of 11.5 mTorr.

It can be seen that the amplitude of buckling deflection of the microbeams made from compressive-stressed films is greater than that of beams made from tensile-stressed films. In addition, the microbeams that have been released in a wet-etch release process have produced smaller buckling deflection than that of beams released in a dry-etch release process. For example, microbeams made from the same tensile stressed-films have been found to exhibit a maximum buckling deflection of ~ 8 μm in the wet-etch release process and ~ 13 μm in the dry-etch release process. As the deflection amplitude increases, the residual stress increases accordingly. Since all the fabricated beams exhibit buckling, the corresponding residual stress developed in the suspended beams is

compressive.

3.6.3 Model description: mechanical static analysis

Although the maximum deflection and residual stress of tantalum microbeams can be estimated analytically using [Equation \(3.5\)](#), differences, however, have been observed between the experimental and the analytical results. In other words, the unusual buckling profile that have been produced in the fabricated beams cannot be fitted with the simple model that only takes into account the compressive stress effect.

To understand the mechanism of buckling in beam-like structures, several models have been reported in the literature. In these models, the focus has been aimed towards predicting the buckling behaviour of a suspended microbeam (microbridge) as a result of either the fixed boundary conditions (clamped structures) and gradient residual stress effects [[102](#), [104](#)], or flexible boundary conditions (non-ideal clamping) plus the mean residual stress and/or gradient residual stress components [[107](#)]. However, only the direction (upward or downward) and the amplitude of buckling were evaluated. In particular, the effects of post-processing and the externally applied load on the final shape of beams deflection have not been considered in these studies.

In order to predict closely the final deflection profile observed in the fixed-fixed beams reported here, several numerical models have been developed using a finite element analysis (FEA) software package (CoventorWare). The models are illustrated schematically in [Figure 3.10](#). Note that the purpose of the developed models is apply different boundary conditions in such a way that the numerical model fit the measured profile empirically.

In the proposed models, a compressive residual stress has been included in the material property and an external load has been applied to produce various boundary conditions to determine the direction, amplitude and shape of the buckling profile. From an experimental point of view, the external mechanical load can result from undercut etching, solvent surface tension during drying, surface oxidation and other post-processing effects. The values of the compressive residual stress and mechanical load used in the developed models are presented in [Table 3.4](#).

Table 3.4: Comparison of the maximum deflection (A) simulated with different models using compressive stress (σ) and different values of load (P_{un} , P_{cn} and P_{ed}) applied along the beam length.

Model	σ (MPa)	P_{un} (MPa)	P_{cn} (MPa)	P_{ed} (MPa)	A (μm)	MAE*
Model-a	-470	0.12	-	-	14.42	2.27
Model-b	-470	-	0.12	-	13.68	1.12
Model-c	-470	-	-	0.12	8.73	12.97
Model-d	-470	0.12	-	-	14.71	3.46
Model-e	-470	-	0.12	-	13.78	1.38
Model-f	-470	-	0.12	0.045	12.87	0.18

*Mean Absolute Error (MAE) included to compare the fitting of each model with the experiment.

The simulation has been performed for 400- μm -long beams only. To estimate the buckling profile precisely, the compressive residual stress values applied in the models (-470 MPa) are slightly larger than those observed by experiment (-445 MPa). [Figure 3.11](#) shows the experimentally observed buckling profile of doubly clamped beam with a length of 400 μm , width of 15 μm and thickness of 0.5 μm fitted with the simulated profile of **Models a, b, c, d, e** and **f**.

In the case of **Models- a, b, d** and **e**, a compressive stress of $-$

470 MPa and an external load of 0.12 MPa distributed load along the beam bottom have been applied. The vertical deflection of these models is upward and larger than the measured one. Importantly, the corresponding simulated buckling profile is a dome-like shape, which is different from the buckling shape observed by experiment.

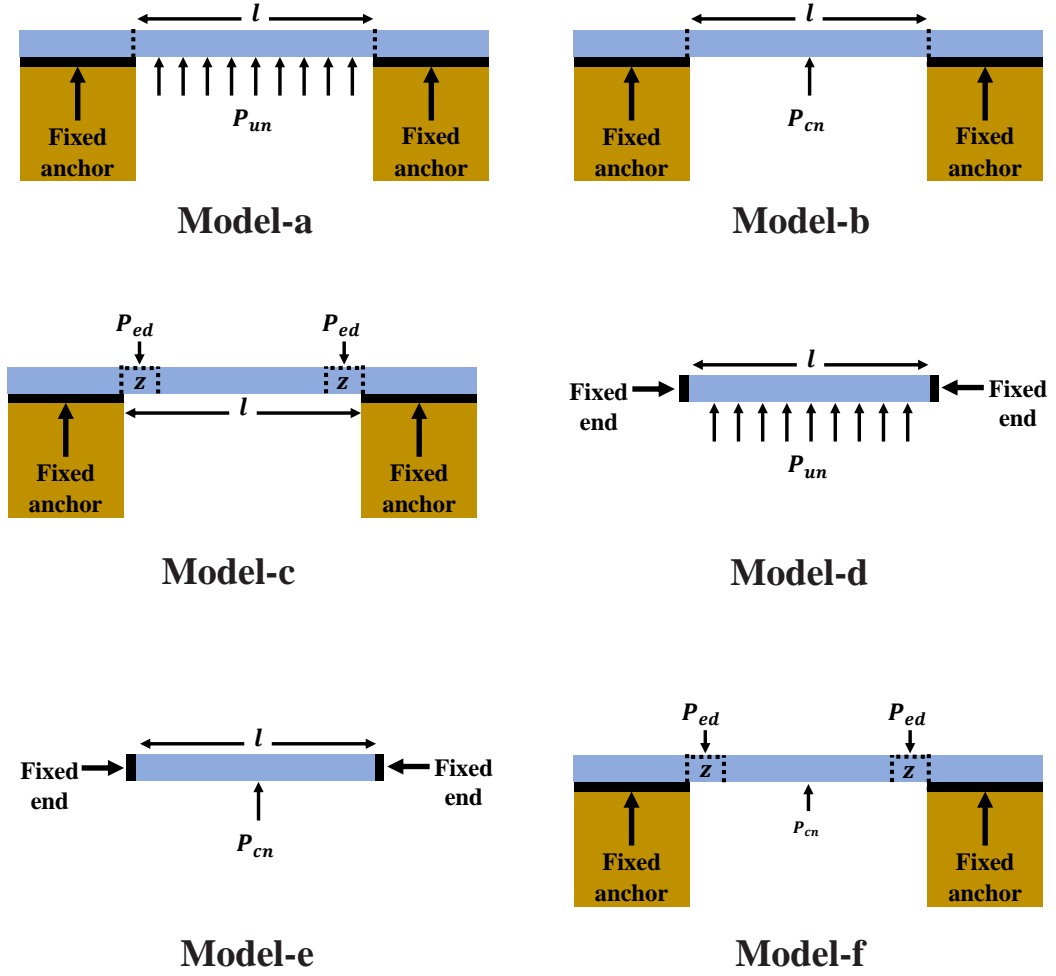


Figure 3.10: Finite element models of a fixed-fixed beam structure of tantalum with different boundary conditions. All models include a compressive stress (σ). **(Model-a)** Uniform load (P_{un}) applied along the beam length with two fixed anchors. **(Model-b)** concentrated load (P_{cn}) applied on the middle beam with two fixed anchors. **(Model-c)** Concentrated load applied (P_{ed}) along distance (z) from the fixed anchors. **(Model-d)** Uniform load (P_{un}) applied along the beam length with two fixed ends without anchors. **(Model-e)** Concentrated load (P_{cn}) applied on the middle beam with two fixed ends without anchors. **(Model-f)** Concentrated loads applied on the middle beam (P_{cn}) and along distance (z) from the fixed supported ends (P_{ed}). The boundary conditions of the developed models have been applied to provide the best empirical fit to the measurements.

In the case of **Model-c**, in addition to the -470 MPa of compressive residual stress, an external load of 0.12 MPa has been applied only on parts nearby the fixed clamped ends. The buckling profile of this model is entirely different with downward deflection. In **Model-f**, the application of the mechanical load both on the centre of the bottom of the beam and on the parts near the fixed ends of the beam, as well as applying compressive stress to the beam material, a deflection profile can fit the measurements. From [Figure 3.11](#), it can be seen that **Model-f** shows the least error and fits the measured profile closely.

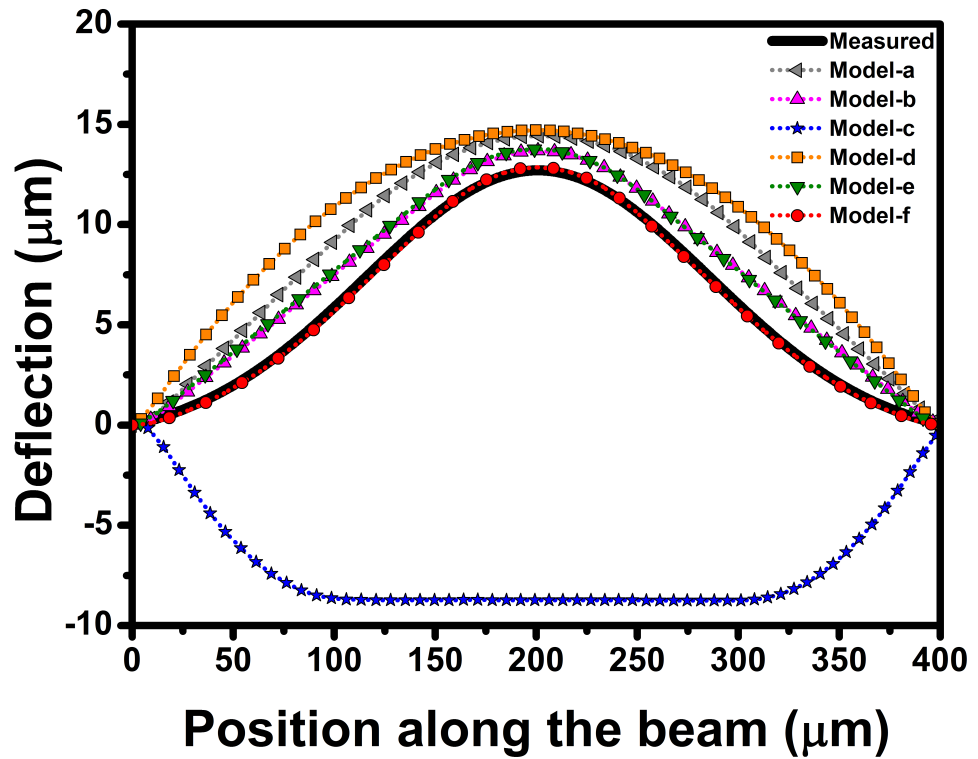


Figure 3.11: Comparison of final measured (solid line) and simulated (dotted line) deflection profiles of a $400\text{-}\mu\text{m}$ -long beam using six finite element models.

To verify the outcomes of **Model-f** for the experimentally observed deflection of other fabricated beams presented in [Table 3.3](#), different values of compressive stress and external loads have been applied. The verification simulation results are shown in [Table 3.5](#). It can be seen that the simulated deflection amplitude is similar to

the measured one for all beams. It is concluded, therefore, that the developed model (**Model-f**) can be used to predict precisely the mechanical deflection profile of doubly clamped beams structure.

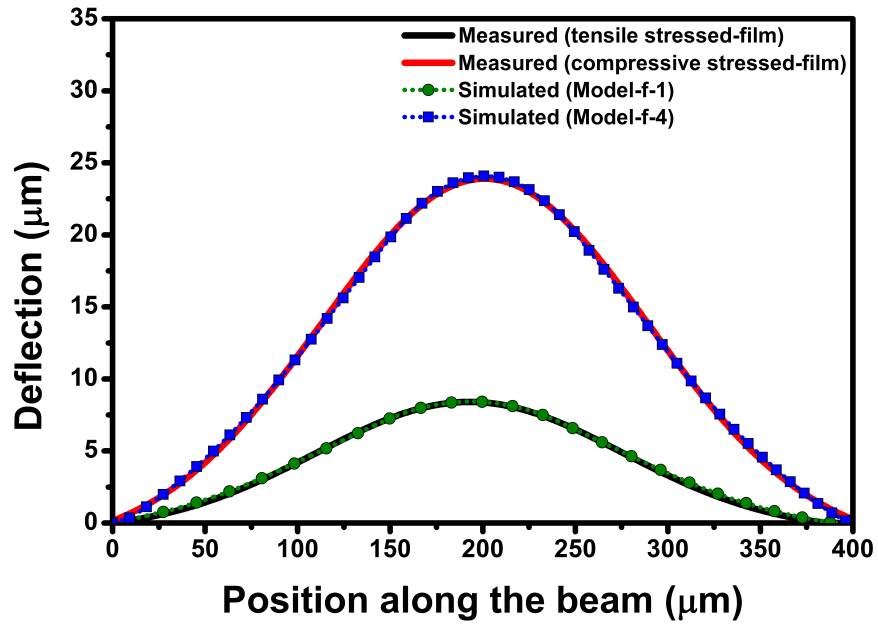
Table 3.5: Comparison of the maximum vertical deflection (A) of 400- μm -long beams simulated with **Model-f** using different values of compressive stress (σ) and external load (P_{cn} and P_{ed}) applied along the beam length.

Model	σ (MPa)	P_{cn} (MPa)	P_{ed} (MPa)	A^* (μm)	A^{**} (μm)
Model-f-1	-200	0.5	0.15	8.40	8.43
Model-f-2	-470	0.12	0.045	12.70	12.85
Model-f-3	-825	0.27	0.11	16.96	16.83
Model-f-4	-1675	0.55	0.15	23.90	24.09
Model-f-5	-1760	0.55	0.15	24.51	24.74

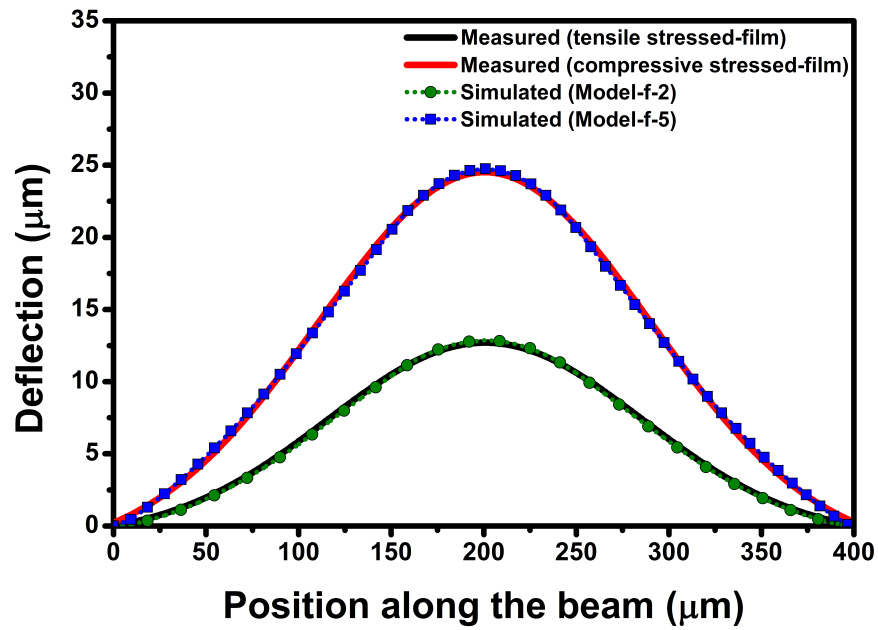
*Measured. **Simulated.

3.6.4 Effect of initial film stress

To investigate the influence of initial residual stress of the as-deposited films on the actual mechanical profile of the released microstructures, the final measured deflection profiles of doubly clamped beams made from tensile and compressive-stressed films and released by wet and dry etching processes are shown in [Figure 3.12](#). The measured deflection profile of the beams with length of 400 μm , width of 15 μm and thickness of 0.5 μm has been fitted with **Model-f** ([Table 3.5](#)). It can be seen that the beams made from compressive-stressed films (**Model-f-4** and **Model-f-5**) have exhibited larger deflection than the beams made from tensile-stressed films (**Model-f-1** and **Model-f-2**). The different deflection profile of the fabricated beams between the tensile and compressive-stressed films could be related to the film microstructure and the nature of the interface between the substrate and the deposited film during the fabrication process.



(a) Wet etch release



(b) Dry etch release

Figure 3.12: Comparison of final measured (solid lines) and simulated (dotted lines) deflection profiles of 400- μm -long beams made from tensile and compressive stressed-films and released in wet (a) and dry (b) etching systems. The simulated profiles are based on **Model-f**.

In the case of tensile stressed-films, contraction takes place and the surface may bend and render in a concave shape [110].

Therefore, the microbeam tends to remain flat after removing the sacrificial layer [111]. In the case of compressive stress, the film undergoes an expansion and the surface may render in a convex shape [110]. Consequently, the possibility of buckling or delaminating is high after removing the supporting layer during the release process [112]. Furthermore, it is likely that the tensile-stressed films possess ultra-small columnar grains with microvoids at the film/substrate interface, thereby inducing a small magnitude of residual stress in the released beam after removing the sacrificial layer underneath. The compressive-stressed films, on the contrary, might have tightly packed atoms with fibrous structures [92], and therefore have a much denser film/substrate interface that leads ultimately to a larger deflection after release. However, further investigation is required to verify the buckling behaviour that is due to the film/substrate interface.

3.6.5 Effect of etch release process

The mechanisms of the different etching approaches used to remove sacrificial layers and release the final structural components is of great importance in fabricating MEMS devices. To study the effect of etch release process on the mechanical static behaviour of suspended microbeams of tantalum, a comparison of the final deflection profile of tantalum beams released in wet and dry etching processes has been implemented.

Figure 3.13 shows the final measured and simulated deflection profiles of 400- μm -long beams made from tensile-stressed films and released by three different etching methods. The first etching system is wet-based etching using a solution of buffered hydrofluoric acid (BHF). In the second etching system, dry-based oxygen plasma etching (O_2 -ashing) at a temperature of 70 °C has been employed.

The last etching system is based on a dry downstream oxygen plasma using O₂-downstreaming at a temperature of 200 °C and flow rate of oxygen/nitrogen of 2000/100 sccm. The simulated profiles are based on **Model-f**.

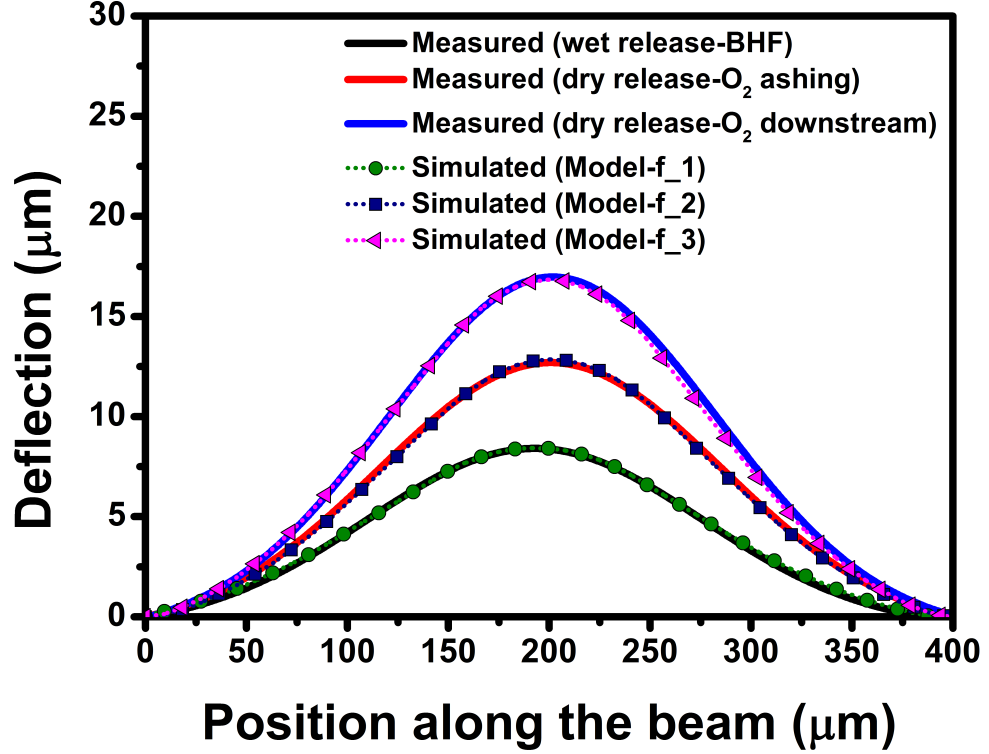


Figure 3.13: Comparison of final measured (solid lines) and simulated (dotted lines) deflection profiles of 400-μm-long beams made from tensile and compressive stressed-films and released in wet and dry etching systems.

A good agreement between simulation and experiment can be seen clearly in [Figure 3.13](#). It has been found that the beams that have been released in the dry etch release methods have exhibited larger deflection profiles than the beams released in the wet etch release technique. The results are in good agreement with previous studies [113, 114] that have reported the influence of sacrificial materials such as photoresist and silicon on the compressive residual stress of released beams.

In this thesis, however, new findings have shown that

using different etch release conditions (e.g. O_2 -ashing and O_2 -downstreaming) would cause different deformations in the final released microstructure even with the use of the same sacrificial material (e.g. polyimide in this study). Accordingly, the different observations of the buckled microbeams could only be explained in terms of etch release mechanism by taking into consideration the effect of etch release conditions. Temperature, for example, can be an influential parameter during the etch release process. Since the wet etch release has been performed at room temperature, further stress that may be introduced through high temperature processes can be avoided. In contrast, the higher temperatures in the dry etch processes (200 °C in the O_2 -downstreaming compared to 70 °C for O_2 -ashing) might have a considerable influence on the released structure.

Compared to the deflection profile observed here, Weileun Fang et al. [105] have shown that the shape and the direction of buckling can be controlled by focusing a dry NH_3 plasma treatment on central and sided regions of the microbeam. In fact, their findings support the model assumption (**Model-f**) of applying the mechanical load on the central and sided parts of the beam. Therefore, shapes and amplitudes of the buckling profile can be tuned by changing the position and magnitude of the applied load. Typically, these results reveal how the etch release process can play an important role in determining the final deflection profile of the fabricated device.

3.6.6 Effect of beam dimension

In [Chapter 2](#), it has been shown that the resonant frequency of clamped-clamped beams can be influenced by changing the beam dimensions. Here, the effect of dimensions parameters on the static deflection profile of suspended beams has been investigated. The

final measured and simulated buckling profiles along the position of doubly clamped beams with lengths ranging from 100 to 400 μm are shown in Figure 3.14. The simulated profiles have been obtained using **Model-f** based on the finite elements parameters provided in Table 3.6. The simulated buckling profiles of each beam are in good agreement with those obtained by experiment. Also, it is worth mentioning that the results of deflection profile as a function of the beam length in this work are in good agreement with other studies for other materials [100, 115].

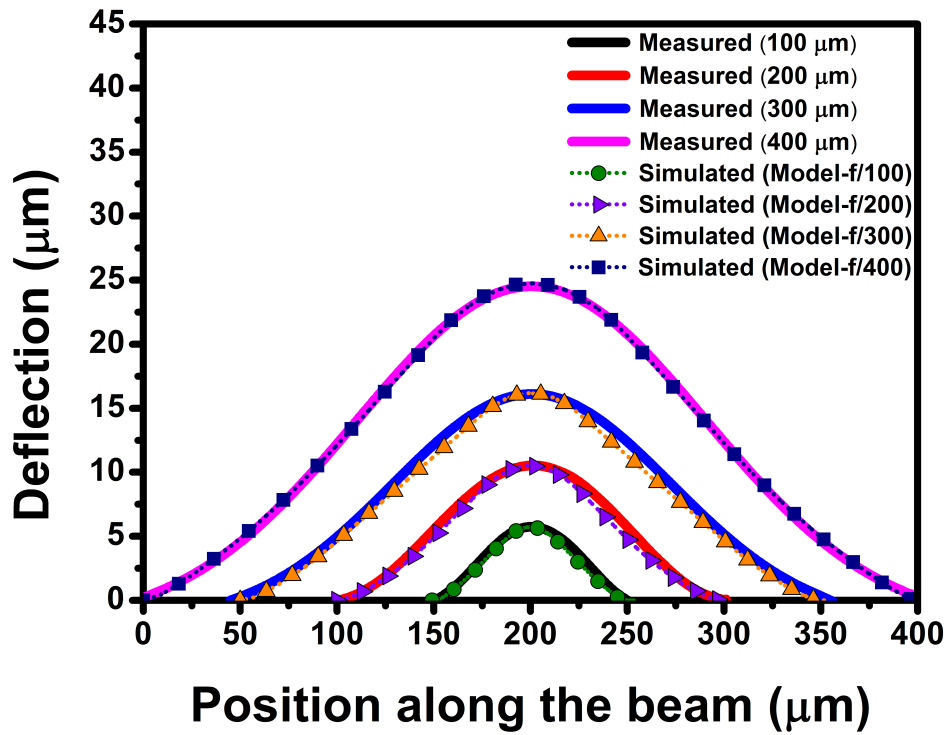
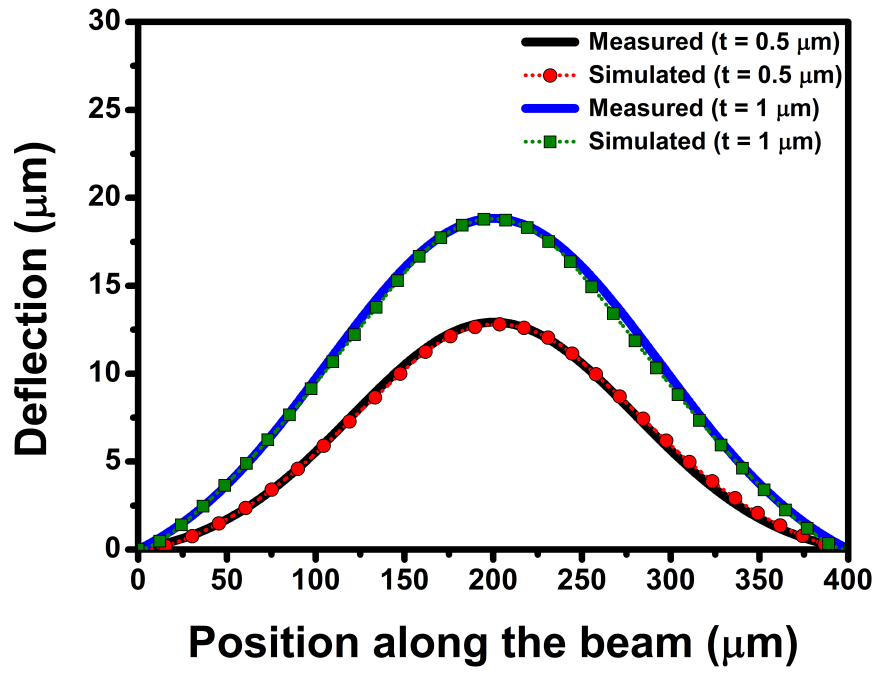


Figure 3.14: Comparison of final measured (solid lines) and simulated (dotted lines) deflection profiles of beams with lengths of 100, 200, 300 and 400 μm . The beams are made from compressive stressed-films and released in a dry etching process.

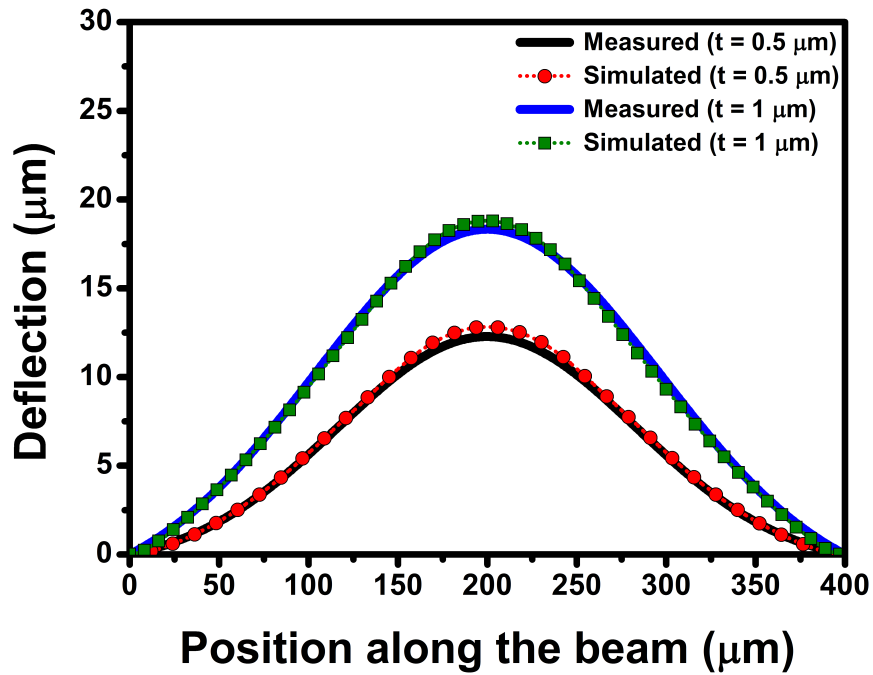
In general, we have found that the amplitude of buckling deflection increases with the increase of the beam length. Such observations could be attributed to the boundary conditions effects. For example, to fit the experiment, the simulations has shown that the 100- μm -long beam requires more compressive stress and

centred load than the 200 or 300- μm -long beams. In other studies, for example, the bending moment due to boundary configuration effects is believed to have an influential role in determining the beam deflection-length relationship [102]. In addition, the beam stiffness may decrease with the increase of the beam length [116], and thus longer beams tend to buckle more than shorter ones.

To examine the effect of beam width and thickness, a comparison of the final measured and simulated buckling profile of 400- μm -long beams with widths of 15 and 20 μm and thicknesses of 0.5 and 1 μm is shown Figure 3.15. The simulated profiles have been obtained using **Model-f** based on the finite elements parameters provided in Table 3.7. Note that the compressive stress values used in the simulation are similar to those obtained by experiment.



(a) Beam width = 15 mm



(b) Beam width = 20 mm

Figure 3.15: Comparison of final measured (solid lines) and simulated (dotted lines) deflection profiles of 400- μm -long beams with two different widths and thicknesses. (a) Beams of width of 15 μm and thicknesses of 0.5 and 1 μm . (b) Beams of width of 20 μm and thicknesses of 0.5 and 1 μm .

Table 3.6: Maximum simulated vertical deflection (A) of fixed-fixed beams with lengths of 100, 200, 300 and 400 μm . **Model-f** has been used with different values of compressive stress (σ) and external load (P_{cn} and P_{ed}) applied along the beam length.

Model	σ (MPa)	P_{cn} (MPa)	P_{ed} (MPa)	A^* (μm)	A^{**} (μm)
Model-f/100	-1425	2	0.4	5.66	5.74
Model-f/200	-1125	1.2	0.4	10.37	10.47
Model-f/300	-1260	1	0.4	16.15	16.17
Model-f/400	-1760	0.12	0.045	24.51	24.74

*Measured. **Simulated.

Table 3.7: Maximum simulated vertical deflection (A) of 400- μm -long beams with widths (w) of 15, and 20 μm and thicknesses (t) of 0.5, and 1 μm . **Model-f** has been used with different values of compressive stress (σ) and external load (P_{cn} and P_{ed}) applied along the beam length.

w (μm)	t (μm)	σ (MPa)	P_{cn} (MPa)	P_{ed} (MPa)	A^* (μm)	A^{**} (μm)
15	0.5	-453.5	0.13	0.05	12.70	12.83
15	1	-914.16	0.7	0.15	18.74	18.83
20	0.5	-453.5	0.13	0.05	12.72	12.83
20	1	-914.16	0.7	0.15	18.80	18.83

*Measured. **Simulated.

From [Figure 3.15](#), it can be seen that thicker microbeams tend to buckle more than thinner ones. For example, the vertical deflection has been found to be 18.78 μm for a 1- μm -thick beam compared to 12.92 μm for a 0.5- μm -thick beam. It is possible that the level of residual stress may vary through the film's thickness [117]. For beams with the same length and widths, the simulation results presented in [Table 3.7](#) have shown that the 1- μm -thick beams experience higher compressive residual stress and external loads than the 0.5- μm -thick beams. However, for beams with the same length and thickness but different widths, the deflection profile has been found to be almost independent of beam width. Despite the slight variations of the experimental vertical deflection between 15

and 20- μm -wide beams with the same length and thickness, the simulations have shown that the vertical deflection and buckling profile of these beams are identical.

3.7 Summary

This chapter has been devoted to the fabrication and characterisation of thin-films and suspended microstructures of tantalum. The accomplished work and findings of this chapter are summarised as follows:

The relationship of fabrication process-related parameters such as sputtering conditions, annealing treatment, oxygen exposure and bombardment exposure to the characteristics of residual stress of tantalum thin-films have been studied. The residual stress of nanofilms of tantalum has been found to shift between tension and compression state regions, depending on the deposition and post-deposition conditions.

Firstly, the residual stress of the as-deposited films has been investigated with respect to the sputtering power and pressure. The films' stress has been found to be more influenced by the sputtering pressure. The residual stress of the films starts as a compressive stress at low sputtering pressures and switches significantly to the tensile state as the pressure increases.

The residual stress of the as-deposited films has been studied while treating the films at different annealing temperatures. Annealing the thin-films at 300 °C leads to a considerable shift of the thin-films' stress towards the compression region. Noticeable changes of stress in the unannealed films that have been sputtered at higher sputtering pressure have been observed after exposing the films to atmospheric ambient, while the annealed films have shown a stability in their stress during exposure to the air. Furthermore, the

residual stress of tantalum thin-films has been modified by exposing the films to pure argon energy bombardment. When the power and flow rate of Ar energy increases, a high compressive stress has been found to develop in the film.

In the second part of this chapter, an array of suspended microbeams of tantalum based on clamped-clamped structures has been fabricated from compressive and tensile-stressed films and released in wet and dry etching systems. The mechanical static profile of the beams has been characterised optically. It has been found that the suspended beams made from tensile-stressed films have exhibited the least vertical deflection. Importantly, the wet etch release approach leads to induce smaller deformation in the final fabricated beams than the dry etch release methods. An optimum profile of the suspended microstructures of tantalum with an aspect ratio of 1:48 has been obtained from the tensile-stressed films that have been released by the wet etching method. A FEA model has been developed to fit the buckling behaviour of doubly clamped beams by including the effects of compressive residual stress and applying an external mechanical load at different boundary conditions.

Chapter 4

Dynamics of Tunable Tantalum-based Resonators

4.1 Introduction

This chapter is dedicated to the fabrication, characterisation and dynamic simulation and testing of an array of suspended ultra-long microstructures of tantalum beams. The outcomes of [Chapter 2](#) and [Chapter 3](#) will be considered to design properly ultra-long beams that can operate at frequencies within the audio range (20 Hz – 20 kHz). Then, the fabrication procedure and physical characterisation of free-standing ultra-long beams of tantalum in the form of doubly clamped structures will be described. The electrostatic actuation method will be used to drive the fabricated beams into resonance and tune their frequencies over a desired range. In addition, the dynamic behaviour of tantalum beams will be modelled analytically and numerically and compared with measurements.

4.2 Design of tantalum-based resonators

Electrostatically driven MEMS-based clamped-clamped beams have been applied extensively to realise a wide range of transducers for different sensing and actuation applications [118]. From a dynamic performance point of view, however, most of these transducers require high actuation power and operate in a relatively high frequency regime (up to MHz) as a means to avoid the pull-in instability that takes place when the drive voltage exceeds a certain limit at which the electrostatic force surpasses the elastic force [119]. When the pull-in occurs, the moveable structures will collapse on the actuation electrode. In this case, the resonator may undergo a large undesirable deformation that may lead to a functional failure and limit the applications of the device.

Low frequency operation is essential for particular applications such as audio sensors [120], microphones [121], energy harvesters [122], and accelerometers [123]. In this project, the main objective is to realise resonators that operate at audio frequency range, so that these resonators can be employed in acoustic transducers such as artificial basilar membranes and other hearing aid devices.

To achieve a proper design of clamped-clamped microbeams that resonate at audio frequencies, it is necessary to increase the length or reduce the thickness of the beams. However, the fabrication process for making long suspended beams is extremely challenging. Even for short beams (i.e. length below 500 μm), the effect of stress induced during the deposition and post-fabrication processes can cause the structure to buckle or bend undesirably [102]. In order to realise straight and long suspended beams, the process-induced stress should be controlled, and the aspect ratio of static vertical deflection to beam length needs to be minimised. In the previous

chapter, the influence of stress, due to deposition and fabrication processes, on tantalum-based films and suspended beams has been investigated and optimised.

In this chapter, the design, fabrication and characterisation of an array of electrostatically driven clamped-clamped tantalum microbeams that have a width of 40 μm and a thickness of 1 μm will be presented. Although relatively thin beams (i.e. thinner than 1 μm) is preferable for low frequency applications, the realisation of thin and long beams is undoubtedly difficult. From fabrication point of view, reducing the thickness of a beam structure while increasing its length would make the beam more susceptible to damage. One of the novelties of the current device lies in its design that includes ultralong-microbeams with lengths ranging from 1 to 3.4 mm. The large aspect ratio (i.e. length to thickness) is the key component of achieving low frequency and high sensitivity of the fabricated structures. Also, the design of the resonator includes a large bottom actuation electrode that could provide efficient actuation by reducing the driving voltage, and hence minimising the pull-in instability. Moreover, the fabrication process has been further optimised to enable a successful realisation of fully suspended microbeams without producing mechanical deformation such as bending or buckling.

4.3 Fabrication of ultralong-beams of tantalum

A surface micromachining process has been used to fabricate an array of clamped-clamped microbeams of tantalum. The fabrication process flow for the beams is shown in [Figure 4.1](#). The fabrication process begins with the deposition of ~ 240 nm of plasma-enhanced chemical vapour deposition (PECVD) silicon oxide (SiO_2) on a

p-type (100) silicon wafer. To define the actuation electrode, a lift-off process has been used. First, a photoresist has been spin coated and patterned on an oxidised silicon wafer (Figure 4.1a). Afterwards, a 0.5- μm -thick layer of aluminium metal has been deposited using a DC magnetron sputtering system. Then, the photoresist has been stripped away leaving behind an actuation electrode (Figure 4.1b).

For the sacrificial layer, polyimide of thickness of 5.5 μm has been used. After coating, the polyimide has been baked initially at 90 °C for 90 s and 150 °C for a further 90 s. Then, the polyimide has been cured fully at 200 °C for 30 minutes. Chemical mechanical polishing (CMP) has been employed to planarise the sacrificial layer on the actuation electrode area (Figure 4.1c). To define the fixed-fixed microbeams, a photoresist has been spin coated and patterned (Figure 4.1d). Then, a DC magnetron sputtering system has been used to deposit four layers of tantalum metal using sputtering power of 500 W and sputtering pressure of 20 mTorr, 10 mTorr, 20 mTorr and 10 mTorr consecutively to form one layer of tantalum of 1 μm thickness. As confirmed by curvature measurements, the corresponding stress of the deposited tantalum layers will be compressive, tensile, compressive and tensile [124, 125]. In this case, the final residual stress in the whole deposited layer can be compensated by the influence of the compressive and tensile stress component of the different layers. The reason behind depositing four layer of tantalum film with two different deposition parameters is that, in addition to the compensation of stress components, the deposition rate at sputtering pressure of 20 mTorr is higher than that of 10 mTorr. After films deposition, the photoresist has been stripped away and the final structures of clamped-clamped microbeams has been defined (Figure 4.1e).

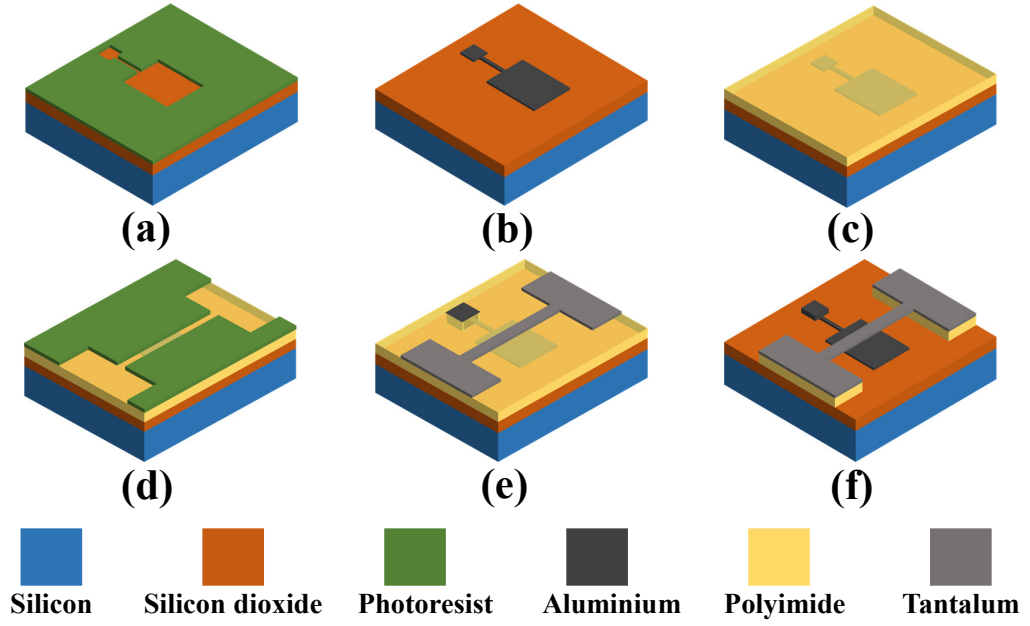


Figure 4.1: Schematic process flow for an array of fixed-fixed microbeams of tantalum. (a) Photoresist spin coated and patterned. (b) Actuation electrode of aluminium deposited and patterned with lift-off. (c) Polyimide spin coated and planarised by chemical mechanical polishing (CMP). (d) Photoresist spin coated and patterned in clamped-clamped structures. (e) Tantalum metal sputtered, and photoresist stripped. (f) Polyimide etched, and microbeams released.

The final step of the fabrication process is to etch the sacrificial layer using oxygen plasma-ashing, and thus the final microstructures have been released fully (Figure 4.1f). Consequently, an array of suspended fixed-fixed beams of tantalum with a thickness of $1\ \mu\text{m}$, width of $40\ \mu\text{m}$ and lengths ranging from $1\ \text{mm}$ to $3.4\ \text{mm}$ has been fabricated successfully.

4.4 Characterisation of fabricated structures

In a similar way to the characterisation of beams presented in Chapter 3, the suspension of the fabricated beam devices has been inspected. A physical characterisation by a scanning electron microscope (SEM) has been carried out to examine whether the structures have been released completely. Figure 4.2 shows SEM

images of an array of the released clamped-clamped microbeams after removing the sacrificial layer. No upward or downward deflection has been observed and it can be seen that the beams are fully released and showing a relatively straight profile along the length.

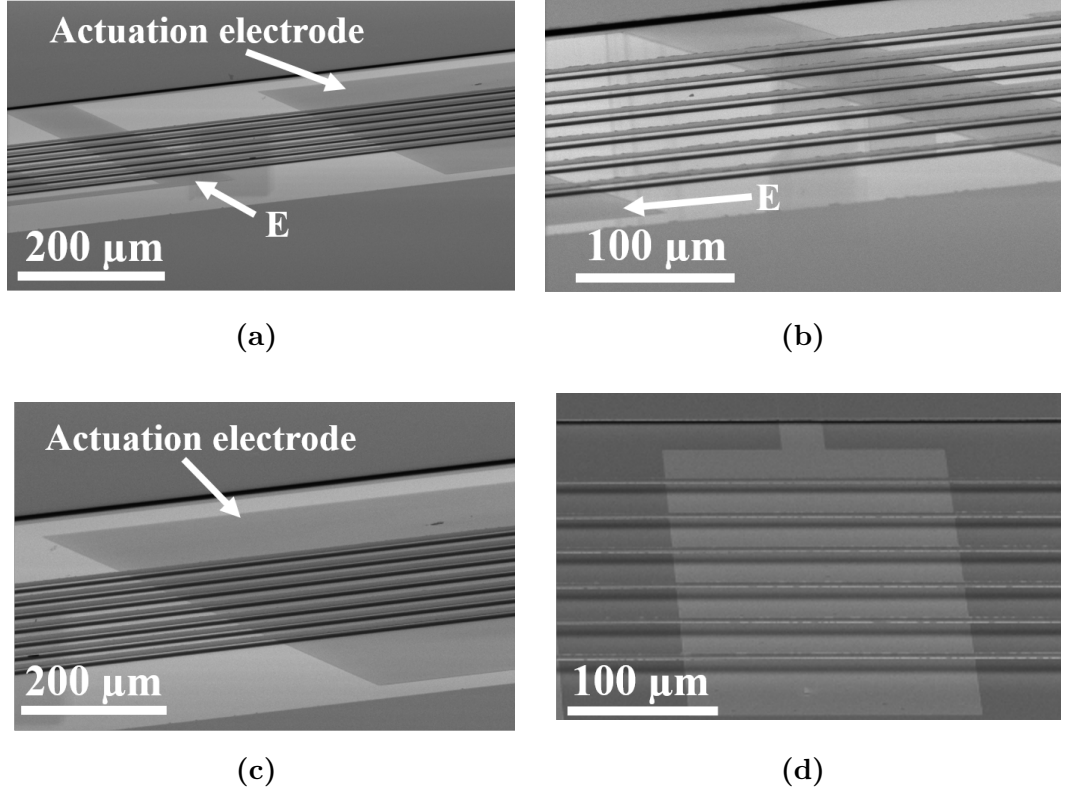


Figure 4.2: SEM images of the released microbeams after removing the sacrificial layer. (a) Image of long beams suspended over actuation electrode with zoom-in views in (b), (c) and (d). Image in (d) shows the actuation electrodes underneath the suspended beam. The shaded area marked with the letter E in (a) and (b) is an extra electrode for another experiment.

The suspension of released microstructures has been confirmed by a white light interferometer (WLI) that can provide a precise measurement of the final deflection profile of the fabricated devices. A typical WLI measurement of released microbeams suspended over a trench, 5.5-μm from the underlying substrate, is shown in Figure 4.3. The actual profile of the 3.4-mm-long beam is illustrated on the left side of the graph. The interferometry image shows a

consistent straight profile and the aspect ratio of vertical deflection to the beam length is $\sim 1:3400$. The slight deviations shown in the beam profile (black line) could be related to defects of the fabricated beams or an error of the optical interferometry measurement.

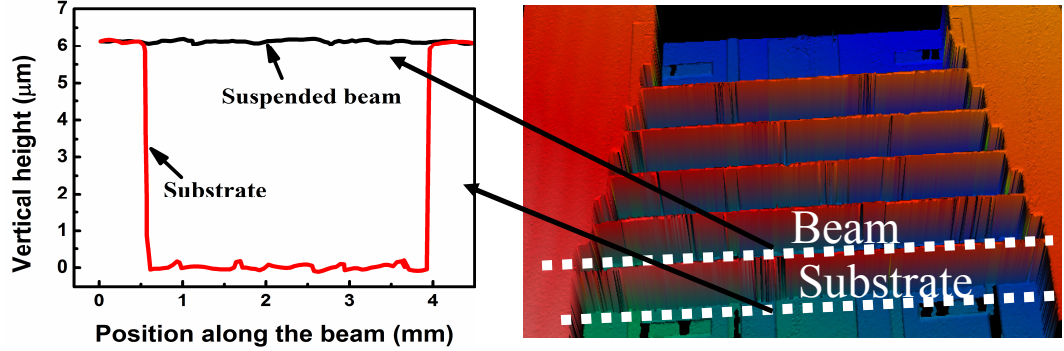


Figure 4.3: White-light interferometry measurement of the released microbeams after removing the sacrificial layer. The right side of graph shows reconstructed 3D interferometry of an array of released beams, while the left side shows the actual final deflection profile of a 3.4-mm-long beam suspended over a trench, 5.5-μm from the underlying substrate.

4.5 Mechanical dynamics of fabricated beams

To investigate the dynamic behaviour of the fabricated microbeams, electrostatic actuation has been implemented. The fabricated microbeams have been driven into resonance electrostatically by inducing an electrostatic field between the suspended beam plate and actuation electrode. For such measurements, a combination of an AC harmonic signal with an amplitude of V_{ac} superimposed to a DC voltage of V_{dc} has been applied between the resonator beam and the actuation electrode underneath. The vibration of resonators has been detected optically through laser Doppler vibrometry (LDV). In the measurements, a Polytec MSA-050 Micro System Analyser has been used. Note that the resonator devices have been tested at atmospheric pressure and room temperature conditions.

To find the operating frequency range of the resonators, a sweeping excitation signal has been applied across different audio

ranges (20 Hz – 20 kHz). For example, when an excitation signal is swept from 1 Hz to 8 kHz with a sampling time of 640 ms while applying a discrete Fourier transform (FFT) to the signal, the first four resonant frequencies have been observed. Another dynamic characteristic to measure is the vibration amplitude of the resonators by applying a sinusoidal signal at the resonant frequency modes.

4.5.1 Resonant frequency of tantalum beams

To measure the first four resonant frequencies of the fabricated suspended beams of tantalum, a combined actuation voltage of 0.5 V of V_{ac} and 3 V of V_{dc} has been applied while sweeping the frequency from 1 Hz to 8 kHz. Figure 4.4 shows the mechanical dynamic measurements of the first four modal frequencies of microbeams with lengths varying from 1 to 3.4 mm.

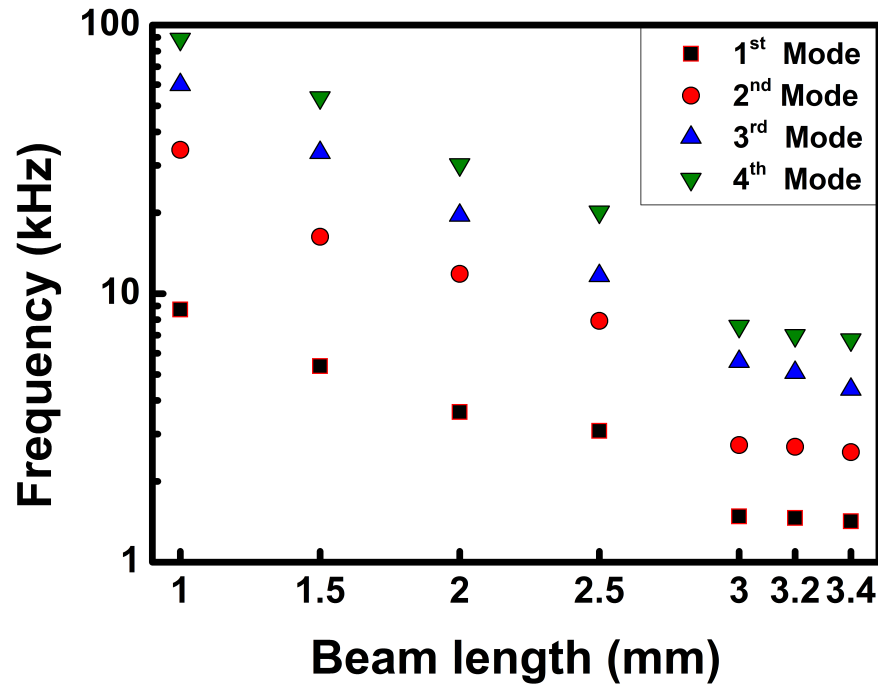


Figure 4.4: Frequency response measurements of the first four resonant frequencies with respect to the beam length.

For the amplitude of vibration measurements, a time domain sinusoidal signal has been applied at each resonant frequency. [Figure 4.5](#) shows, for example, the spectra of the first four resonant frequencies (i.e. the vibration amplitude with respect to the resonant frequency) for a 3-mm-long beam.

It has been observed that the frequency decreases and the amplitude of vibration increases when the beam length increases. For example, the longest beam (3.4 mm) has exhibited the lowest fundamental resonant frequency of ~ 1.4 kHz accompanied with a vibration amplitude of ~ 750 nm. Overall, the longest beam possesses the lowest frequency and the highest amplitude. For all fabricated resonators, the fundamental resonant frequency has been observed to be smaller than 10 kHz. Therefore, it is possible for the devices demonstrated here, even for 1-mm-long beams, to operate at frequencies within the audio range. This has been achieved by a proper design of ultra-long microbeams and the optimisation of the fabrication process.

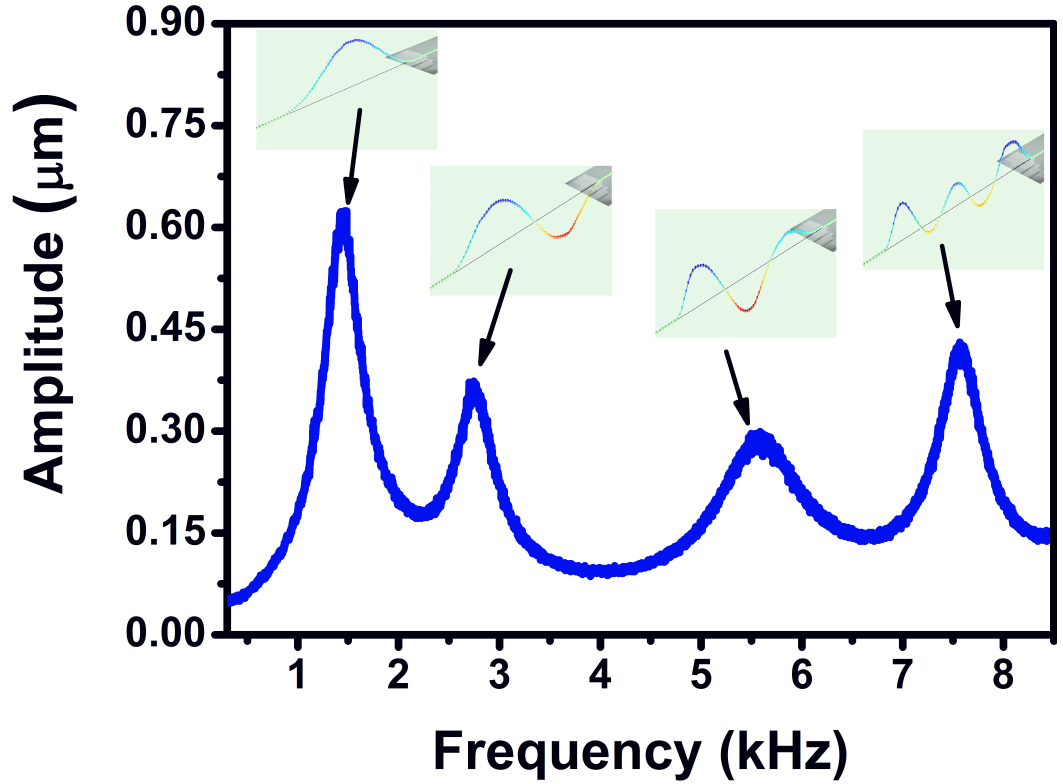


Figure 4.5: Frequency spectra of the first four resonant peaks of a 3-mm-long beam. The inset shows the corresponding shape of the measured modes.

4.5.2 Resonant frequency of stressed-beam resonators

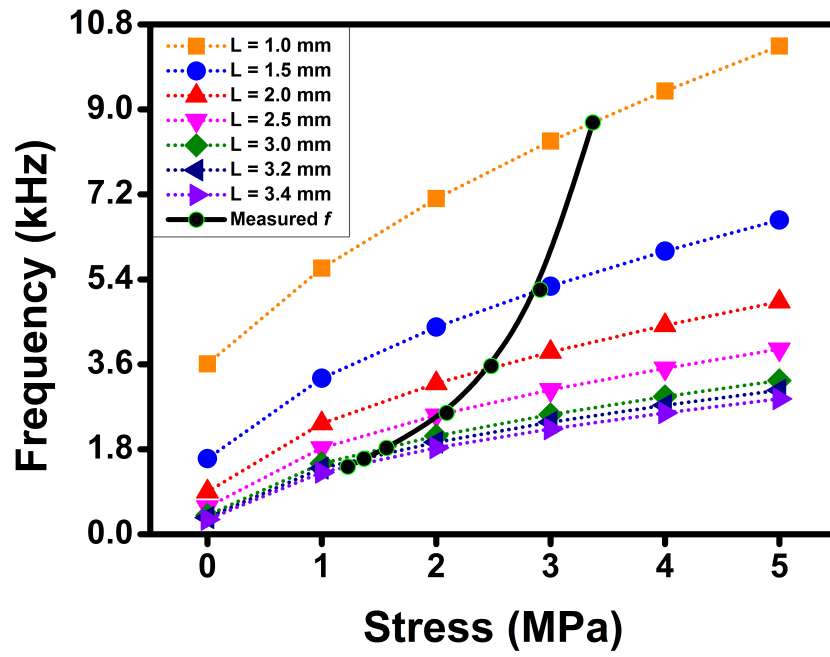
The presence of residual stress in a suspended beam material could affect the dynamic vibration behaviour of the fabricated resonator. Although the fabricated microbeams show a straight mechanical profile in terms of vertical deflection along the length, the residual stress that might be introduced into the resonators during the deposition and fabrication processes cannot be prevented completely. It is, therefore, important to determine whether the beams are experiencing a tensile or compressive stress and estimate the magnitude of the residual stress. In order to do this, numerical finite element analysis (FEA) and analytical models have been created to estimate the resonant frequencies and compare with the measurements.

For the analytical model, it has been assumed first that the fixed-fixed beams are stress-free ($\sigma = 0$), so that the fundamental frequency is given by [43]:

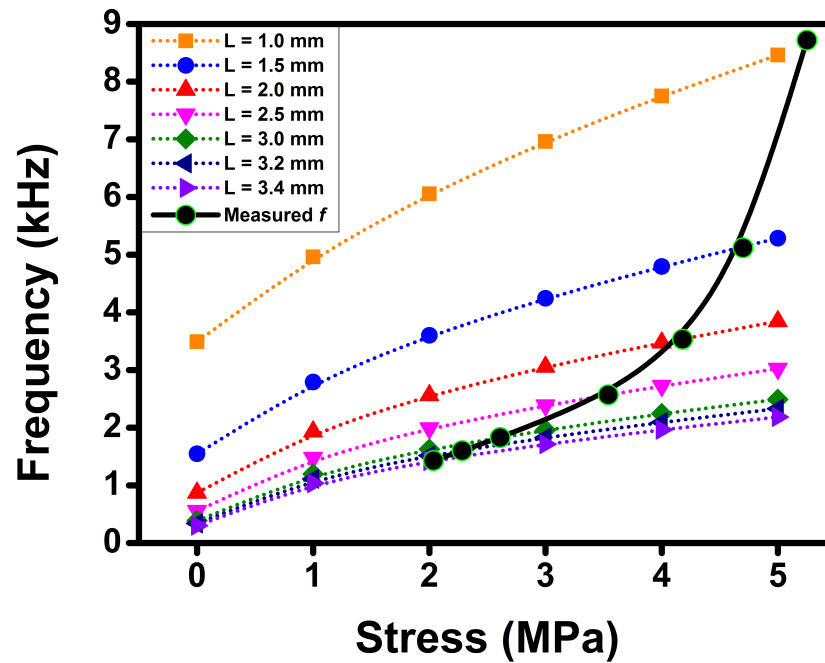
$$f_1 = \frac{4.730^2}{2\pi} \sqrt{\frac{EI}{\rho A l^4}} \quad (4.1)$$

where E is the Young's modulus, I is the moment of inertia ($I = bt^3/12$), ρ is the density, A is the cross-section area ($A = bt$) of the clamped-clamped beam of length l , width b and thickness t .

For the numerical simulation, the software package CoventorWare has been used. The material properties and dimensions of tantalum beams used in the present analytical and numerical models are Young's modulus of 186 GPa, density of 16.5 g/cm³, width of 40 μm and thickness of 1 μm . Therefore, the resonant frequency of tantalum beams has been estimated analytically and numerically, and compared with measurements, as shown in Figure 4.6. The measured and simulated first three shapes of the resonant modes are shown in Figure 4.7. With application of stress of 0 MPa, it can be seen that the fundamental resonant frequency that has been estimated from both analytical and FEA models (dotted line) is lower than the measured one (black solid line). This indicates that the beams are most likely experiencing a tensile stress. The presence of tensile stress in the suspended beam will stiffen the structure and hence increase the resonant frequency [126]. To estimate the magnitude of the tensile stress developed in the beams, additional analytical and FEA models have been created.



(a) Analytical



(b) FEA simulation

Figure 4.6: Measured and modelled fundamental resonant frequency as a function of stress for different lengths of tantalum fixed-fixed beams. Analytical (a) and simulation (b) models have been created using different values of stress (0–5 MPa) and lengths of 1 - 3.4 mm.

By assuming that the resonator beams are subjected to an

axial tensile force, the fundamental resonant frequency of a tensile-stressed clamped-clamped microbeam can be approximated analytically as follows [127]:

$$f_1 = 1.028 \frac{t}{L^2} \sqrt{\frac{E}{\rho}} \cdot \sqrt{1 + 0.295 \frac{l^2 \sigma_t}{Et^2}} \quad (4.2)$$

where σ_t is the biaxial residual tensile stress of the beam. Due to the straight profile of the final fabricated beams, it is proposed to apply a small magnitude of tensile stress (1 – 5 MPa) in Equation (4.2) in order to fit the experimental data. The same parameters in Equation (4.1) have been applied to the numerical and analytical models to find the fundamental resonant frequency, the values of which has been compared with the measurements. For the numerical FEA model, the same parameters of the analytical model have been applied and the fundamental resonant frequency has been simulated and compared with the measurements. As shown in Figure 4.6, the increase of tensile stress from 1 to 5 MPa, both analytical and FEA models show fairly good agreement with the results of resonant frequency obtained from the measurements.

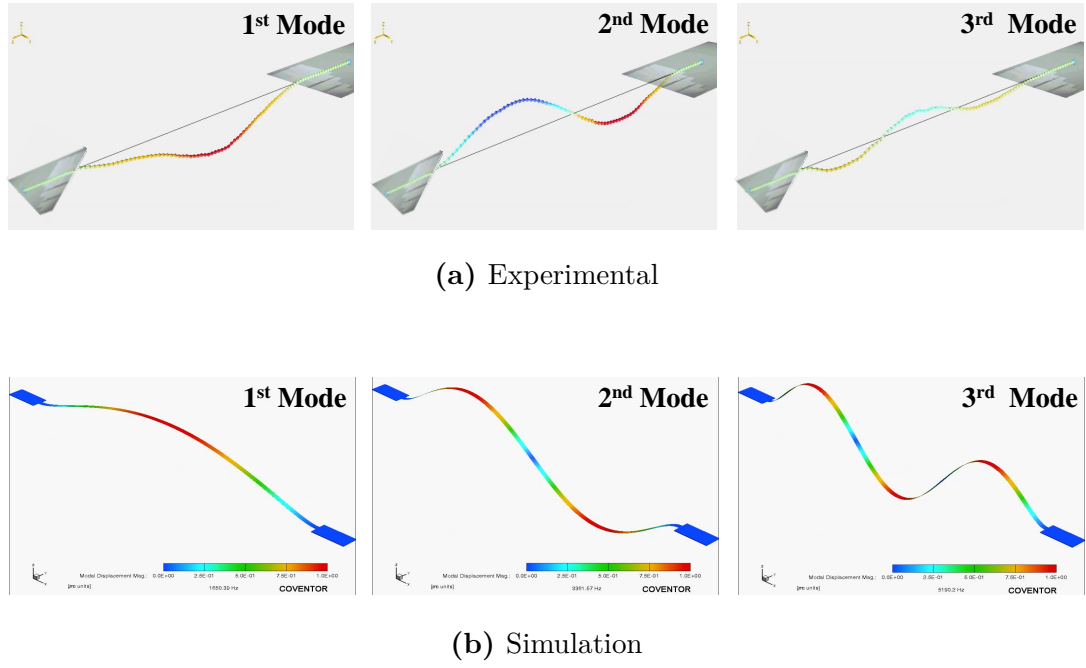


Figure 4.7: The first three shape of the resonant modes for clamped-clamped beam structures. (a) Measured by LDV (b) Simulated by CoventorWare.

For the microbeams of length of 1 – 2.5 mm, the measured resonant frequencies fit with the modelled ones with a tensile stress of 3 MPa for the analytical model and 5 MPa for the FEA model. However, for the beams of length of 3 – 3.4 mm, the estimated frequencies fit the experimental ones with a tensile stress of 1 – 2 MPa. Therefore, the tensile residual stress developed in the fabricated fixed-fixed microbeams is estimated to be about 2 – 5 MPa, supporting the SEM and optical interferometry measurements that show a consistent straight profile of the beams and confirming that the induced tensile stress is relatively small.

4.5.3 Pull-in voltage analysis

In general, the electrostatic actuation of MEMS microstructures experiences a highly nonlinear electromechanical coupling that may lead to pull-in instability [118]. The frequency of a resonant beam is sensitive to the induced electrostatic forces during the actuation.

To avoid a functional failure or undesirable collapse of the device, it is crucial to determine the pull-in voltage (V_{PI}) prior to performing an electrostatic actuation under high driving voltages. To describe the pull-in voltage of a clamped-clamped beam structure, a simple model, developed by Nathanson et al.[12], can be used as follows:

$$V_{PI} = \sqrt{\frac{8K_{eff}d_0^3}{27 \varepsilon_0 A_{eff}}} \quad (4.3)$$

where K_{eff} is the linear spring constant, d_0 is the initial zero-voltage gap between the suspended beam and the actuation electrode, ε_0 is the permittivity of free space and A_{eff} is the electrostatic effective area.

From Nathanson's model, Pamidighantam et al [128] developed a model that can describe the pull-in voltage of electrostatically driven beams accurately by including the effects of the axial stress and non-linear stiffening. Therefore, the pull-in voltage of a clamped-clamped beam of length l , width w and thickness t can be expressed as:

$$V_{PI} = \sqrt{\frac{8K_{eff}d_0^3}{20.9 \varepsilon_0 l w_{eff}}} \quad (4.4)$$

where the effective spring constant (K_{eff}), the effective Young's modulus (\hat{E}), the effective width (w_{eff}), and the tension axial force

(N) are given respectively as follows:

$$K_{eff} = \frac{32\hat{E}wt^3}{l^3} + \frac{8.32N}{l} \quad (4.5)$$

$$\hat{E} = E(1 - \nu^2), \text{ for } w > 5t \quad (4.6)$$

$$w_{eff} = w \left(1 + \frac{0.65(1 - \beta)d_0}{w} \right), \beta = 0.4 \quad (4.7)$$

$$N = wt(\hat{\sigma}_0 + \sigma_{NL}) \quad (4.8)$$

where $\hat{\sigma}_0 = \sigma_0(1 - \nu^2)$ is the residual film stress and $\sigma_{NL} = E\pi^2(\beta d_0)^2/4l^2$ is the induced axial stress due to the non-linear stretching.

By rearrange equations 4.4, 4.5 and 4.8, V_{PI} can be written as:

$$V_{PI} = \sqrt{\frac{d_0^3 wt}{l^2 \varepsilon_0 w_{eff}} \left(12.24 \frac{\hat{E}t^2}{l^2} + 3.18(\hat{\sigma}_0 + \sigma_{NL}) \right)} \quad (4.9)$$

In the case of $N = wt(\hat{\sigma}_0 + \sigma_{NL})$, the pull-in voltage for microbeams with a length ranging from 1 to 3.4 mm, width of 40 μm and thickness of 1 μm has been calculated using Equation (4.4) and plotted in Figure 4.8a and Figure 4.9a. It has been found that the pull-in voltage increases with the increase of the axial tensile stress and decreases dramatically as the beam length increases. For example, the pull-in voltage of 3.4-mm-long beams has been found to shift from 1.13 to 4.55 V as the applied tensile stress increases from 0 to 6 MPa. In general, the analytical calculations show that the pull-in voltage is inversely proportional to the beam length and directly proportional to the tensile stress.

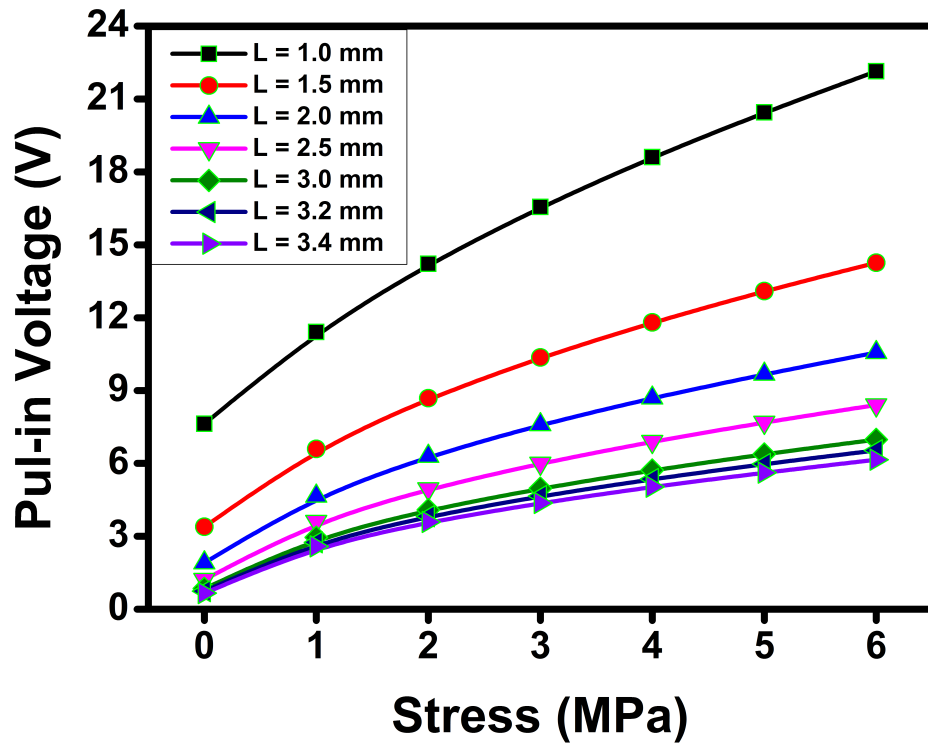
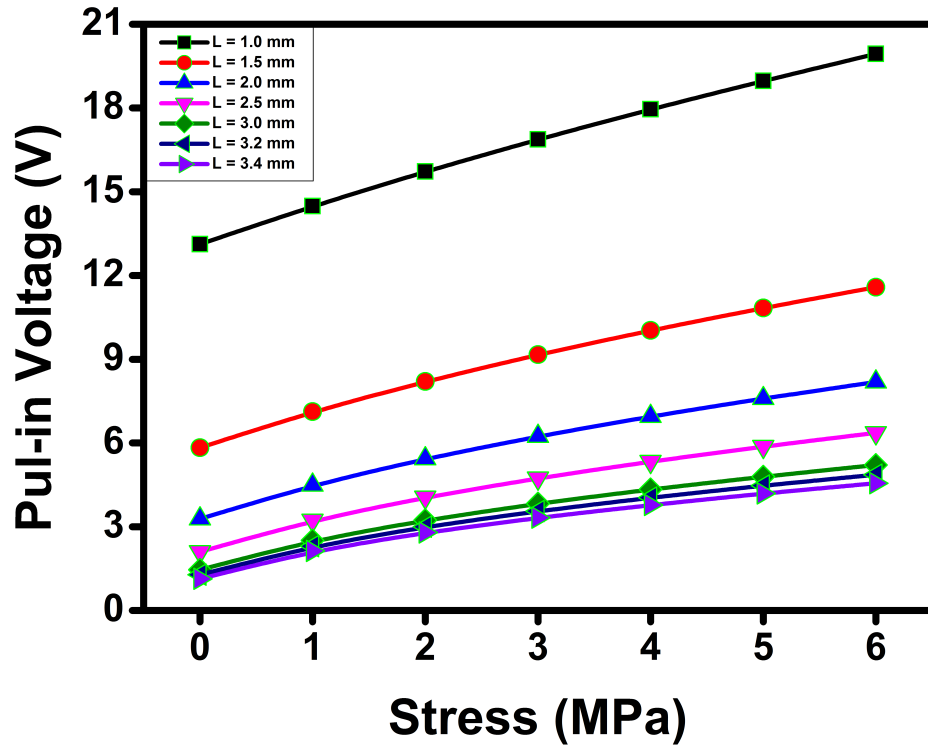
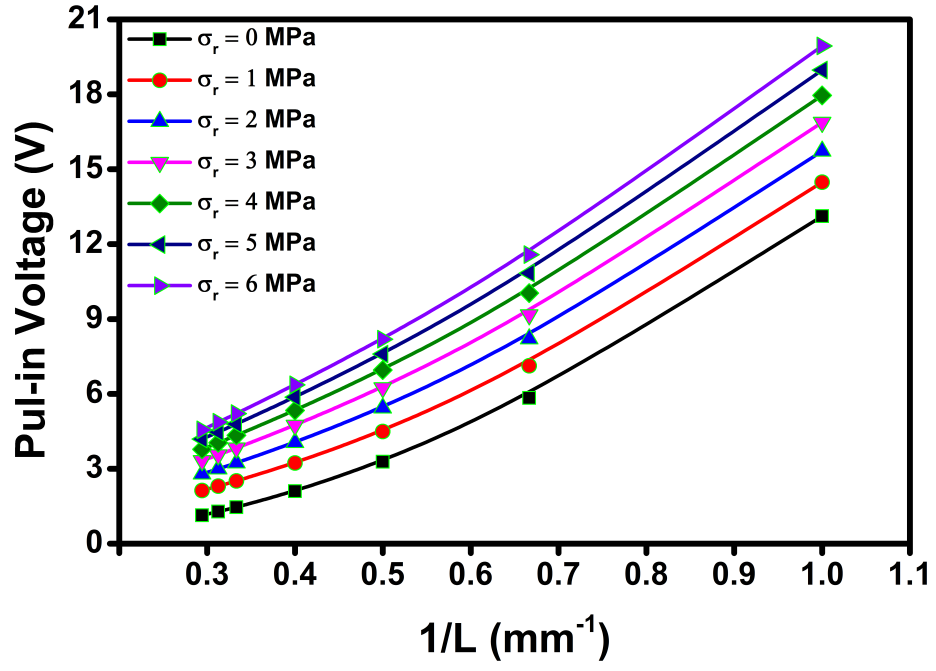
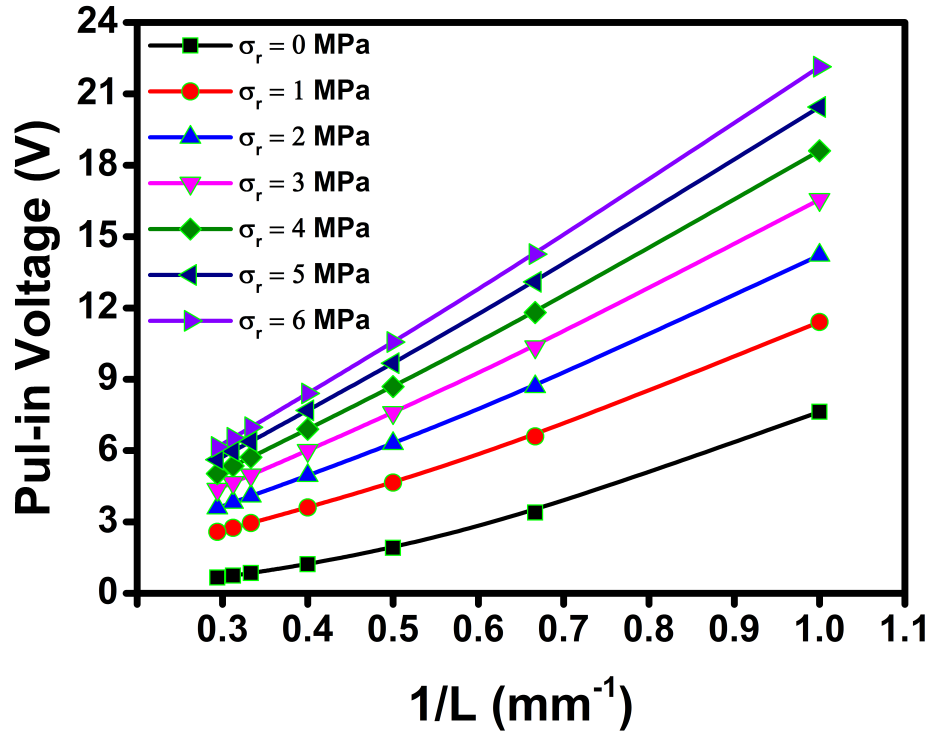


Figure 4.8: Pull-in voltage as a function of stress for different lengths of doubly clamped beams of tantalum. (a) The axial tensile force $N = wt(\hat{\sigma}_0 + \sigma_{NL})$. (b) The axial tensile force $N = wt\hat{\sigma}_0$.



(a)



(b)

Figure 4.9: Pull-in voltage as a function of microbeam length for different values of axial tensile stress. (a) The axial tensile force $N = wt(\hat{\sigma}_0 + \sigma_{NL})$. (b) The axial tensile force $N = wt\hat{\sigma}_0$.

However, it has been found experimentally that the fabricated microbeams can be actuated electrostatically with driving voltages higher than 4.5 V. Therefore, it is assumed that the beams experience a small non-linear stretching, and thus the corresponding axial stress (σ_{NL}) can be ignored. The axial tensile force becomes $N = wt\hat{\sigma}_0$, and the pull-in voltage has been estimated using Equation (4.4) and plotted in Figure 4.8b and Figure 4.9b. It can be seen a similar behaviour to the first case (Figure 4.8a), where the pull-in voltage decreases with the increase of the beam length and increases as the axial tensile stress increases. Despite the similarity, the estimated pull-in voltage in the second case is slightly higher than that in the first case. For example, the longest beam (3.4 mm) has shown a pull-in voltage of 6.1 V at an axial tensile stress of 6 MPa. Compared with the experimental observations, the second model has been found to be more accurate in predicting the pull-in voltage of fixed-fixed structures of tantalum microbeams.

4.5.4 Frequency tuning: experimental measurements

The resonant frequency of electrostatically-driven doubly clamped beams can be tuned by altering the mechanical stiffness of the suspended beams. Typically, this can be achieved by changing the DC voltage between the suspended beam and the actuation electrode. In some cases, depending on the driving voltage and design characteristics, nonlinear phenomena such as spring softening and spring hardening can be induced. In spring softening, as the oscillation amplitude increases, the effective spring constant decreases and that results in a downward shift in the resonance frequency. In the case of spring hardening, the resonant frequency increases as the effective spring constant increases [129, 130].

To examine the dynamic vibration tuning feature of fixed-fixed microbeams of tantalum, different DC bias voltages of 1 – 5 V

have been applied to a beam of length 3.4 mm and its frequency response at each applied voltage has been measured with an LDV. The frequency spectra measurements in response to the applied DC voltage is shown in Figure 4.10. It has been observed that increasing the V_{dc} tuning voltage from 1 to 5 V has induced a spring softening effect in the fabricated beam. That is, the resonant frequencies shift downwards with the increase of the V_{dc} tuning voltage.

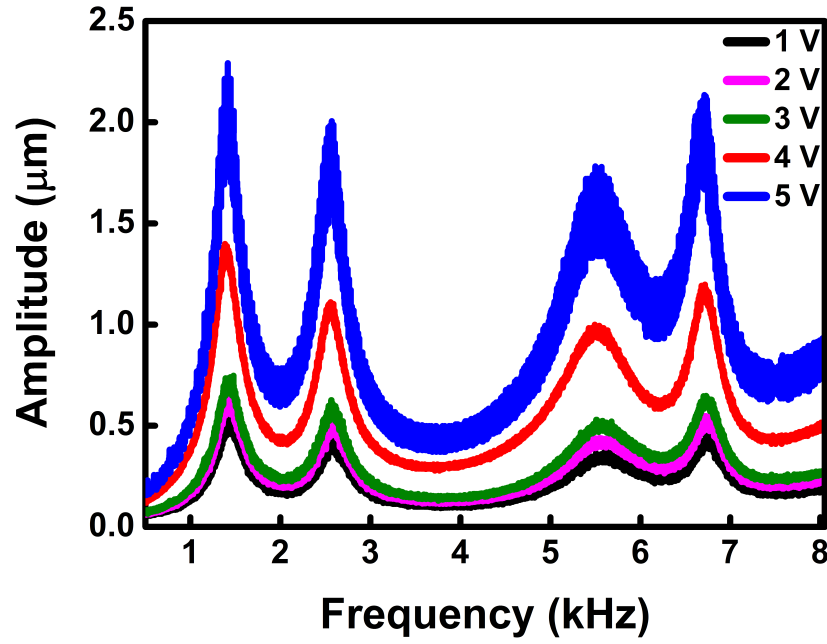
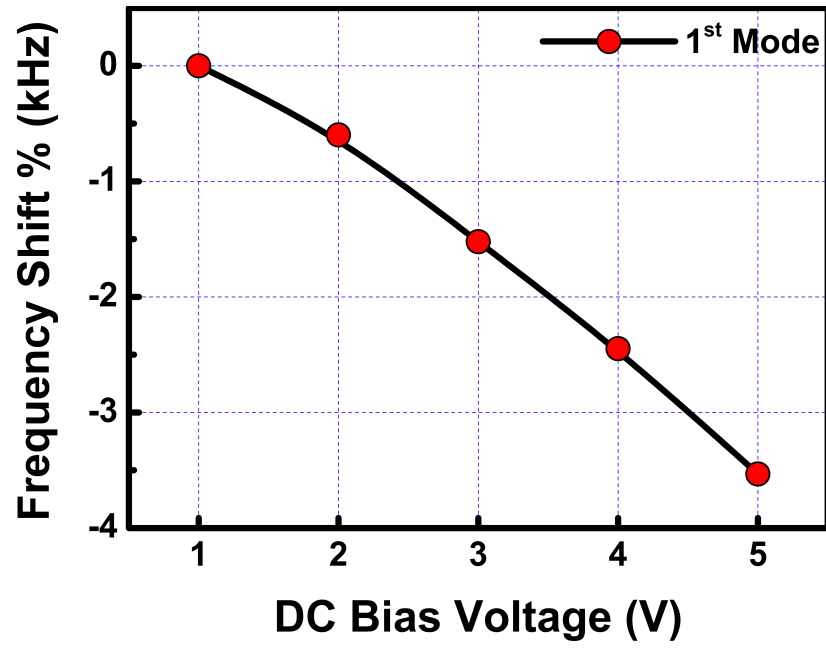


Figure 4.10: Measured frequency response of a 3.4-mm-long microbeam to different V_{dc} tuning voltages of 1 - 5 V and V_{ac} of 0.5 V.

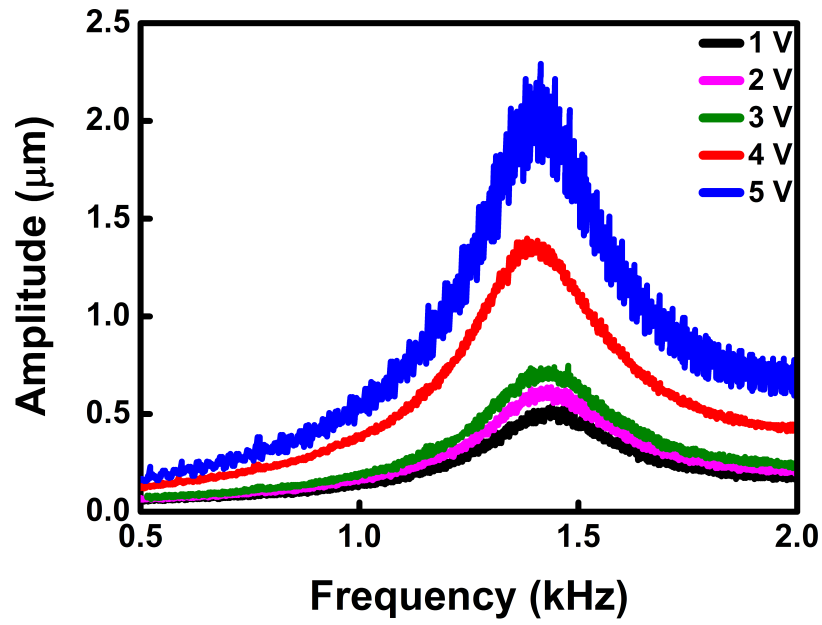
The observed downward shift of the fundamental resonant frequency of the beam of length of 3.4 mm is shown in Figure 4.11a. For instance, it has been found that the increase of the DC tuning voltage from 1 to 5 V leads to a downward shift of the first modal frequency of -35000 ppm. Note that the beams have been actuated with a small DC voltage (i.e. < 5 V) in order to avoid pull-in instability and its related failure. Exciting the suspended beams with a higher DC voltage offset (i.e. > 5 V) could introduce non-linearity, and this might explain the noise seen in the frequency

spectrum at a tuning voltage of 5 V.

In addition to the downward shift of the resonant frequencies, the amplitude of vibration has been found to increase significantly with an increase of the V_{dc} tuning voltage. As illustrated in [Figure 4.11b](#), the amplitude of vibration of the fundamental resonant frequency has been observed to increase from $\sim 0.5 \mu\text{m}$ at 1 V to $\sim 2.3 \mu\text{m}$ at 5 V. The outcomes of these observations indicate that the fabricated resonators possess high dynamic tuning sensitivity for both resonant frequencies and vibration amplitude. It is concluded, therefore, that the demonstrated resonators of fixed-fixed microbeams could be used as highly sensitive acoustic transducers.



(a)



(b)

Figure 4.11: Measured frequency response of a 3.4-mm-long microbeam to different DC tuning voltages. (a) Fundamental resonant frequency shift versus DC tuning voltage. (b) Amplitude of vibration versus fundamental resonant frequency.

4.6 Summary

This chapter has been dedicated to the design optimisation, fabrication and dynamic characterisation of electrostatically-driven resonators of tantalum. The accomplished work and findings are summarised as follows::

An array of ultra-long resonators of tantalum with length ranging from 1 to 3.4 mm has been realised. The beams' length and vertical deflection to length aspect ratio of 1:3400 are the major features of the resonators. The realisation of suspended and undeformed microstructures has been achieved by controlling the process-induced stress during the fabrication process.

The resonant frequencies of the beams have been measured by driving the beams electrostatically. The resonant frequency dependence on the resonator length and tensile residual stress have been investigated numerically and analytically. The frequency tuning in response to different DC tuning voltages has been demonstrated. A spring softening effect with a downward shift of the resonant frequency and an increase of the vibration amplitude has been induced in the resonators. The implemented device has shown a possibility of operating in a low-frequency regime with high tuning sensitivity under the use of relatively small DC tuning voltages, promising practical applications for low-frequency-operated devices. The results produced in this work provide useful information about the fabrication-induced stress effects of micro-suspended beams and can be used for the optimisation of the design and manufacturing of MEMS-based materials and devices.

Chapter 5

Properties and Transfer Challenges of Graphene

This chapter is dedicated to describing the unique properties of the two-dimensional (2D) material of graphene. First, an overview of graphene will be provided, focusing on its extraordinary mechanical and electrical properties that can be exploited to produce ultra-thin suspended devices. Then, the currently used fabrication methods of graphene membranes will be described. The focus will be directed on the challenges involved in transferring a large-area graphene film from its growth substrate to a substrate of interest.

5.1 Introduction to graphene

Graphene is a two-dimensional material consisting of a single layer of carbon atoms that are arranged in a hexagonal (honeycomb) lattice, as shown in [Figure 5.1](#). In fact, graphene can be considered as the basic building block for other carbon allotropes. For example, graphene sheets can be reconstructed to form structures such as fullerene (0D), carbon nanotubes (1D), and graphite (3D). There was a viewpoint that crystalline structures

of two-dimensional materials cannot exist because it was believed that such structures are unstable thermodynamically [131]. The possibility of the existence of 2D materials was thought to be unlikely until 2004, when two scientists from the University of Manchester discovered graphene material for the first time. The scientists, who were awarded the Nobel Prize in Physics in 2010 for their pioneering research on graphene, used a simple method to exfoliate mechanically a graphene sheet from graphite [132]. In the initial fabrication technique, adhesive tape used to peel off individual layers of graphene from graphite and transfer them onto a silicon oxide substrate. Since then, graphene has been the focus of intense research by the scientific community. As graphene research increases with relentless pace, industrial sectors from various disciplines show a growing interest in graphene-based

technologies.

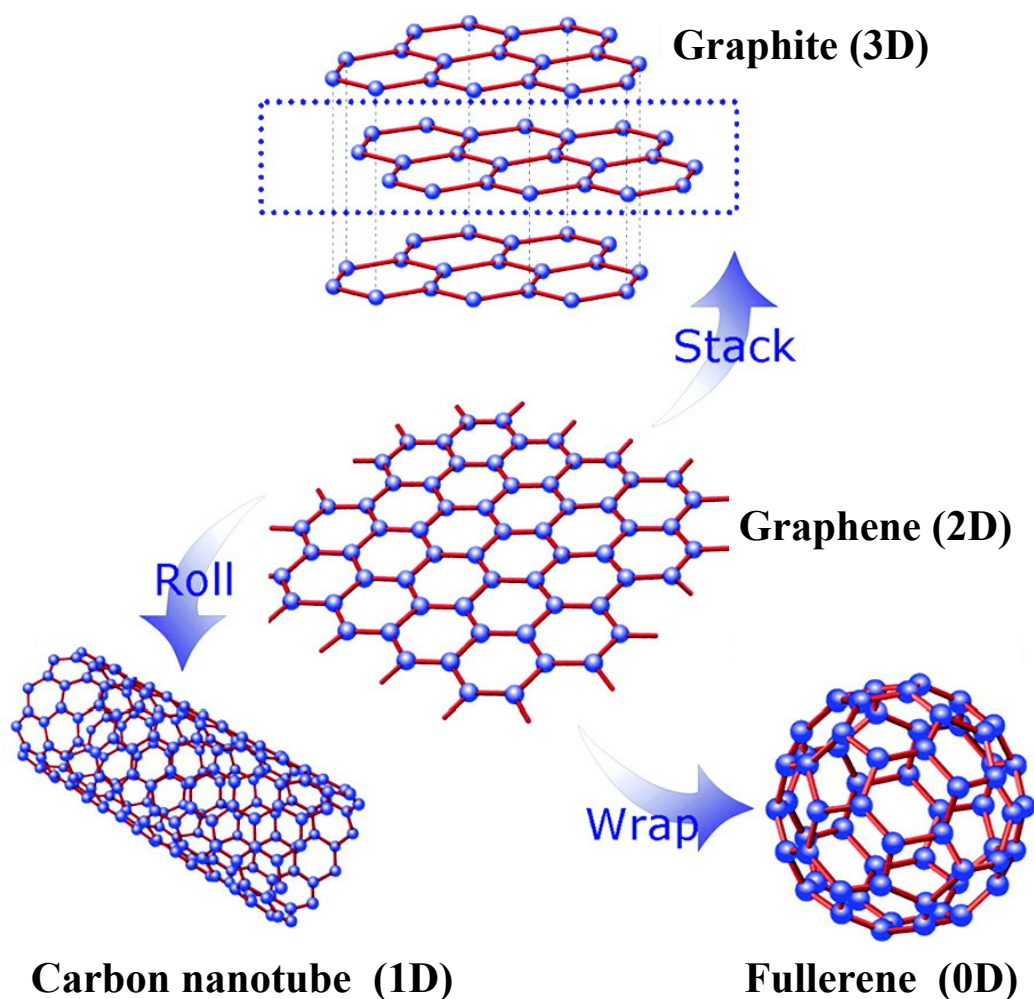


Figure 5.1: Carbon allotropes based upon 2D graphene. Reprinted with permission from American Chemical Society [132].

5.2 Properties of graphene

The increasing interest in graphene is due to its exceptional properties. The main factor that distinguishes graphene from other existing materials is its unique crystal structure. In the graphene lattice, nearest-neighbour carbon atoms are separated by a distance of 1.42 Å and connected to each other by strong covalent σ bonds [133]. The covalent σ bonds are formed when electrons in atomic

valence orbitals of $2s$, $2p_x$ and $2p_y$ are hybridised into sp^2 orbitals. Since the fourth $2p_z$ orbital is oriented perpendicular to the planar structure of graphene sheet, its valence electron will not interact with the in-plane σ electrons. When $2p_z$ orbitals of neighbouring carbon atoms are overlapped by binding covalently to each other via π bonds, a delocalised π band is constructed [134]. The half-filled formed band is divided into valence band π (occupied) and conduction band π^* (unoccupied).

5.2.1 Electrical properties of graphene

The remarkable electronic properties of graphene are basically attributed to π bands. Unlike other known materials, ideal (pure) graphene does not have a band gap. This means that there is no gap in energy between the valence and conduction bands of graphene material. As shown in Figure 5.2, the filled valence and unoccupied conduction bands represented by Dirac cones meet at points called Dirac points. The Dirac points are located at the corners of the Brillouin zone [134].

Due to the unique zero-band gap characteristic, graphene is considered as a semi-metal and a zero-gap semiconductor. Therefore, the peculiar electronic structure of graphene enables the electrons in graphene to conduct electrical current in an extremely greater manner than other traditional semiconductors and metals [135]. The characteristic that features the superior electrical properties of graphene is its extremely high intrinsic charge mobility that ranges from 15000 to 250 000 cm^2/Vs [136, 137]. At a temperature of 4 K, graphene mobility reaches values of 350 000

– 500 000 cm²/Vs [138].

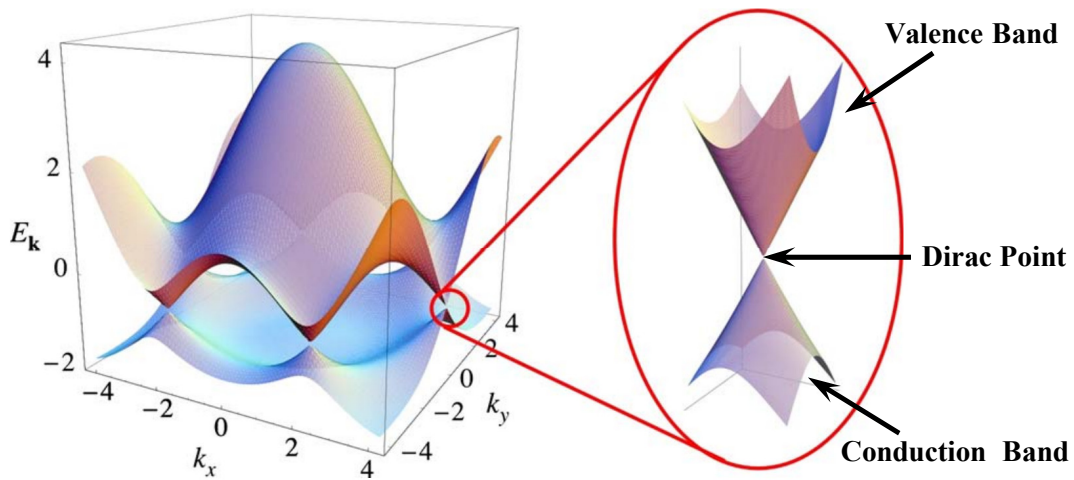


Figure 5.2: Electronic band structure of graphene showing the conduction and valence bands meeting at the Dirac points. Adapted from [139].

5.2.2 Mechanical properties of graphene

Although graphene is considered the thinnest elastic material ever to exist in nature, it possesses special mechanical properties. In fact, the exceptional mechanical strength of graphene is attributed to the hexagonal planar structure that results from the sp^2 hybridisation between s and p orbitals [134]. Due to its extremely high intrinsic mechanical strength of ~ 130 GPa [140], graphene has been manifested as the strongest material ever discovered. In addition, graphene has a remarkable Young's modulus of ~ 1 TPa for monolayer and ~ 0.5 TPa for multilayer [141]. Moreover, ultra-low mass density of 2200 kg/m³ [62] has been measured for graphene. Another interesting property of graphene material is its high ductility that enables graphene membranes to be stretched up to ~ 20 % [142]. The superior mechanical properties of graphene can be exploited to realise large free-standing suspended structures. Therefore, graphene can be considered as a promising material for acoustic resonators.

5.2.3 Thermal properties of graphene

In addition to the special electrical and mechanical properties, graphene has extraordinary thermal properties. For example, the measured thermal conductivity of graphene is found to be in the range of $\sim 2000 - 5300$ W/mK [138, 143]. So far, this is the largest thermal conductivity ever known. A negative coefficient of thermal expansion (CTE) of about -7×10^{-6} K⁻¹ [71, 138] is another unusual property that differentiates graphene from conventional materials. Due to its negative CTE, a graphene membrane contracts upon heating, which is different from the normal thermal behaviour of other materials. Therefore, it is possible to produce graphene-based resonators and exploit the superior thermal properties of graphene to drive the resonators into resonance electrothermally. For example, when an electric current flows through a membrane of graphene, heat will be generated causing the membrane to deform (expand or contract) accordingly.

5.3 Fabrication of graphene films

To date, several techniques have been developed to synthesise graphene membranes on different substrates. Mechanical exfoliation of single crystal graphite was the first demonstrated synthesis method of graphene film [144]. However, the graphene films prepared by this method are small in size, have irregular shapes and their thicknesses are uncontrollable [145]. The small flakes produced in the mechanical exfoliation method are unsuitable for large scale graphene-based devices or industrial production.

Another developed technique to synthesise graphene is through epitaxial growth upon a silicon carbide (SiC) substrate. The method is based on a high thermal decomposition of silicon carbide

[146]. Although this method offers some benefits such as producing large-scale films with good electronic properties, the synthesis conditions are rigorous, namely, a high temperature (1650 K) and ultra-high vacuum. The most widely used synthesis technique is chemical vapour deposition (CVD) growth of graphene films on transition metal substrates [145, 146]. This method has the advantages of producing relatively high-quality graphene on a large scale. Therefore, CVD graphene films have been used for all graphene-based resonators fabricated and produced in this work.

5.3.1 Graphene on shallow cavities: Wet transfer

To exploit its unique properties, CVD graphene membranes have to be transferred from its growth metal substrate to a substrate of interest. For resonance-based transducer devices such as microphones, graphene membranes have to be suspended over a cavity. The depth of the cavity is in the range of a few microns. For example, the air gap distance between the vibrating diaphragm and the back plate in capacitive MEMS microphones is 2 μm or less. Therefore, in this work resonators consisting of graphene membranes suspended above shallow cavities have been fabricated. The fabrication process flow for the target substrate and transfer procedure steps of graphene-polymer films are shown in [Figure 5.3](#).

To prepare the target substrate of the resonator, an insulating layer of ~ 2 μm -thick silicon dioxide (SiO_2) has been deposited on a P-type silicon substrate via chemical vapour deposition ([Figure 5.3a](#)). Next, ~ 2.3 - μm -thick layer of photoresist has been spin coated on top and patterned photolithographically in circular, square and rectangular shapes ([Figure 5.3b](#)). To create 2- μm -deep cavities, a reactive ion etching (RIE) technique has been used to

etch anisotropically the exposed oxide ([Figure 5.3c](#)). Consequently, circular, square and rectangular cavities with a depth of 2 μm have been created.

To transfer a graphene membrane from its growth substrate to the target substrate, a polymer film of Poly(methyl methacrylate) (PMMA) has been used as a supporting layer during the transfer. Firstly, $\sim 700\text{-nm}$ -thick layer of PMMA (molecular weight ~ 996000 with a concentration of 4% in chlorobenzene) has been spin coated on top of the copper foil and annealed at 80 $^{\circ}\text{C}$ for 2 minutes ([Figure 5.3d](#)).

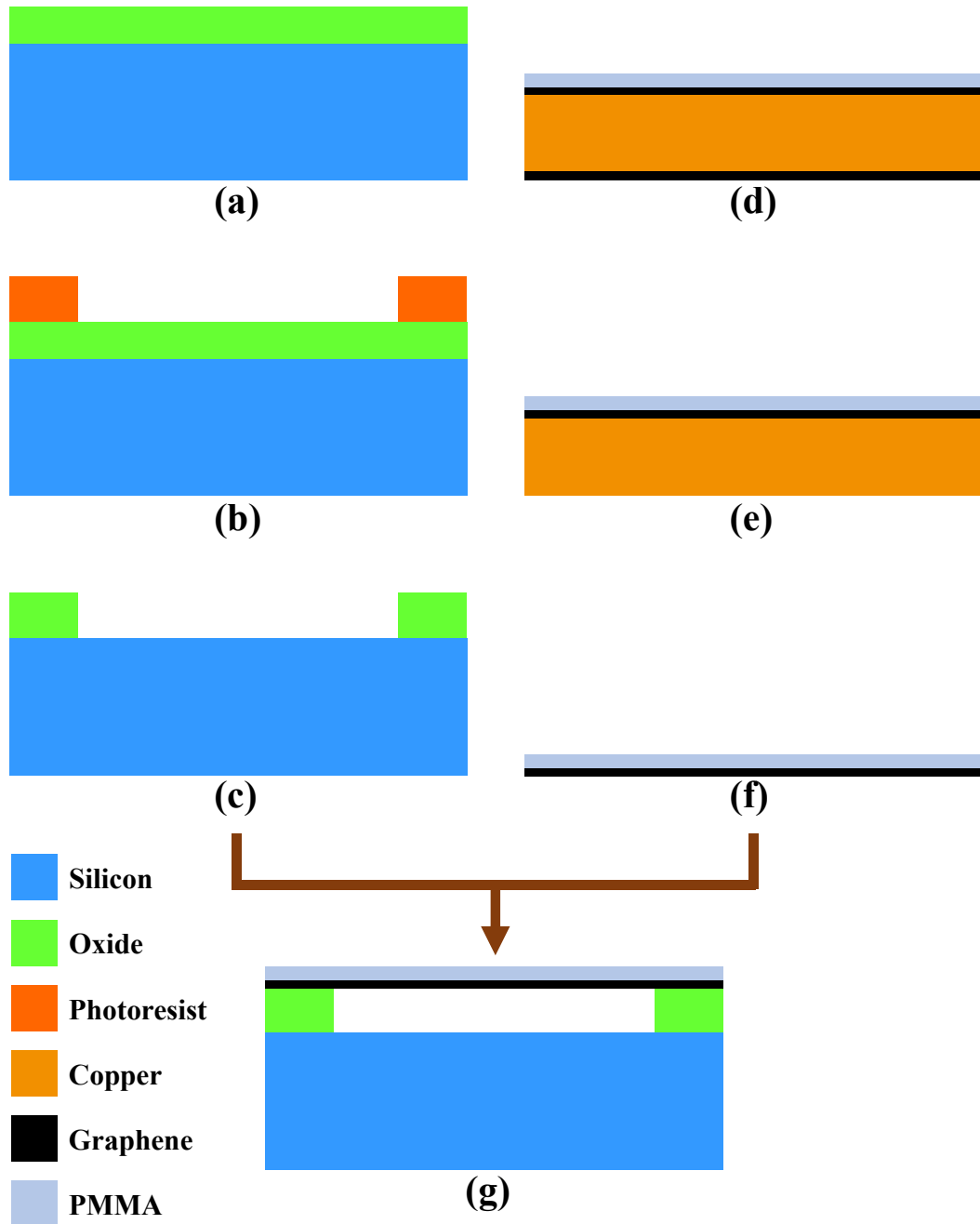


Figure 5.3: Schematic illustration of the fabrication process of graphene-based resonators showing the main steps to prepare a patterned substrate and the transfer procedure of graphene-PMMA films from a copper substrate to the patterned substrate. **(a)** CVD silicon dioxide deposited on a silicon substrate. **(b)** Photoresist spin coated and patterned. **(c)** Silicon dioxide etched, and circular, square and rectangular cavities created. **(d)** PMMA spin coated on the top side of copper foil and baked. **(e)** Backside graphene etched. **(f)** Copper metal etched, and graphene-PMMA films floated on DI water. **(g)** Graphene-PMMA films scooped and transferred onto a SiO₂/Si substrate.

To allow the PMMA film to dry completely, the coated foils have been kept in a cleanroom environment for 24 hours. Afterwards, the graphene membrane on the backside of the copper foil has been etched using an oxygen plasma system (Figure 5.3e). Then, the samples have been floated on a copper etchant solution of 1 M of ferric chloride (FeCl_3) to etch the copper foil and release the graphene-PMMA membranes (Figure 5.3f). To remove the etchant residues, the membranes have been rinsed in hydrochloric acid (HCl 10%) and deionised water (DIW) many times. At the final stage, the floating membranes have been scooped out and transferred onto the cavity-bearing substrates (Figure 5.3g).

5.3.1.1 Post-transfer characterisation

After transferring the graphene-PMMA films to the patterned substrates, the devices have been dried at room temperature for 12 hours to ensure that the films are adhered properly to the substrate. The films cover circular cavities with a diameter of 6 mm and square as well as rectangular cavities with a side length of 3 – 5 mm. Optical images of graphene-PMMA films transferred onto substrates with circular and square cavities are shown in Figure 5.4.

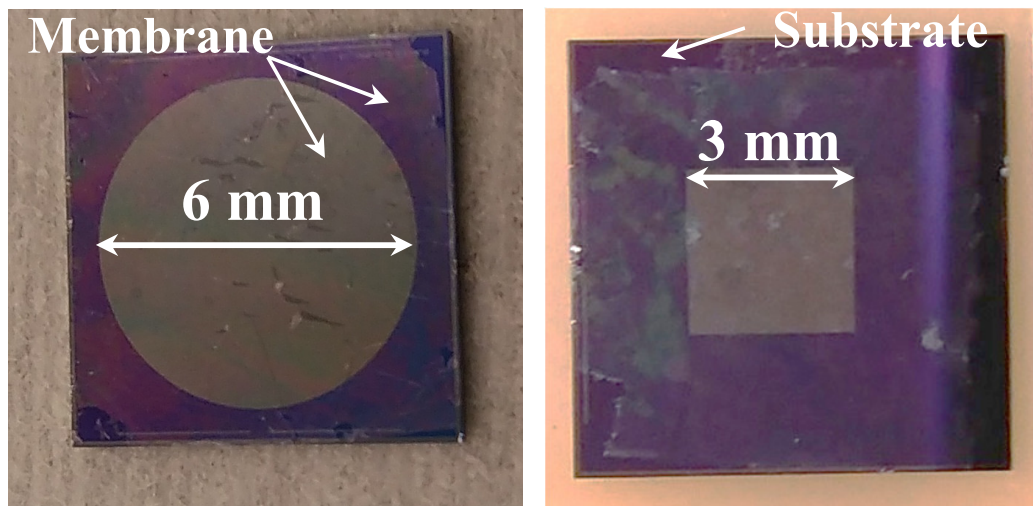


Figure 5.4: Optical image of monolayer graphene, supported by a layer of PMMA, after being transferred to SiO_2/Si substrate with circular and square cavities.

Although the transferred membranes cover fully the cavities underneath, defects such as residues and small holes have been observed. These defects are induced into the membranes during the transfer process due to the wet etching solution and the multiple mechanical handling steps involved. In addition to the defects, the transferred membranes have been found to be bent downward towards the substrate. It is highly possible that the downward membranes sagging is attributed to transfer-related stiction.

5.3.1.2 Raman spectroscopy

Precise determination of layer thickness, grain boundaries, strain and possibly quality for graphene thin films can be achieved by a powerful and non-destructive technique of Raman spectroscopy, which is a vibrational technique that provides a fast characterisation of graphene properties. In general, Raman spectroscopy is based on an inelastic scattering process, in which the Raman spectrum can be detected when a monochromatic laser is irradiated towards a sample and the light is scattered [147]. A film of single or multilayer graphene exhibits two fundamental sets of peaks, namely, G and 2D bands.

In the Raman spectrum of graphene, peaks of G and 2D bands appear at $\sim 1580 \text{ cm}^{-1}$ and $\sim 2700 \text{ cm}^{-1}$, respectively [148]. The Raman spectrum measurement of a thin-film of graphene-PMMA suspended over circular cavities of a SiO_2/Si substrate is shown in Figure 5.5. Three main bands, D, G and 2D, have been observed in the spectrum. A sharp symmetric peak of 2D band has been observed at $\sim 2705 \text{ cm}^{-1}$. For the G band that corresponds to vibrational phonon mode at high frequencies, the peak has been found at 1587.93 cm^{-1} . To determine the thickness of the graphene film used in the transfer process, an empirical equation has been

applied as follows [149]:

$$n^{1.6} = \left(\frac{11}{W_G - 1581.6} \right) - 1 \quad (5.1)$$

where n is the number of film layers, and W_G is the band position in wavenumbers. From the use of 1587.93 cm^{-1} in Equation (5.1), it has been confirmed that the graphene film used in our resonators is a single layer graphene. Also, the quality of the graphene films can be identified from the peak intensity ratio of the 2D and G bands (I_{2D}/I_G), or from the sharp symmetric peak of 2D band. For our membranes, the I_{2D}/I_G ratio has been found to be ~ 1.2 , which indicates that the quality of graphene is relatively high. However, the appearance of the D band in the spectrum indicates that the transferred graphene has defects.

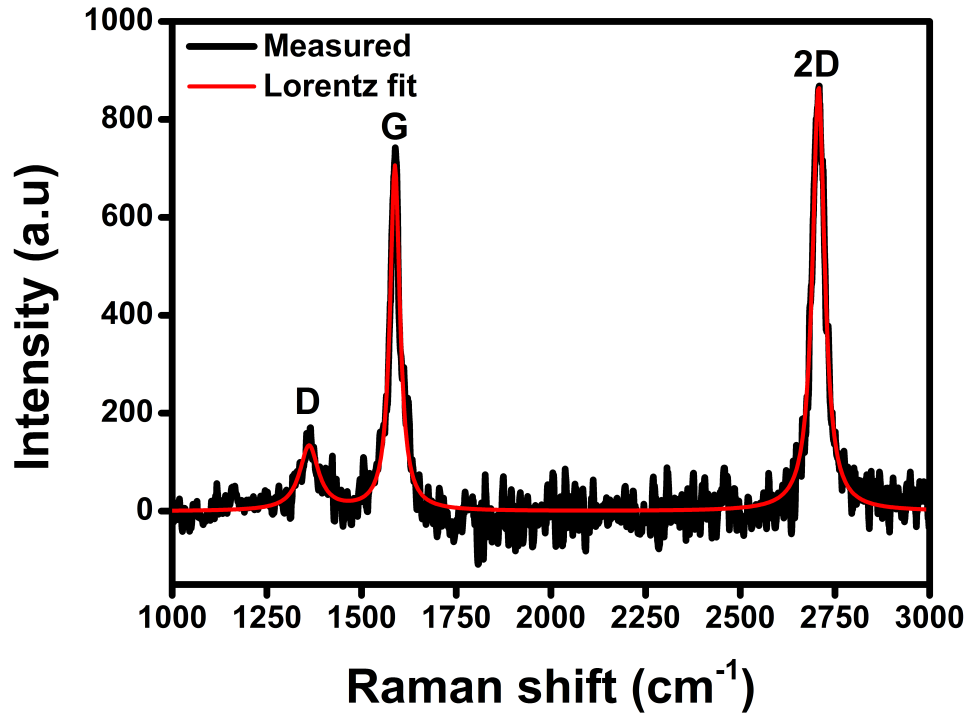


Figure 5.5: Lorentzian fitted Raman spectrum measurement of graphene-PMMA films transferred onto a SiO_2/Si substrate, showing the D, G and 2D bands.

5.3.1.3 PMMA removal from graphene films

The role of PMMA film in graphene preparation is to act as a temporary support layer. During the transfer, CVD graphene membranes must be protected from mechanical deformation such as cracking or tearing. After the transfer, the support layer of PMMA can be removed completely, thus leaving behind a membrane of graphene only. For the resonators fabricated here, a combination of wet and dry removal techniques has been utilised to detach the PMMA layer from the graphene membrane. First, the films have been immersed in acetone bath for 50 minutes, following by a 30-minutes-long immersion in isopropyl alcohol (IPA). After the wet removal, the films have been subjected to annealing at 350 °C for 2 hours. The annealing has been performed under the use of nitrogen gas.

After the removal processes of PMMA layers, the graphene film-based resonators have been characterised optically to examine whether the PMMA films have been removed completely without damaging the graphene membrane. Images of the optical measurements of the resonators after the removal process are in [Figure 5.6](#).

It can be seen from the optical images that PMMA film residues have not been removed thoroughly. Visible residues are left on the graphene surface in the cavity and substrate areas. It appears that the removal process of PMMA film inflicts significant damage on the graphene membrane.

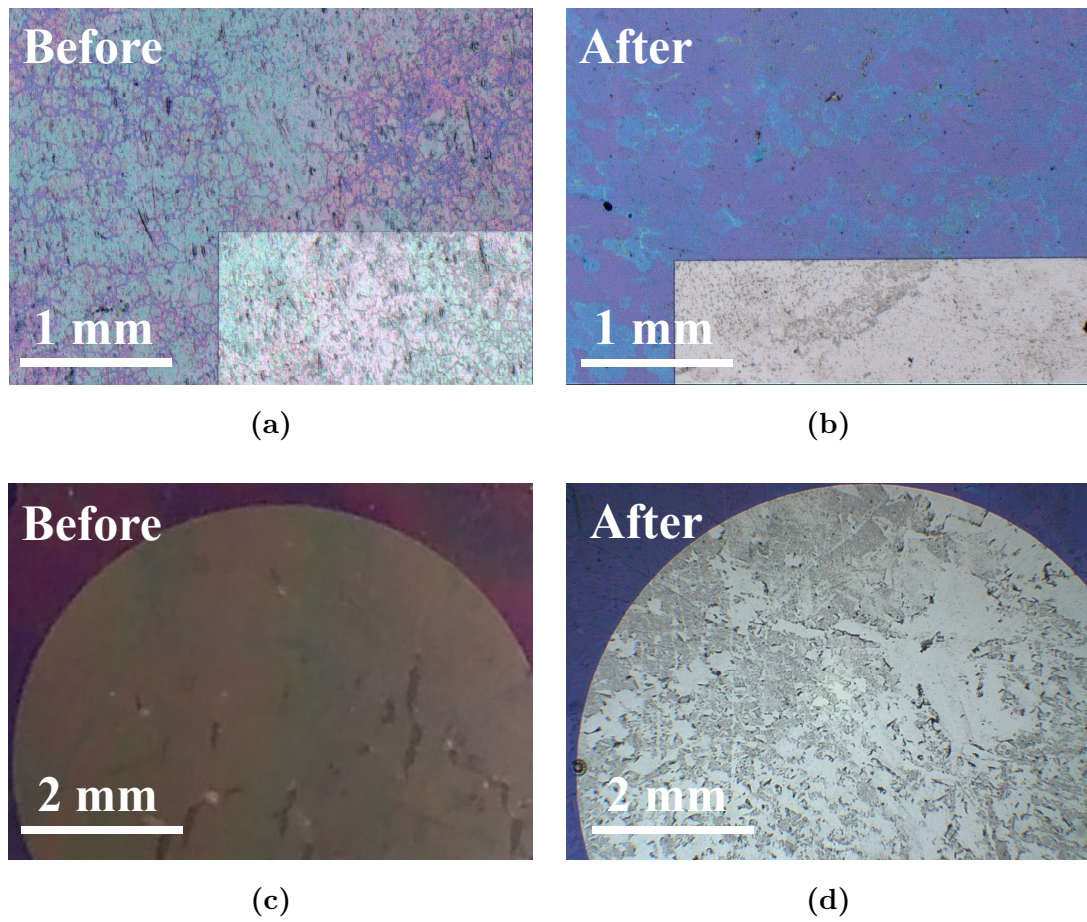
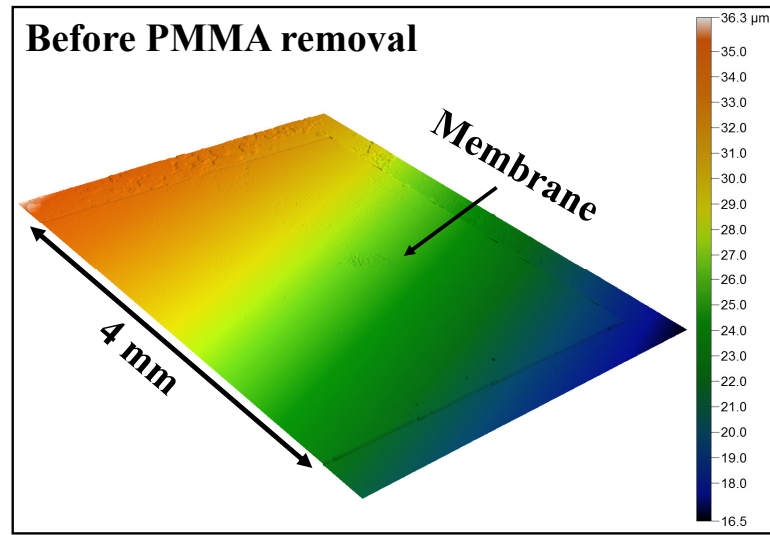
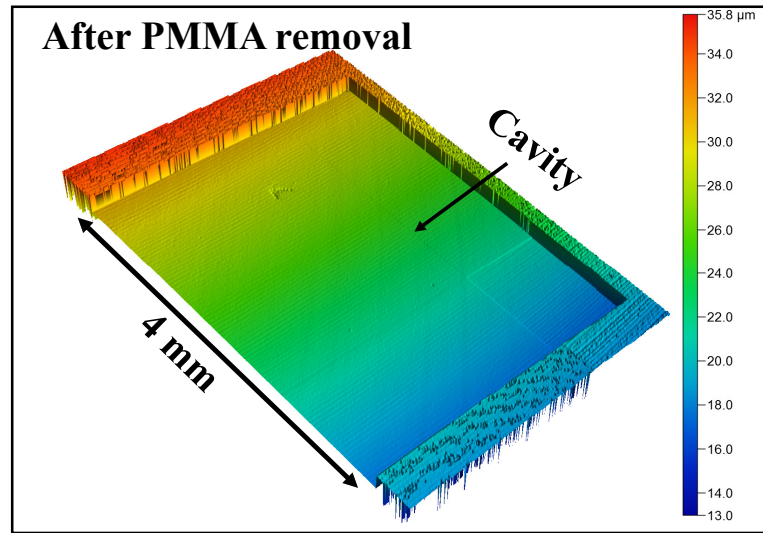


Figure 5.6: Optical images of square and circular graphene-PMMA membranes before (a, c) and after (b, d) removing the PMMA layer.

To inspect whether the graphene membrane could survive and remain suspended over the cavities after the removal process of PMMA, the membrane-bearing resonators have been characterised interferometrically. 3D interferometric images of a graphene-PMMA membrane transferred onto a rectangular cavity are shown in [Figure 5.7](#). Since the graphene film is a transparent material, a thin layer of gold has been deposited on top to provide precise measurements of the device.



(a)



(b)

Figure 5.7: White-light interferometry measurements showing 3D topology images of a rectangular graphene-PMMA resonator before (a) and after (b) the removal of PMMA film.

The interferometry images compare the measured profile of the resonator before and after removing the supporting PMMA layer. It has been observed that the graphene membrane has been damaged, partially or completely, during the PMMA removal. As shown in Figure 5.7b, there is no indication that a suspended graphene remains at all.

However, further Raman spectroscopy measurements have been performed, and confirmed that some flakes of graphene membranes remain at the bottom of the cavity. It is possible that the graphene membrane becomes weak after removing the support layer, thus breaking into small flakes and sticking to the cavity bottom. It can be concluded from these observations that the use of a wet transfer method to transfer large membranes of graphene to shallow cavities leads to a significant damage of the transferred membranes. Moreover, it is possible that — even with the successful transfer and removal processes — the membranes will not be suspended completely.

5.3.2 Graphene on shallow cavities: dry transfer

To investigate whether avoiding a wet-based transfer technique would provide more robust membranes with less defects and deformations, a dry-based transfer method has been developed. The developed technique aims to transfer graphene-PMMA membranes to 2- μm -deep cavities without involving solutions such as water or acids. In this technique, a commercial CVD-graphene of 6 layers from Advanced Graphene Products has been used. After coating graphene with $\sim 1.5\text{-}\mu\text{m}$ -thick layer of PMMA, and etching the copper, the entire graphene-PMMA film has been left to dry without being attached to a substrate. Then, the fully-dried sheet has been cut into small films that can fit the cavities-bearing chips. A schematic diagram of the dry transfer is shown in [Figure 5.8](#).

To transfer the prepared films onto the cavities, the chips have been cleaned and rinsed in alcohol and treated with O_2 plasma for a few minutes. Afterwards, the transfer has been performed by placing the membrane on top of the cavities. To adhere the film properly to the substrate, a tiny drop of DI water has been applied

at the edges of the supporting frame. Finally, the entire system has been placed on a hotplate at 80 °C for 10 minutes. To achieve good adhesion between the film and substrate and to enable a maximum stretch of the transferred membrane, a further annealing step at 140 °C for ~ 5 minutes has been performed.

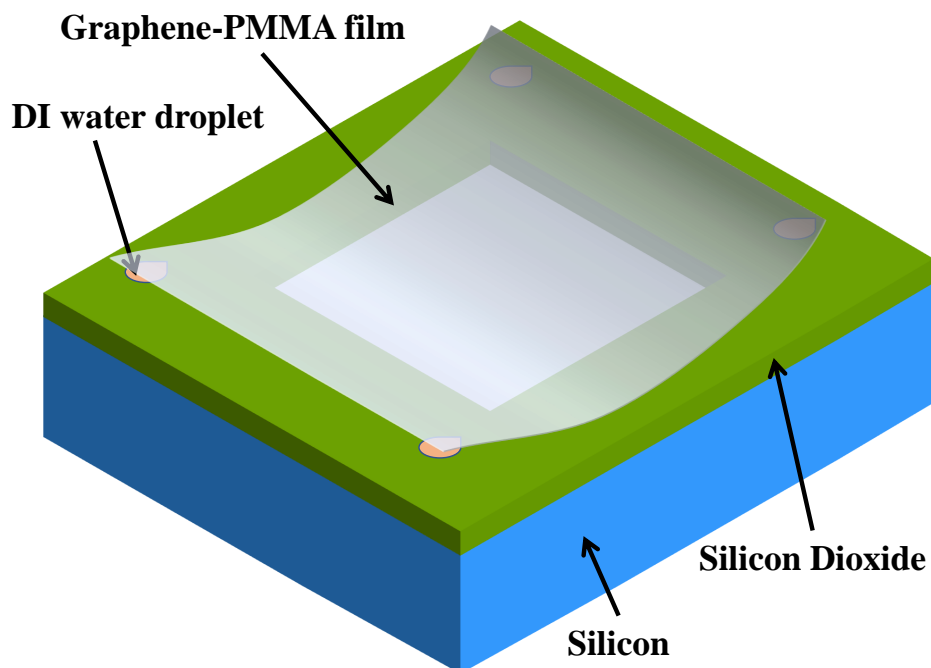


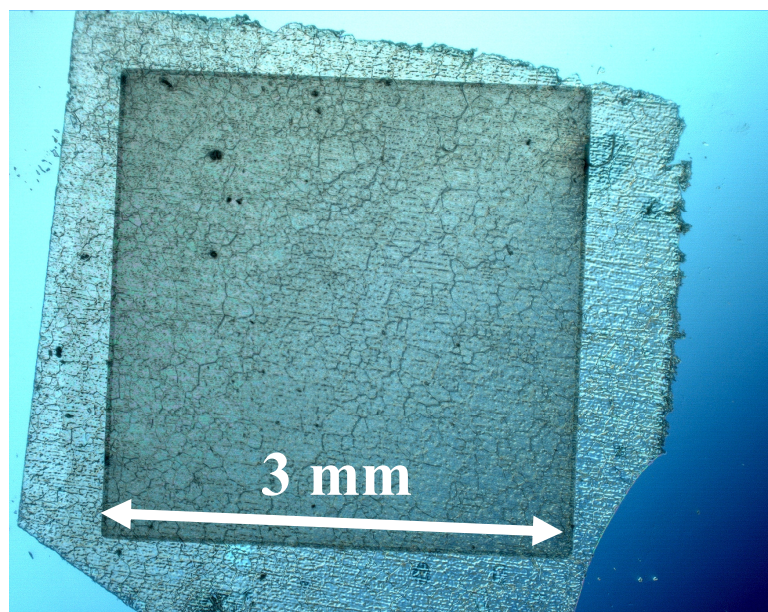
Figure 5.8: : Illustration diagram of the dry transfer of graphene-PMMA films to a SiO₂/Si substrate with a square cavity.

5.3.2.1 Post-transfer characterisation

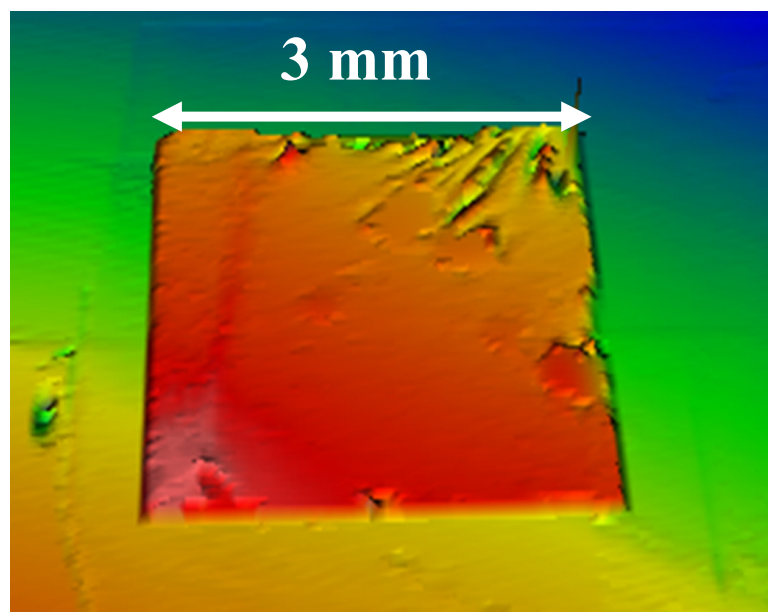
The transferred membranes have been characterised using an optical microscope and a white light interferometer, as shown in [Figure 5.9](#). Although no solvents have been involved in the dry-transfer process, the transferred membranes have exhibited large deformation. For example, a series of wrinkles or ridges have been observed in the transferred membrane, as shown clearly in the 3D interferometric measured profile in [Figure 5.9b](#). The size of the of developed wrinkles/ ridges is more likely to be affected by the transfer process

parameters.

Despite the fact that both the wet and dry transfer processes are performed manually, it seems that the dry-transfer method is relatively less controllable. In other words, the magnitude of developed deformation has been found to be larger in the dry-transferred membranes than the wet-transferred ones.



(a)



(b)

Figure 5.9: Optical (a) and 3D interferometric (b) images of dry-transferred graphene-PMMA films.

5.4 Graphene transfer challenges

Mechanically, a graphene sheet (mono or multilayer) is sufficiently fragile that it can be wrinkled or ruptured easily during the

fabrication process. The challenge becomes even greater with the increase of graphene sheet area. The most critical step in the fabrication process is to transfer graphene from its growth substrate to a substrate of interest without damaging the graphene sheet film or the surface of the target substrate. Despite all the enormous efforts that have been made on the development of graphene synthesis and transfer methods, there are still undoubtedly several challenges facing the realisation of high-quality graphene films on a large scale.

It has been shown that the fabrication of large area graphene-based resonators using wet or dry transfer processes results in different forms of distortion, deformation and cracking in the transferred membranes. The difficulties appear when solvent rinsing or dry annealing processes are involved in the fabrication. So far, graphene membranes prepared by mechanical exfoliation, polymer-assisted transfer, polymer-free transfer, roll-to-roll process and transfer-free approaches [131, 150–152] suffer from several problems, most of which are: small size, low yield, residue defects, buckling, folding and rupturing. Therefore, it can be concluded that there is a significant need to optimise either the transfer process or the resonator design.

5.4.1 Optimisation of graphene transfer and design

One possible way to transfer successfully a thin-film of graphene to a substrate of interest is by using a relatively small cavity. In this case, the size of graphene films must be reduced to a few micrometers, so that suspended graphene films with high yield can be obtained. However, resonators based on small-area graphene films are usually operating at high frequencies (e.g. in the range of MHz), and thus they would not be an appropriate for acoustic applications.

Therefore, it has been proposed here an optimised design of graphene-based resonators that ensures a successful transfer process of graphene-PMMA films to the desired substrate with high coverage. An illustration of the proposed design is shown in [Figure 5.10](#). First, the depth of the cavity has been increased from 2 μm to 380 μm . In such a case, the entire layer of the substrate has been etched ([Figure 5.10a](#)), hence preventing the free-standing film from any possible stiction failure or downward collapsing. In addition, after being transferred to the target substrate ([Figure 5.10b](#)), the films have been left to dry for a short time, and then annealed at 80 °C and 140 °C for 10 and 5 minutes, respectively. In this way, the films are allowed to be stretched to their maximum limit, and therefore they are unlikely to experience large deformation.

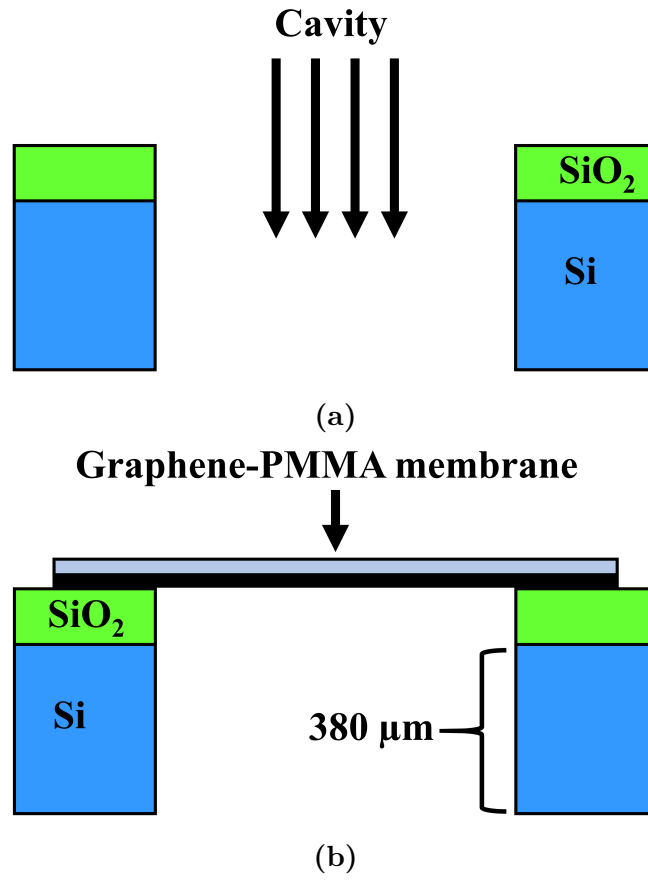


Figure 5.10: Schematic diagram of the optimised design of a graphene-based resonator. (a) The substrate before the transfer, showing the Si layer being etched entirely. (b) The final structure of the resonator showing the graphene-PMMA membrane being transferred onto the target substrate.

The main advantage of using graphene membranes is that graphene can be stretched up to $\sim 20\%$ [142] of its original length. Compared to other metallic coatings, the high ductility of graphene enables a graphene-based membrane to expand and contract to its maximum limit (i.e. 20%) without exhibiting undesirable deformations such as tearing and cracking.

If it is assumed that the transferred film of graphene-PMMA bends downward for a few micrometres, this bending will not influence the operation of the resonator, since the cavity beneath the film is opened fully. The proposed simple design has been demonstrated successfully for both wet or dry-transferred films, and such resonators can be actuated either electrothermally or piezoelectrically. For electrostatic actuation, an actuation electrode separated by a small distance from the free-standing film is required, which has not been included in the current design. More detail about the design, fabrication and electrothermal actuation of graphene-based resonators will be provided in the next chapter.

5.4.2 Post-fabrication characterisation

Based on the optimised design, the transferred films have been characterised by an optical microscope, a white light interferometer and scanning electron microscopy (SEM). The high yield of the transferred graphene-PMMA films with full surface coverage is evident from the optical and SEM images shown in [Figure 5.11](#). It can be seen that the films have covered the cavity entirely. No significant deformation has been observed in the transferred films. Note that some defects and holes have been introduced into the films during the characterisation process due to repeated mechanical

handling.

To inspect whether the transferred membranes buckle upward or bend downward, topography measurements of the membranes have been performed using white light interferometry. From the typical WLI surface measurement (Figure 5.11c) and the actual profile of the suspended membrane (Figure 5.11d), it can be seen that the membranes have not exhibited upwards or downwards deflection, showing a relatively straight profile across the cavity area.

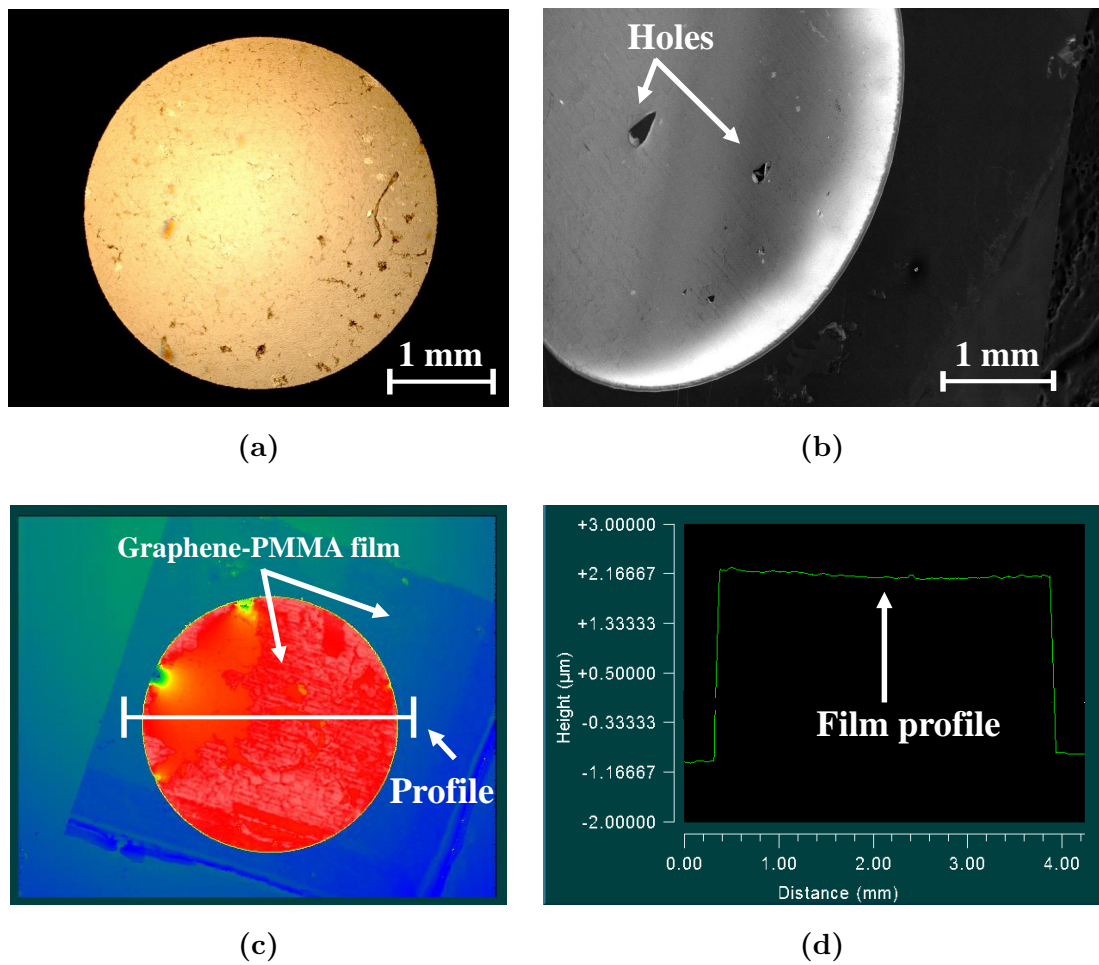


Figure 5.11: Characterisation of the graphene-PMMA membranes transferred over a circular cavity with a diameter of 3.5 mm. (a) Optical image of the suspended membrane taken from the bottom of the cavity. (b) SEM image of the membrane over the circular cavity. (c) WLI image showing the surface topography. (d) The actual profile of the suspended membrane over the cavity obtained from (c). The holes and defects shown in the SEM images have been introduced during the characterisation procedure.

5.5 Summary

In this chapter, an overview of graphene films and the potential use of its unique properties to realise large-area resonators has been given. The challenges associated with the transfer process of graphene membranes have been presented. The accomplished work and findings are summarised as follows:

Being one of the thinnest, strongest and best heat- and electricity- conducting materials, graphene is the ideal candidate for use as a membrane in an acoustic transducer, such as a microphone. To fabricate a graphene-based resonator, CVD graphene thin-films have been transferred from a growth substrate to a substrate of interest using a polymer-assisted transfer method. A thin-film of PMMA polymer has been used as a supporting layer to protect the graphene sheet during and after the transfer. In this work, wet and dry transfer methods have been employed to transfer graphene-PMMA thin-films on either shallow or deep cavities. For shallow circular, square and rectangular cavities with a depth of 2 μm , the transferred films have been found to experience several forms of deformation such as wrinkling, folding, ridging, cracking.

Although both wet and dry transfer methods have their advantages and disadvantages, the wet-based transferred films are found to be less deformable than the dry-based transferred ones. For example, a relatively flat thin-film can be obtained by the wet transfer method as the film floats homogeneously on the DI water. However, possible damage in the transferred films might occur due to a stiction-related failure.

To tackle the challenges observed in the shallow cavity devices, a simple design of graphene-PMMA resonators has been proposed and optimised. The design is based on very deep cavities (380 μm), which enables the graphene-based films to be suspended

freely on the cavity without developing a substantial upward or downward mechanical deformation. The proposed design is simple and reproducible enough to achieve free-standing films with a remarkable diameter to thickness (6 layers of graphene and 350 nm of PMMA) aspect ratio of $\sim 10,000$.

Chapter 6

Fabrication and Characterisation of Tunable Graphene Resonators

6.1 Introduction

In this chapter, an experimental realisation of graphene-based resonators is provided. The developed design described in the previous chapter will be utilised to demonstrate a bilayer system consisting of graphene and PMMA thin-films. For the potential use of graphene-based transducers in acoustic applications, large circular and square bilayer membranes on a millimetre scale will be fabricated using the optimised transfer process. In addition, an electrothermal transduction technique will be employed as an actuation mechanism to drive the resonators into resonance. The resonators oscillation will be read-out optically using laser Doppler vibrometry. The focus of this chapter will be directed mainly on the dynamic behaviour of the bilayer structures. It will be investigated comprehensively how the dynamic characteristics such as the resonant frequency and amplitude of vibration can be tuned by considering the effect of actuation parameters such as driving configuration and tuning voltages.

6.2 Fabrication procedure of large resonators of graphene-PMMA

Graphene is an extraordinary material that has shown superiority over other known materials in MEMS and NEMS. The rapid advances in fabrication technologies of 2D materials have led to graphene-based micro- and nanomechanical resonators/actuators being developed for potential applications in the sensing and actuation fields. However, the size of graphene sheets used in most existing electromechanical resonators is within the nano- and micrometre scale [71, 153, 154]. One of the main drawbacks of reducing the vibrating structures' dimensions to the nano- and micro-scale is that these devices can operate in the high-frequency range (i.e. MHz – GHz) only [155–157]. In particular, the use of only a graphene sheet (mono or a few layers), which has atomic thickness and high stiffness and ultralow mass density, as a resonant element will result in vibrational devices that are unsuitable for audio frequency (i.e. < 20 kHz) applications such as microphones and other acoustic transducers.

In order to enable the graphene-based resonator to be operated at low frequencies (e.g. audio range 20 Hz – 20 kHz), large membranes of the macro-scale size with a large aspect ratio of area to thickness have to be suspended over a cavity. Therefore, the simple and reproducible technique that has been developed will be utilised to transfer ultra-large graphene-PMMA circular membranes with a diameter of 3.5 mm and square membranes with a side length of 3 mm on top of a cavity. Using this technique, a thin film of PMMA has been attached to the graphene sheet to act as a mechanical supporting layer during and after the transfer process. The PMMA thin film will not be removed after the transfer, thus

the final structure of the resonator will be in the form of a bilayer membrane. The use of a thin film of PMMA that has lower density and elasticity than graphene as a second layer has the advantages of enhancing the durability of the entire bilayer structure and lowering the frequency of operation when the system is operating in the membrane regime.

6.2.1 Preparation of target substrate

To fabricate graphene-PMMA resonators, a desired target substrate has been prepared. A schematic of the process flow for the fabrication of the target substrate is shown in [Figure 6.1](#). Firstly, ~ 250 -nm-thick dielectric layer of silicon dioxide (SiO_2) has been deposited on a p-type silicon substrate by chemical vapour deposition ([Figure 6.1a](#)). To create electrode pads for electrothermal actuation, a layer of 500 nm of aluminium has been deposited on top using a DC sputtering system and patterned by a lift-off process ([Figure 6.1b](#)). After spin coating and patterning a layer of photoresist, circular cavities with a diameter of 3.5 mm have been defined. Subsequently, reactive ion etching (RIE) has been used to etch the oxide layer, while utilising inductively coupled plasma (ICP) with a deep reactive ion etching (DRIE) technique to etch through the whole depth (380 μm) of the silicon substrate ([Figure 6.1c](#)). The same procedure described above has been applied to create square cavities with a side length of 3 mm. After stripping the photoresist and dicing the substrate wafer, 7 mm x 7 mm chips containing a single circular or square cavity have been created finally.

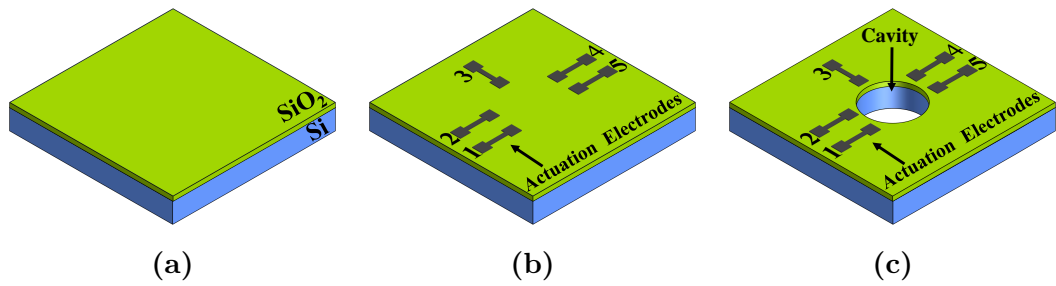


Figure 6.1: Schematic diagram of the fabrication process for the target substrate of a graphene-PMMA resonator: (a) SiO_2 deposited, (b) Al sputtered and patterned, (c) SiO_2/Si etched and cavity created.

6.2.2 Transfer of graphene-PMMA films

Multilayer graphene and thin-films of PMMA polymer have been used to prepare a bilayer membrane structure. [Figure 6.2](#) shows a schematic diagram of the transfer process of a thin-film of graphene-PMMA to the target substrate. A multilayer (~ 2.5 nm) graphene film synthesised on copper foil by chemical vapour deposition (CVD) has been used in our resonators. To support the graphene sheet during and after the transfer, a layer of PMMA (molecular weight ~ 996000 with a concentration of 4% in chlorobenzene) with thicknesses of 350, 400, and 500nm has been spin coated on the graphene/copper and annealed at 80 °C for 5 minutes ([Figure 6.2a](#)). The thickness of 8 layers graphene has been determined by Raman spectroscopy, while the thickness of PMMA has been measured with spectroscopic reflectometry. The sample has been left for 24 hours to dry fully in a cleanroom environment. Next, a copper etchant solution of ferric chloride (FeCl_3) has been used to etch the copper foil ([Figure 6.2b](#)). After being cleaned by rinsing in deionised water (DIW) many times, the floating graphene-PMMA film has been scooped and transferred to

the pre-patterned SiO_2/Si substrate.

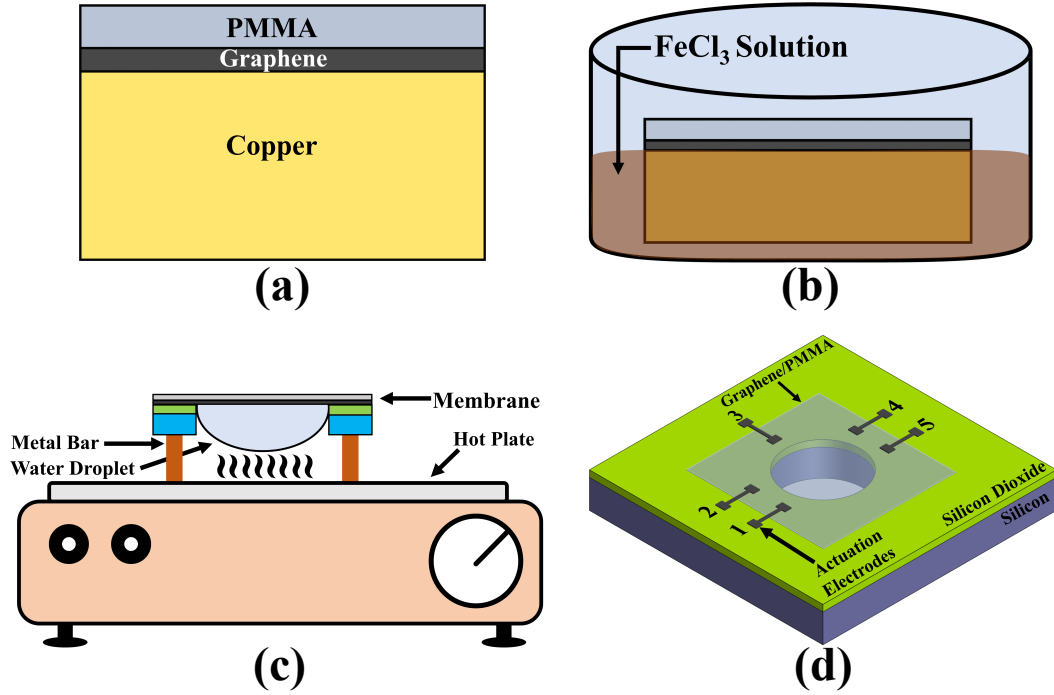


Figure 6.2: Schematic illustration of the transfer process of graphene-PMMA thin-films on a substrate with 3.5 mm-diameter circular cavities. (a) PMMA spin coated on graphene/copper. (b) Copper foil etched in FeCl_3 . (c) Water evaporated from transferred membrane. (d) Final structure of graphene-PMMA resonator.

Since the transferred membrane is suspended over an open cavity, a water droplet will be trapped in the cavity, and due to capillary effects, this may cause a rupture of the transferred membrane. Here, a simple and effective technique has been used that can tackle such stiction-related failures. For this step, two bars with an appropriate height (e.g. 30 mm) are placed securely on a hotplate at 80 °C. Then, the entire stack of graphene-PMMA-substrate was placed on the metal bars creating a bridge-like structure (Figure 6.2c). In this case, the stack will not be in direct contact with the hotplate, and instead the heating that comes from the hotplate will dry the sample slowly until the water liquid is evaporated completely. After this step, the samples have been transferred to another hotplate and annealed at 140 °C for 10 – 20 seconds to stretch the suspended

membrane over the cavity (Figure 6.2d).

6.2.3 Post-transfer characterisation

As shown in the optical images in Figure 6.3, the demonstrated technique has been found to result in a feasible production of ultra-large and graphene-based membranes without causing a rupture of the entire membrane or burning the PMMA supporting layer. More than 75% of the transferred membrane have not exhibited mechanical deformation in the upward or downward direction. In addition, the aspect ratio of the membrane area to thickness is $\sim 10,000$.

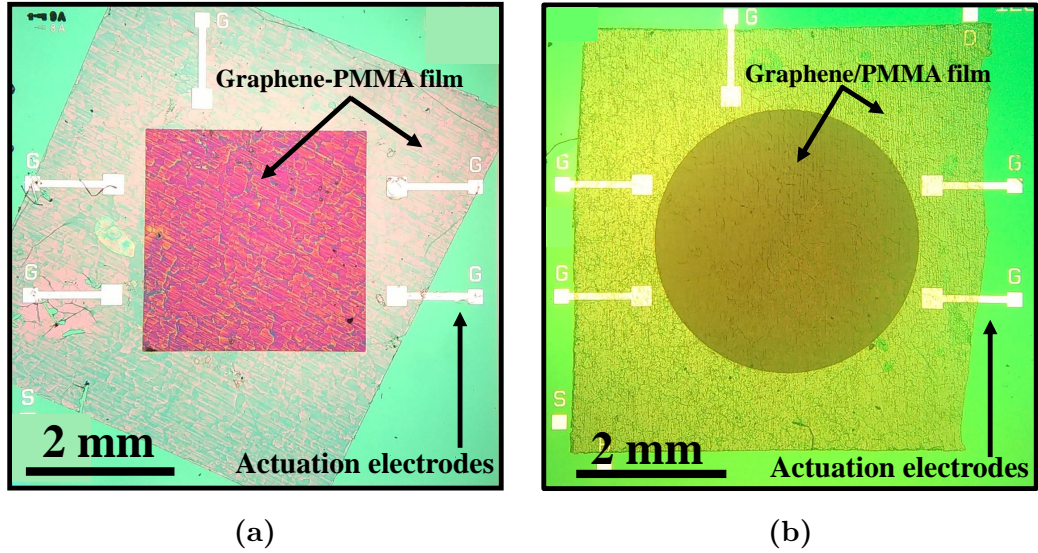


Figure 6.3: Optical micrographs of graphene-PMMA thin-film suspended over square (a) and circular (b) cavities.

6.3 Dynamics of graphene-PMMA resonators

As described in Chapter 2, electrothermal actuation of a bilayer system relies on the difference in the coefficient of thermal expansion for the different materials used. Since the resonator structure fabricated here is a bilayer system, the dynamic behaviour

of the bilayer structure of graphene-PMMA thin-films will be characterised using electrothermal actuation. The effect of actuation configuration, actuation voltage, membrane tension and thin-film thickness on the resonant frequency and the amplitude of vibration will be investigated comprehensively. The reason behind designing the resonators with different actuation electrodes is that the path of the current that passes through the membrane is expected to have a significant influence on the frequency response of the membrane. This means that the resonant frequency and vibration amplitude obtained from one actuation electrode could be different from other configurations even though the actuated membrane is the same. In addition, the use of actuation voltages of 1 - 9 V is because of the fact that the developed resonators are designed in such a manner that they can operate at relatively small actuation/tuning voltages. Such features are highly desirable for low-power consumption audio devices.

6.3.1 Measurements setup

The graphene-PMMA thin films have been actuated electrothermally by applying an input AC voltage superimposed on a DC bias voltage to the actuation metal electrodes underneath the thin film. When the actuation voltage is applied between any two metal electrodes, as shown in [Figure 6.3](#), current will flow through the bilayer structure, hence heat is generated. A local increase of temperature from Joule heating will induce a physical expansion, which in turn alters the mechanical stiffness of the bilayer structure and forces the entire structure to expand or contract accordingly. In this way, the bilayer structure of graphene-PMMA films are driven into resonance. The dynamic vibration of the thin-films has been detected optically using a laser Doppler vibrometer (LDV). The

measurements have been performed at atmospheric pressure and room temperature conditions. For all measurements, an excitation signal has been swept through the frequency range of interest (10 Hz – 30 kHz) and a discrete Fourier transform (FFT) has been used to locate the first three modal frequencies of the suspended films. To measure the amplitude of the vibration, a sinusoidal signal has been applied at the resonant frequency modes.

6.3.2 Effect of actuation configuration

The purpose of using multi actuation electrodes with different configurations to drive the bilayer films is to examine the influence of electrode configuration on the resonant frequency and the amplitude of vibration. In electrothermal actuation, it is possible that the different driving configurations might generate different magnitudes of heat in the sample. To examine the influence of driving configuration on the dynamic behaviour of the graphene-PMMA thin-films, a combined actuation voltage of AC ($V_{ac} = 1$ V) and DC ($V_{dc} = 8$ V) has been applied between two fixed metal electrodes according to the following configurations V_{2-4} , V_{2-5} , V_{3-5} , V_{3-4} , V_{4-5} . Each configuration denotes two actuation electrodes labelled with the numbers shown in [Figure 6.2d](#). The dynamic response of 350-nm-thick circular and square films to different biasing configurations is shown in [Figure 6.4](#) and [Figure 6.5](#). We have found that the configuration of the actuation has a significant impact on the vibration amplitude and frequency shift of the thin-films.

For circular thin-films, the configuration V_{2-4} has shown the largest amplitude of vibration for the first, second and third resonant frequencies compared to the other configurations ([Figure 6.4a](#)). The lowest amplitude of vibration has been observed in the configuration V_{4-5} , especially for the first and third observed

modes.

For square thin-films, on the other hand, the configuration V_{2-5} has been found to exhibit the largest amplitude of vibration for the first and third resonant modes, see [Figure 6.5a](#). The vibration amplitude observed in the configuration V_{2-4} is slightly smaller than that of the configuration V_{2-5} . The configuration V_{4-5} has also led to the lowest vibration amplitude for the first and third resonant modes in the square film.

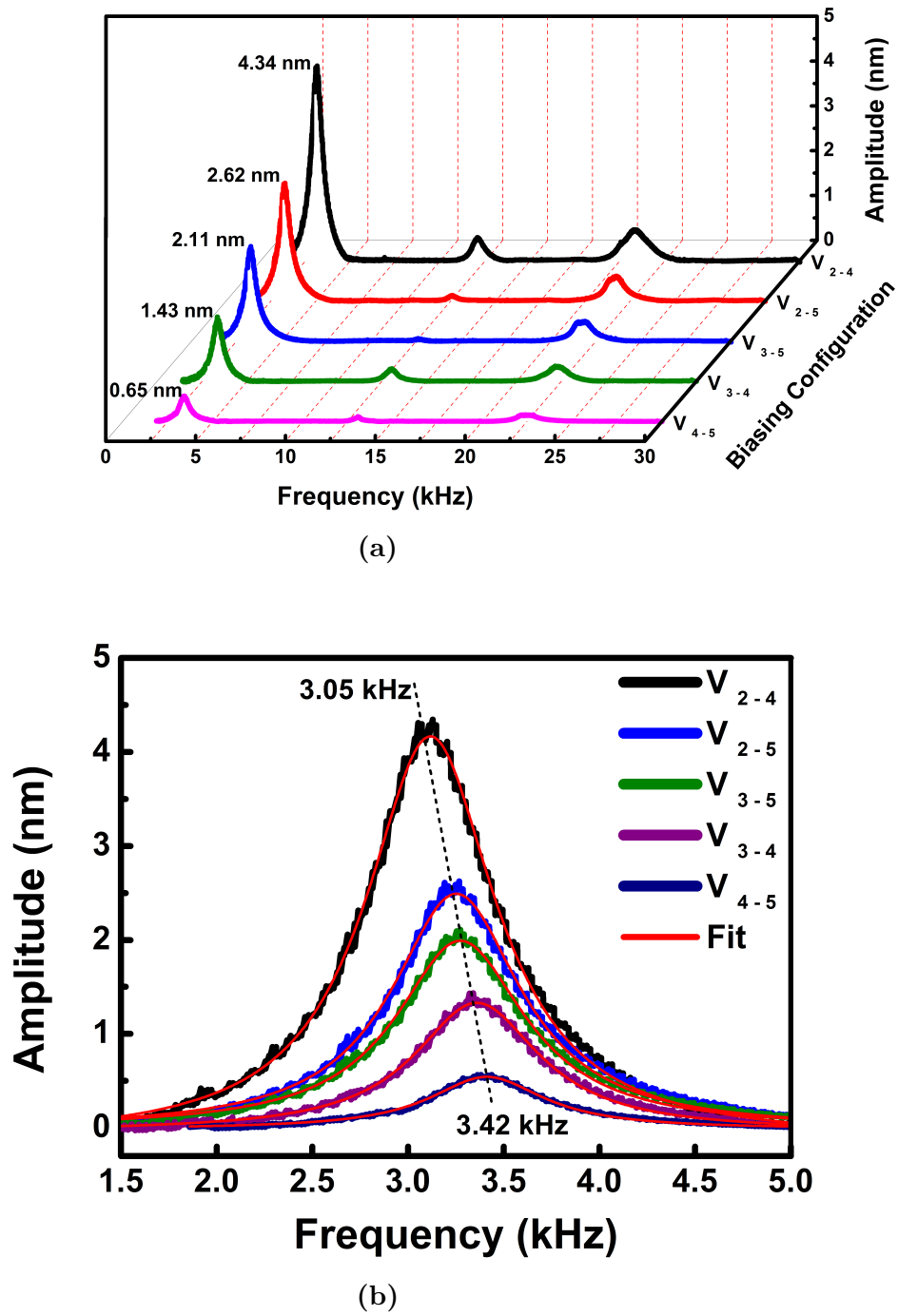


Figure 6.4: The frequency response of 350-nm-thick films of graphene-PMMA to different actuation configurations. (a) Full spectra of circular films. (b) First resonant frequency spectra of circular films.

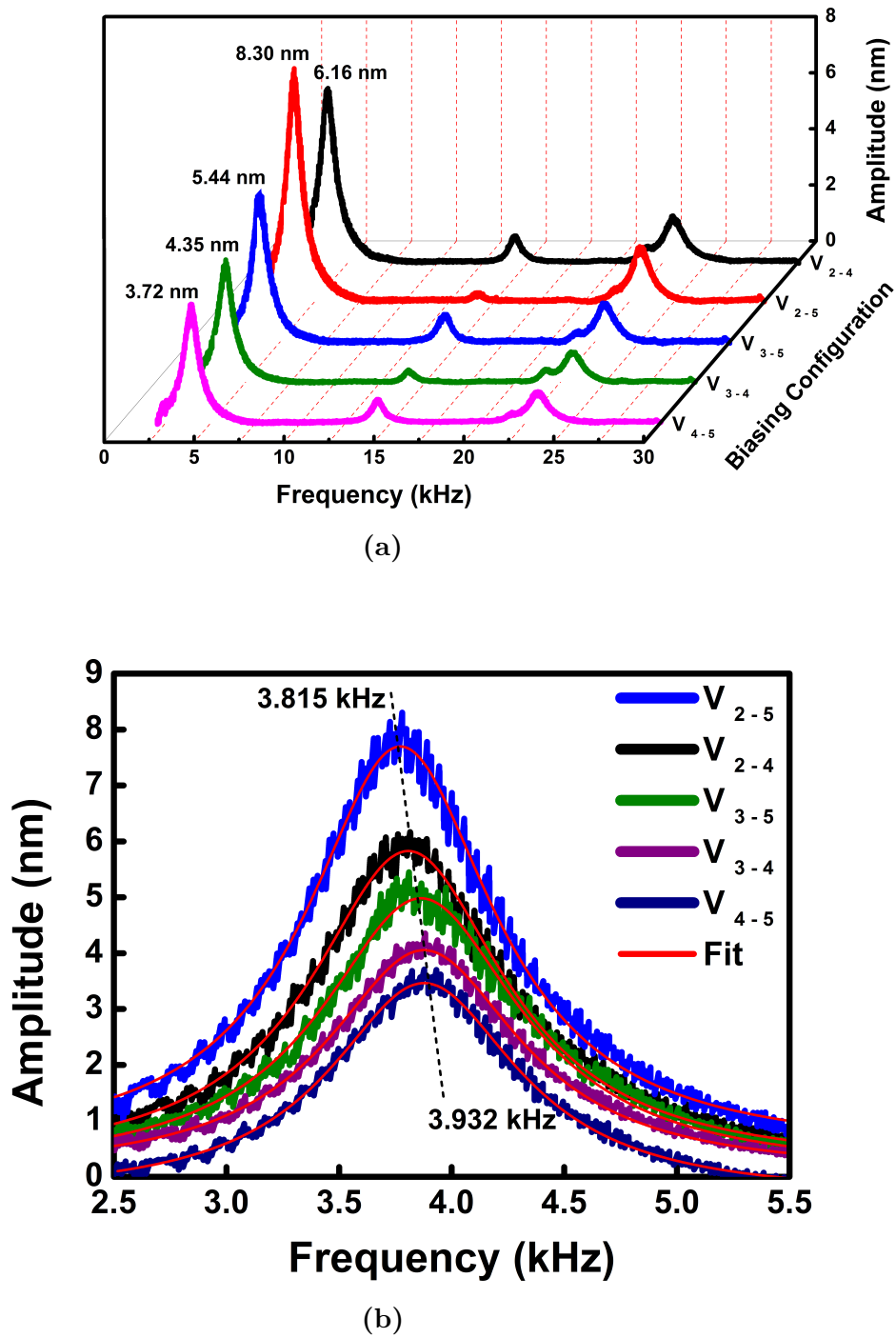


Figure 6.5: The frequency response of 350-nm-thick films of graphene-PMMA to different actuation configurations. (a) Full spectra of square films. (b) First resonant frequency spectra of square films.

Such observation suggests that the generated heat is possibly different for each configuration. It is believed that the path of the current that passes through the active area of the suspended film

could influence the generated heat. At the first resonant frequency, for example, the amplitude of vibration of the circular film using the shorter path configuration V_{4-5} has been found to be 0.65 nm, which is six times less than the highest amplitude of 4.34 nm using the configuration V_{2-4} . The amplitude of vibration of the square film has been observed to be at least two times greater than that of the circular film.

In addition to the change in the amplitude of vibration, the actuation configuration measurements have shown a shift in the films' resonant frequencies when the driving configuration changes, as shown in the zoom-in view of the first resonant modes of the circular ([Figure 6.4b](#)) and square ([Figure 6.5b](#)) films. It can be seen that a gradual increase in the vibration amplitude, for given driving configurations, is accompanied by a gradual decrease of the fundamental resonant frequency of the circular film from 3.42 kHz to 3.05 kHz (i.e. a downward shift of -108187 ppm). The square film, on the other hand, has shown smaller shift in the fundamental resonant frequency compared to the circular film. That is, a shift of -29755.84 ppm from 3.932 kHz to 3.815 kHz has been observed, corresponding to the configurations V_{4-5} and V_{2-5} , respectively. This observation is suggestive of the fact that depending on the degree of heat generated, a certain electrode configuration can cause both a progressively higher amplitude and a larger frequency shift to lower frequencies, consistent with the existence of thermally induced tension in the thin-film.

At the second resonant mode of the circular film, however, it has been found that the configurations V_{2-4} and V_{3-4} have produced larger amplitudes of vibration than the configurations V_{2-5} , V_{3-5} and V_{4-5} . The same behaviour has been observed in the square film, especially in the configuration V_{2-5} . The reason behind such

behaviour is believed to be attributed to the path of electric current through the nodal points of resonant modes. To investigate further the relationship between the mode nodal points and frequency response, the shapes of the measured modes have been extracted from LDV measurements data and illustrated in [Figure 6.6](#).

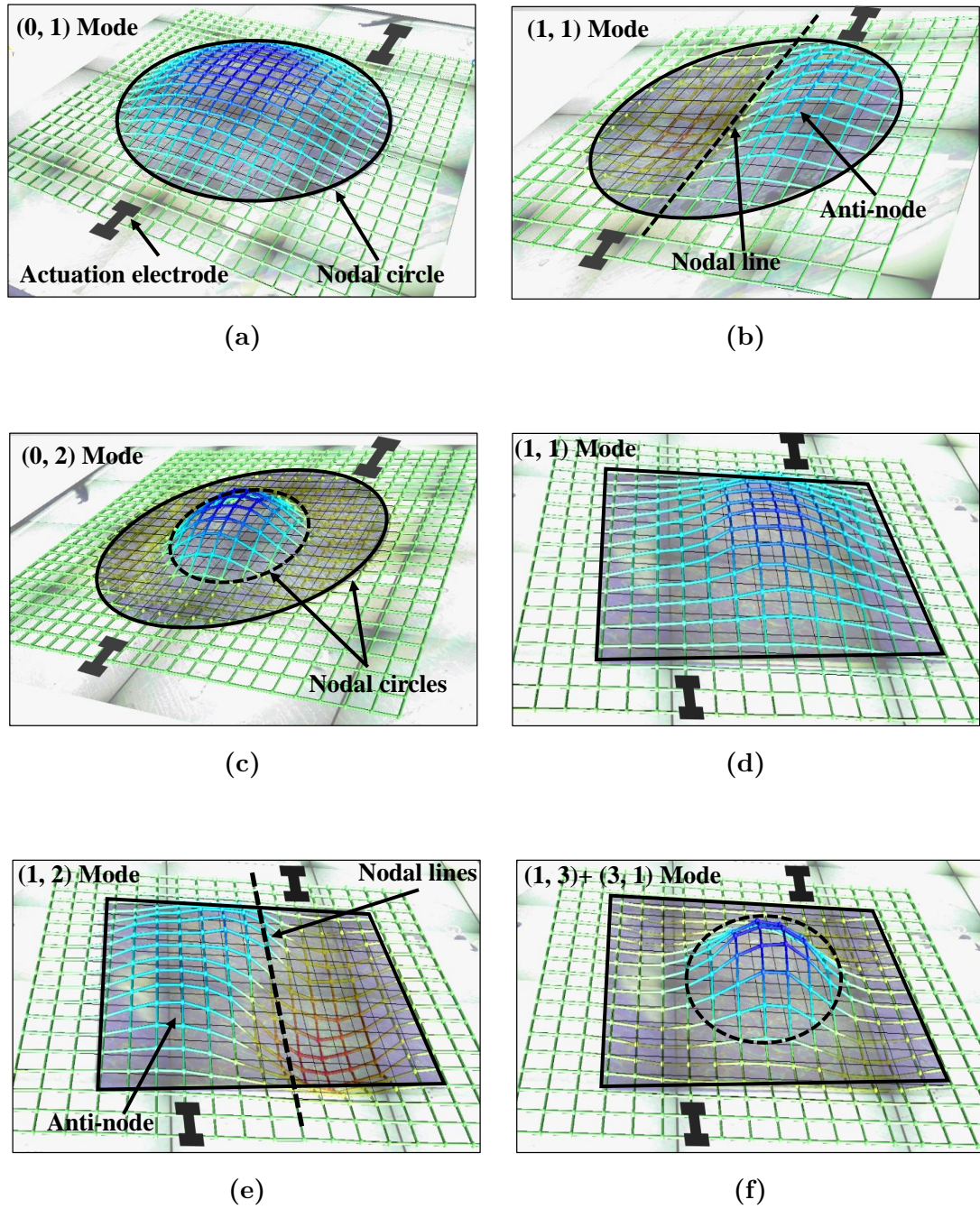


Figure 6.6: Shapes of the first three resonant modes with the nodal and anti-nodal points for circular (a, b, c) and square (d, e, f) thin-films of graphene-PMMA measured by an LDV.

The second mode (1, 1) has anti-nodal points (maximum displacement) and nodal points (zero displacement). In the circular film, the nodal points are one diametric node and one

concentric node (see [Figure 6.6b](#)). The square film has also two nodal lines; one symmetrical node (i.e. the outside square edge) and one asymmetrical node that separates the anti-nodal points ([Figure 6.6d](#)). In the V_{2-4} and V_{3-4} configurations, it is likely that the electrical current is flowing in the path of the anti-nodal points and is able to heat around the anti-nodal area more, thus inducing a larger amplitude of vibration. In the V_{2-5} , V_{3-5} and V_{4-5} configurations, on the other hand, it is believed that the current might flow in the path of the immovable nodal lines, and hence the resultant amplitude of vibration will be smaller.

From these observations, it is concluded that the best actuation configuration is the one at which the current flows through the anti-nodal area of the thin-film. Therefore, the design of the actuation electrodes can be further optimised. For example, two large electrodes with arch-like shape could be considered an optimum design that might provide an efficient actuation configuration for circular films. In general, the resonant frequency and the vibration amplitude of the graphene-PMMA thin-films can be tuned by driving the films with a certain biasing configuration.

6.3.3 Effect of film thickness

Thickness is a property that plays an important role in determining the frequency range of a vibrating structure. Since we are dealing with ultra-large and thin bilayer structures of graphene and PMMA films, the resonator can possibly behave as a membrane or as a plate. Therefore, we have measured the first three modes of resonance for circular and square thin films as a function of film thickness using electrothermal actuation voltages of 1 V of V_{ac} and 8 V of V_{dc} . The measured resonant frequencies versus the film thickness are shown

in [Figure 6.7](#).

The three resonant modes observed for circular and square films are $(0, 1)$, $(1, 1)$ and $(0, 2)$. It can be seen that the resonant frequency of the thin films increases linearly with the film thickness. For example, the first three resonant frequencies of 350-nm-thick circular films of graphene-PMMA have been found to be 3.26, 12.56, and 21.70 kHz respectively. For thick circular films (500 nm), a modest increase of the corresponding modal resonant frequencies to 4.64, 16.75, and 26.68 kHz has been observed. Compared to the circular films, the resonant frequencies of square films have been observed to be slightly larger. For instance, a fundamental resonant frequency of ~ 4 kHz has been measured for 400-nm-thick square film, which is slightly larger than that of ~ 3.7 kHz for circular film. Analytically, the fundamental frequencies of 500-nm-thick circular ([Equation \(2.14\)](#)) and square ([Equation \(2.15\)](#)) membranes of graphene-PMMA under a tension of 0.2 N/m have been estimated to be 4.25 kHz and 4.58 kHz, respectively. The calculated frequencies are consistent with measured ones where the resonant frequency of square films is found to be slightly larger than that of circular ones, as shown in [Figure 6.7](#).

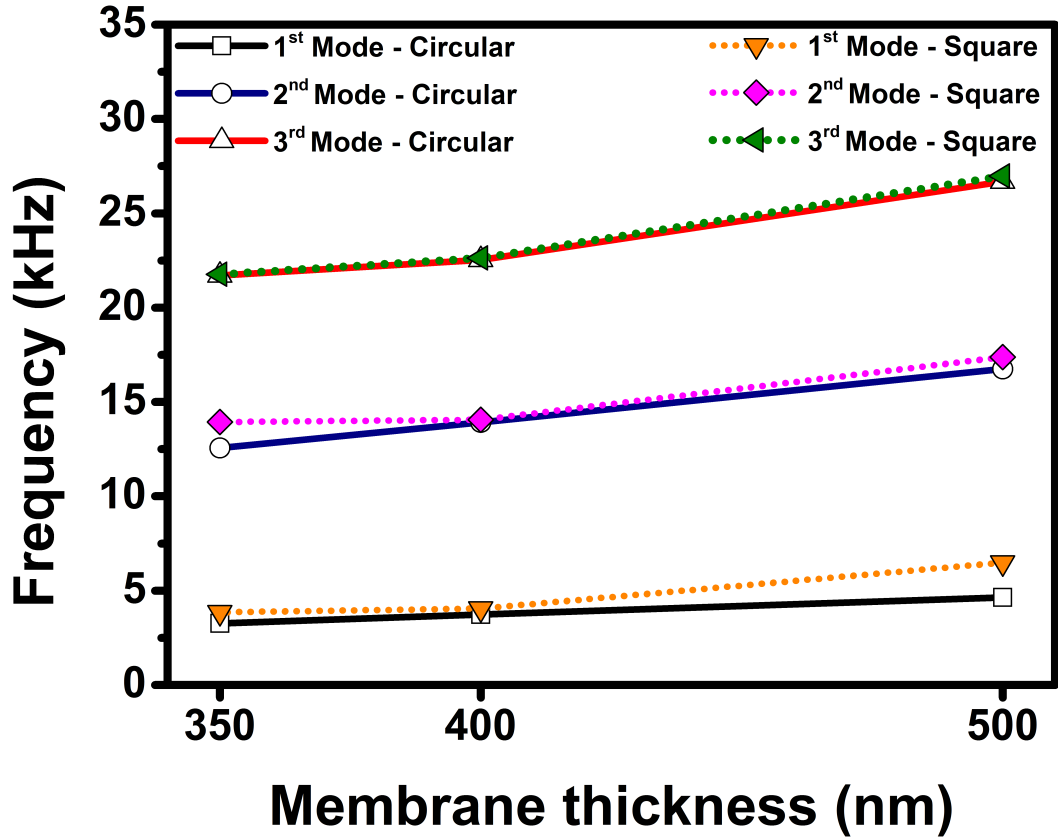


Figure 6.7: Measured modal resonant frequencies of circular (solid) and square (dotted) thin-films with respect to the film thickness. Lines act as guides.

6.3.4 Analysis of membrane and plate

The possibility that the devices reported here will behave either as membranes or as plates will be discussed from frequency and tension/strain points of view. The existing membrane models that describe the frequency of monolayer or multilayer graphene thin films [62, 68, 158–160] could be used to model a bilayer system of graphene and PMMA.

The resonant frequency equations of membranes and plates provided in Chapter 2 describe a single layer of material. Since the thin-films used here are composed of two different materials, it is practically more convenient to use the effective values of parameters. Therefore, the effective values of Young's modulus E_{eff} , thickness

t_{eff} , density ρ_{eff} and bending rigidity D_{eff} parameters for graphene (g) and PMMA (p) films have been given as [161]:

$$E_{eff} = \frac{E_g t_g + E_p t_p}{t_g + t_p} \quad (6.1)$$

$$t_{eff} = t_g + t_p \quad (6.2)$$

$$\rho_{eff} = \frac{\rho_g t_g + \rho_p t_p}{t_g + t_p} \quad (6.3)$$

$$D_{eff} = \frac{\hat{E}_g ((t_g - K)^3 + K^3)}{3} + \frac{\hat{E}_p ((t_p + t_g - K)^3 - (t_g - K)^3)}{3} \quad (6.4)$$

where

$$\hat{E}_g = \frac{E_g}{(1 - \nu_g^2)} \quad (6.5)$$

$$\hat{E}_p = \frac{E_p}{(1 - \nu_p^2)} \quad (6.6)$$

$$K = \frac{\hat{E}_g t_g^2 + \hat{E}_p ((t_g + t_p)^2 - t_g^2)}{2(\hat{E}_g t_g + \hat{E}_p t_p)} \quad (6.7)$$

In addition to the pre-tension (N_i) that can be considered as a built-in tension at room temperature, a thermal tension (N_t) can be induced in the thin-films from Joule heating during electrothermal actuation. Furthermore, the surrounding medium of the measurement has an impact on the dynamic response of the vibrating thin-films. When dynamic frequency measurements are performed in an air medium, the damping effect will add an additional mass (A_m) to the moving mass of the film. The additional mass term can be described by adopting Yu Zhou et al. model [162] as follows:

$$A_m = \frac{2}{3} \frac{\rho_{air}}{\rho_{eff}} \frac{R}{t_{eff}} \quad (6.8)$$

Here, R is used for circular films, while it is substituted with a for square films.

Therefore, by considering the built-in tension as well as the thermally induced tension, the resonant frequencies of clamped bilayer circular and square membranes can be re-written from Equation (2.14) and Equation (2.15) as follows:

$$f_{mn}(\text{circular membrane}) = \frac{\alpha_{mn}}{2\pi R} \sqrt{\frac{N_i + N_t}{\rho_{eff} t_{eff} (1 + A_m)}} \quad (6.9)$$

$$f_{mn}(\text{square membrane}) = \frac{\alpha_{mn}}{2\pi a} \sqrt{\frac{N_i + N_t}{\rho_{eff} t_{eff} (1 + A_m)}} \quad (6.10)$$

In the case of plates, a thermally-induced stress (σ_t) term is used instead of tension. Consequently, the resonant frequencies of clamped bilayer circular and square plates can be re-written from

Equation (2.16) and Equation (2.17) as:

$$f_{mn}(\text{circular plate}) = \frac{\beta_{mn}}{2\pi R^2} \sqrt{\frac{D_{eff} + \sigma_0 t_{eff}}{\rho_{eff} t_{eff} (1 + A_m)}} \quad (6.11)$$

$$f_{mn}(\text{square plate}) = \frac{\beta_{mn}}{2\pi a^2} \sqrt{\frac{D_{eff} + \sigma_0 t_{eff}}{\rho_{eff} t_{eff} (1 + A_m)}} \quad (6.12)$$

Note that the investigation of membrane- or plate-like behaviour of bilayer structures will be limited to the circular films only, as similar behaviour can be assumed for square films. If it is assumed that the bilayer structures, despite their thicknesses, have the same magnitude of tension, their resonant frequencies should decrease with the increase of the thickness. However, the measurements in Figure 6.7 have shown that the resonant frequency increases with the increase of the film thickness. It is possible that such behaviour could be attributed to the differences of tension in the membranes. As the membrane tension increases, the resonant frequency increases. Therefore, different values of total tension ($N_i + N_t$) have been used in the membrane model (Equation (6.9)) to find the values of tension at which the experimental resonant frequency fits with the analytical model. The calculations are presented in Table 6.1. The strain has been calculated based on the estimated values of tension. The physical properties of Young's modulus and density used in the calculations are respectively 1 TPa and 2270 kg/m³ for graphene and 3.8 GPa and 1045 kg/m³ for PMMA.

Table 6.1: Estimation of the magnitude of total tension ($N_i + N_t$) and strain in the graphene-PMMA films with different thicknesses based on the experimental measurements and analytical description in Equation (6.9) for the first resonant frequency ($f_{0,1}$).

Film thickness	Analytical			Experimental
	N (N/m)	Strain	$f_{0,1}$ (kHz)	$f_{0,1}$ (kHz)
8 layers/ 350 nm	0.801	1.96×10^{-4}	3.26	3.26
8 layers/ 400 nm	1.078	2.52×10^{-4}	3.73	3.73
8 layers/ 500 nm	2.079	4.46×10^{-4}	4.64	4.64

If the transferred films are assumed to behave as plates, the calculated resonant frequencies from the stress-free plate model (i.e. $\sigma_t = 0$) are not in agreement with the measurements, as presented in Table 6.2. When the thermal induced stress is included in the plate model (Equation (6.11)), the experimental resonant frequency fits with the model at only extremely high values of stress (e.g. 135.53 GPa for 350 nm-thick film). Such a high thermal stress seems unlikely to be induced practically at an electrothermal actuation voltage of 8 V. Therefore, it is concluded that the bilayer film reported here is more likely to behave as a membrane structure rather than a conventional plate.

Table 6.2: Estimation of the magnitude of thermally induced stress and strain in the graphene-PMMA films with different thicknesses based on the experimental measurements and analytical description in Equation (6.11) for the first resonant frequency ($f_{0,1}$).

Film thickness	Analytical			Experimental
	Stress (GPa)	Strain	$f_{0,1}$ (kHz)	$f_{0,1}$ (kHz)
8 layers/ 350 nm	0	0	0.09	3.26
8 layers/ 400 nm	0	0	0.07	3.73
8 layers/ 500 nm	0	0	0.06	4.64
8 layers/ 350 nm	135.53	11.68	3.26	3.26
8 layers/ 400 nm	182.57	17.18	3.73	3.73
8 layers/ 500 nm	298.43	32.19	4.64	4.64

6.4 Tuning of graphene-PMMA resonators

The alteration of the mechanical stiffness of graphene results in the tuning of its resonant frequencies. Frequency tuning is of great interest to certain areas of sensing and communications applications such as terahertz modulators [163, 164], plasmonic filters [163], frequency mixers [155], and self-sustained oscillators [156]. However, the frequency tuning feature of resonators can be influenced significantly by the background noise. The effect of noise becomes significant as the device size becomes smaller. In addition, resonators based on micro- and nanostructures are more susceptible to nonlinear dynamic behaviour [156]. The noise and nonlinearity effects might limit the linear dynamic range which results in a small motional amplitude and poor frequency tunability. In the previous sections, it has been shown that the bilayer membrane of graphene-PMMA could be driven into resonance using electrothermal actuation. In the following sections, it will be shown that electrothermal transduction can be used to tune the resonant

frequencies of the bilayer membranes and increase their vibration amplitude using relatively small tuning voltages.

For all dynamic tuning measurements provided here, a new set of large multilayer graphene membranes of thickness of ~ 2.5 nm supported by a thin film of ~ 370 nm of PMMA have been realised experimentally using the same transfer process mentioned in the previous sections. The bilayer membranes have been transferred onto circular cavities with a diameter of 3.5 mm and square cavities with a side length of 3 mm. The dynamic tuning of the fabricated resonators has been investigated electrothermally by applying a combination of AC and DC voltages between the tuning electrodes labelled 2 and 5 in [Figure 6.2d](#). It is expected in such a scenario that the electrical current will flow through the centre area of the suspended membrane, targeting the anti-nodal points of the fundamental resonant mode and consequently maximizing the vibration amplitude. Under atmospheric pressure and room temperature conditions, the dynamic vibration of the membranes has been detected optically using the LDV. Note that the measurements have been limited here to the first resonant frequency only. To do so, an excitation signal has been swept through the frequency range of interest while applying a discrete Fourier transform (FFT) to the signal.

6.4.1 Frequency tuning: circular and square membranes

The electrothermal tuning has been performed for both circular and square resonators. First, the AC voltage has been kept constant at an amplitude of 1 V while sweeping the DC tuning voltage from 1 to 9 V. Second, the DC voltage has been held at 1 V while varying the AC voltage from 1 to 9 V. The measured frequency response of the membranes to the applied voltages is shown in [Figure 6.8](#). It can be observed clearly from the entire frequency spectra measurements that the increase of the applied voltage (DC or AC) leads to a

downward shift of the first resonant frequency accompanied by an increase of the amplitude of vibration. The measured response reveals the dependency of frequency tuning on the tuning voltage. In general, the resonant frequency of circular and square membranes has been found to shift downward maximally by $\sim 9\%$ and $\sim 5\%$ with respect to a DC tuning voltage of 9 V and an AC voltage of 1 V. On the other hand, the overall shift in the resonant frequency when an AC voltage of 1 - 9 V and a DC voltage of 1 V are applied has been observed to be smaller than that of DC tuning.

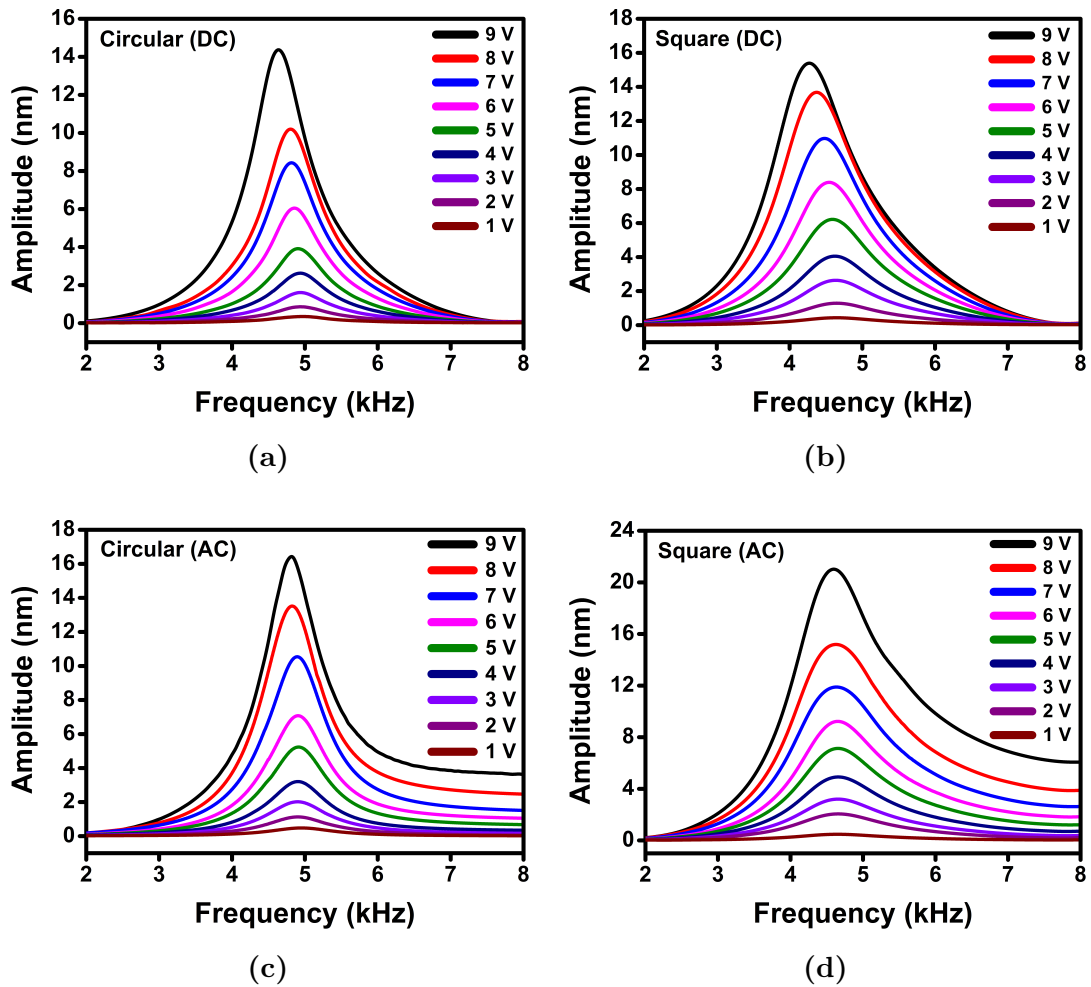


Figure 6.8: Measurement of the amplitude of vibration versus resonant frequency shift for circular and square membranes with respect to the applied voltage. (a, b) Frequency response measured at a constant AC voltage of 1 V and a DC tuning voltage (1 to 9 V). (c, d) Frequency response measured at a DC voltage fixed at 1 V and an AC voltage (1 to 9 V).

Overall, with the application of electrothermal DC tuning voltages of 1 – 9 V while fixing the AC voltage at 1 V, the frequency response curves of both circular and square membranes have been found to be symmetric as shown in [Figure 6.8a](#) and [Figure 6.8b](#). However, when the electrothermal actuation is performed under a fixed DC voltage of 1 V while varying the AC voltage from 1 to 9 V, the resultant resonance curves are asymmetric ([Figure 6.8c](#) and [Figure 6.8d](#)). Such asymmetrical behaviour could be related to the alternating nature of the AC driving signal, especially at higher AC voltages.

The actual amplitude of vibration has been measured experimentally by applying a sinusoidal excitation signal at the observed resonant frequency. The measurements of the vibration amplitude of circular and square membranes as a function of the applied voltage is shown in [Figure 6.9](#). It can be seen clearly that the amplitude of vibration changes according to the applied voltage amplitude.

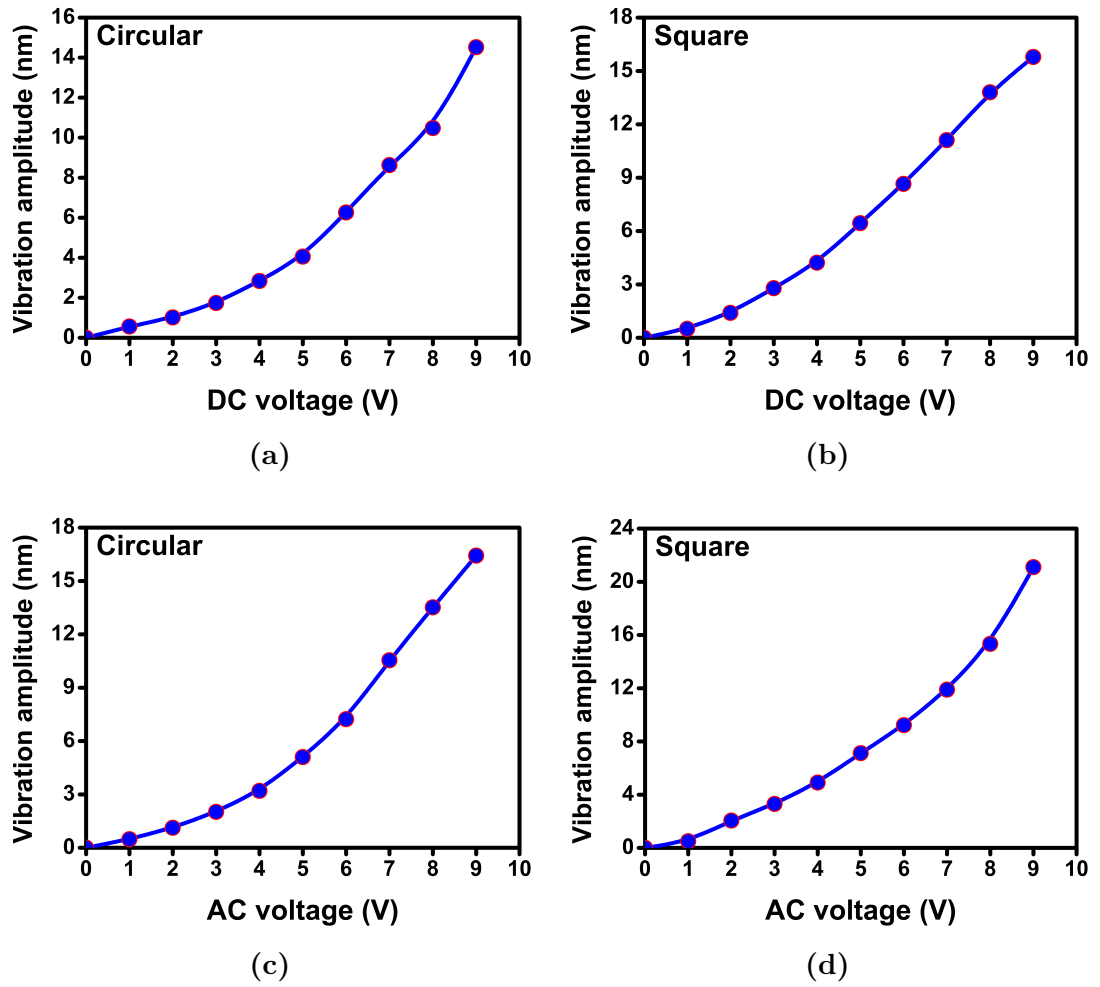


Figure 6.9: Measurement of the vibration amplitude of circular and square membranes with respect to the applied DC (a, b) and AC (c, d) voltages of 1 to 9 V. Note that the measured values of vibration amplitude have been extracted from the highest points of resonance peaks with frequency resolution of 1.56 Hz.

Overall, non-linear response has been observed in the increase of the vibration amplitude with respect to the applied voltage. However, two observations of the vibration amplitude can be distinguished in two ranges of the applied voltage; the first range is from 1 to 5 V and the second range is from 5 to 9 V. The voltage sensitivity has been found to be greater by more than two times in the second range than that in the first one. For example, a circular membrane has exhibit a voltage sensitivity of 0.8 nm/V and 2.5 nm/V in the first and second ranges of the applied DC voltage, respectively.

In case of the circular membranes, it has been found that increasing the DC tuning voltage in the first range of 1 – 5 V leads to a vibration amplitude response of ~ 0.8 nm/V, see [Figure 6.9a](#). In the second range of 5 – 9 V, however, the vibration amplitude response has been found to be about three times greater than in the first range. At a DC tuning voltage of 9 V, an amplitude of vibration of ~ 15 nm has been observed. For frequency tuning under different AC voltages, similar behaviour to the DC case has been observed ([Figure 6.9c](#)). The amplitude of vibration is observed to be greater by three times in the second range of the applied AC voltage than that in the first range. A maximum vibration amplitude of ~ 17 nm has been measured at a DC tuning voltage of 9 V. Therefore, it is deduced that the circular membranes exhibit higher vibration amplitude in the second range of 5 – 9 V of the applied voltage. In addition, by considering the overall trend of the observed response from the first to the second range, the applied AC voltage seems to be more influential in this regard.

In case of the square membranes, a vibration amplitude response of ~ 1.28 nm/V has been achieved in the first range of the DC tuning voltage ([Figure 6.9b](#)). Comparatively, the application of the

DC tuning in the second range would make the square membranes exhibit a vibration amplitude response of 2.4 nm/V. When different AC voltages are applied (Figure 6.9d), the observed behaviour is almost similar to the DC tuning case, as the second range of the applied AC voltage results in an increase of the vibration amplitude response to ~ 3.4 nm/V compared with ~ 1.3 nm/V in the first range. A maximum amplitude of vibration of ~ 16 nm has been observed with a DC voltage of 9 V compared to ~ 22 nm with an AC voltage of 9 V. Therefore, it can be concluded that the performance of the electrothermal tuning of the square membranes shows relatively larger vibration amplitude in the second range for both DC and AC applied voltages. The linear response of resonant frequencies with respect to the DC and AC voltages at different ranges (i.e 1 - 5 V and 5 - 9 V) will be discussed in more detail in the tuning sensitivity section.

6.4.2 Tuning sensitivity

To evaluate the efficiency of the electrothermal tuning used in this work, the tuning sensitivity of the bilayer membranes has been estimated based on the experimental data obtained from frequency response measurements. From the linear fitting of the tuned resonant frequency (f), the tuning sensitivity ($\Delta f/\Delta V$) has been estimated for circular and square membranes and is shown in Figure 6.10.

Overall, a significant influence of the amplitude of the applied voltage on the frequency tuning response has been observed for both circular and square membranes. Similar to the amplitude of vibration observations, the bilayer membranes exhibit two different ranges of tuning sensitivity, corresponding to the 1 – 5 V and 5 – 9 V ranges of the applied voltage. In general, the tuning sensitivity

is observed to be higher in the second range compared to the first range.

For the circular membranes, the tuning sensitivity has been found to be greater by about two times (i.e. 37 Hz/V) in the second range of 5 – 9 V of the DC tuning voltage than that (i.e. 18 Hz/V) in the first range of 1 – 5 V (Figure 6.10a). In the case of tuning under different AC voltages (Figure 6.10c), the membrane tuning sensitivity has been increased from 10 Hz/V in the first range to 34 Hz/V in the second range. It is concluded that the circular membranes exhibit better tuning sensitivity in the second range of the applied voltage.

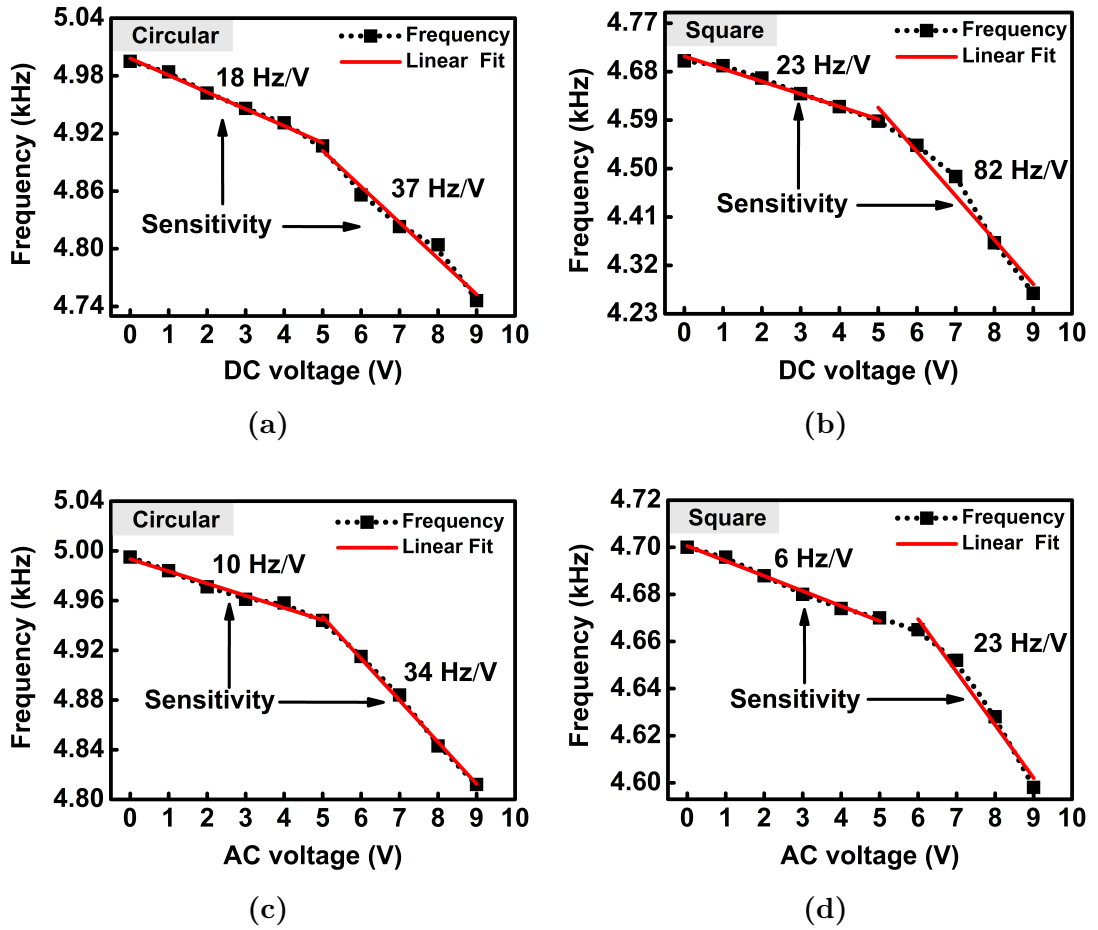


Figure 6.10: Tuning sensitivity of circular and square membranes of graphene-PMMA estimated from frequency shift with respect to the applied DC (a, b) and AC (c, d) voltages of 1 to 9 V. The measured values of resonant frequencies have been extracted from the highest points of resonance curves with frequency resolution of 1.56 Hz.

For the square membranes, performing the frequency tuning in the first range of the DC voltage has led to a tuning sensitivity of 23 Hz/V, which has been increased by more than three times (82 Hz/V) in the second range (Figure 6.10b). Moreover, the square membranes seem to exhibit a tuning sensitivity of 6 Hz/V in the first range of the applied AC voltage, compared to 23 Hz/V in the second range (Figure 6.10d). It can be concluded, therefore, that the square membranes possess better tuning sensitivity in the second range of both DC and AC voltages.

From the electrothermal tuning observations accomplished in this

work, it can be concluded that it is more effective to perform the frequency tuning of the graphene-PMMA bilayer membranes under a DC bias voltage rather than an AC voltage. These results are consistent with other studies reported for electrothermally actuated silicon carbide MEMS resonators [165]. From the device design point of view, the square membranes have shown better tuning sensitivity than the circular ones when different DC bias voltages are applied. Although the graphene sheet can achieve an extremely high tunability [157], the relatively small tunability that has been observed in our membranes is possibly because of the fact that the change in tension provided by the polymer supporting layer of PMMA is dominant [156] [166]. In addition, the presence of the PMMA layer, as well as the quality of the contact between metal electrode pads and membrane, might influence the dynamic tuning response of the measured devices. On the other hand, both the circular and square membranes show almost similar behaviour under the application of an AC voltage. It is possible that the different response of circular and square membranes might be related to the differences in their boundary and clamping conditions.

It is believed that the tuning sensitivity of the membrane can be attributed to the thermally-induced tension from the electrothermal actuation/tuning. Any variation in the membrane tension results in a shift of the resonant frequency. The downward frequency shift that has been observed in the bilayer circular and square membranes is highly likely to be consistent with the reduction of thermally induced tension. The source of the reduction of the membrane tension could be attributed to the Joule heating phenomenon. When a voltage is applied to the actuation electrodes, electric current will pass through the whole bilayer membrane and generate heat. The generated heat will cause a temperature gradient (ΔT) within the bilayer structure. Since graphene and PMMA have different

coefficients of thermal expansion, the temperature gradient within the entire membrane thickness will induce a mechanical strain, hence thermal tension in the membrane. When the thermally induced tension is modified, the mechanical stiffness of the bilayer structure will be altered accordingly. In the currently fabricated devices, therefore, the increase of the applied voltage from 1 to 9 V leads to a reduction of the membrane tension and hence a downward shift of the resonant frequency.

6.5 Summary

This chapter has been dedicated to the optimised design, fabrication and dynamic characterisation of electrothermally-driven/tuned large-area resonators based on suspended membranes of graphene-PMMA. The accomplished work and main findings of this chapter are summarised as follows:

A straightforward fabrication process for the fabrication of low frequency electromechanical resonators using a bilayer structure based on graphene-polymer membranes has been developed. Resonators that are made from ultra-large multilayer graphene membranes of thickness of ~ 2.5 nm supported by a thin polymeric film of PMMA have been realised experimentally on a millimetre scale. The bilayer membranes have been transferred onto circular cavities with a diameter of 3.5 mm and square cavities with a side length of 3 mm. The demonstrated graphene-PMMA resonators have striking diameter (side length) to thickness aspect ratios of $\sim 10,000$, which allow the bilayer membranes to vibrate at frequencies within the audio range and achieve a minimum resonant frequency of ~ 4.5 kHz.

The difference in the thermal properties of graphene and PMMA films have enabled the resonant frequencies of the bilayer membranes to be tuned electrothermally. The dynamic tuning of the fabricated resonators has been investigated electrothermally by applying a combination of AC and DC voltages. The applied AC and DC voltages with ranges of 1 – 5 V and 5 – 9 V have revealed a significant impact on the frequency tuning response. With the increase of the applied voltages, a downward shift of the resonant frequencies accompanied by an increase of the vibration amplitude have been observed.

The square membranes have shown better tuning sensitivity

than the circular ones for different DC tuning voltage ranges while both types of membranes exhibit almost similar increases in tuning sensitivity for the different AC tuning voltage ranges. For example, a maximum tunability of $\sim 9\%$ accompanied by tuning sensitivity of 82 Hz/V and vibration amplitude of ~ 22 nm have been observed for the square membranes under electrothermal tuning voltages of 1 V of AC and 9 V of DC. The fabrication technique reported in this work can be applied to realise large suspended membranes made from other 2D materials. Furthermore, the obtained results indicate that the graphene-polymer resonators can achieve low frequency vibration within the audible region (20 Hz – 20 kHz), holding promise for the development of reliable and high sensitivity transducers for a wide range of acoustic and audio applications.

Chapter 7

Conclusions and Scope of Future Work

The work presented in this thesis has focused primarily on the development of electromechanical transducers based on MEMS technology for acoustic sensing applications. The major contributions of this research are mainly aimed at designing and fabricating a range of mechanical resonators that can operate at frequencies within the audible range. From a practical standpoint, the developed resonators can be used in a microphone, hearing aid, speaker or headphone device. The main contributions, key findings and possible future work suggestions of this accomplished research are summarised in this chapter.

7.1 Tantalum-based Resonators

The first resonator that has been developed in this work is based on an array of doubly clamped microbeams made from tantalum metal. The unique physical and chemical properties—high melting point, corrosion-resistance, high fracture toughness and low ratio of Young’s modulus to mass density— of tantalum metal have been the primary motivation for the design and fabrication of tantalum-based resonators. Since the main objective of this project

is to realise mechanical resonators that can vibrate within the audio dynamic range, a proper design that ensures a free-standing structure of doubly clamped microbeams of tantalum is essential. It has been shown that the suspended beams can achieve a resonant frequency within the audible range by either increasing the length or reducing the thickness of the beams. One of the problematic issues facing tantalum microbeams-based resonators, as well as other MEMS-based devices, is the residual stress. The challenge becomes even stronger as the mechanical resonant component of a resonator device becomes longer (or thinner). Therefore, a significant contribution of this research has been aimed at investigating the residual stress that could develop in thin-films or suspended beams of tantalum during the fabrication or post-fabrication processes.

A comprehensive investigation on the relationship between fabrication process parameters and residual stress of tantalum thin-films has been conducted. The findings reveal that the residual stress of 50-nm-thick sputtered films of tantalum shifts between tension and compression state regions, depending on the deposition and post-deposition conditions. In particular, the thin-film residual stress has been evaluated as a function of deposition conditions, annealing treatment temperature, oxygen exposure time, and bombardment exposure parameters. It has been found that residual stress of the thin-films starts as a compressive stress at low sputtering pressures and switches significantly to the tension state as the pressure increases. In addition, it has been shown that the residual stress of films deposited at a lower sputtering pressure becomes more compressive when annealed at 300 °C. When annealed and unannealed thin-films are exposed to atmospheric ambient, the residual stress has been found to remain stable for the former films while it changes significantly for the latter films. Furthermore, the as-deposited thin-films have been

exposed to pure argon energy bombardment and as a result, a high compressive stress has been developed in the films.

Based on the tantalum thin-films stress outcomes, an array of suspended doubly clamped microbeams ($100 - 400 \mu\text{m}$) of tantalum has been fabricated. Compressive and tensile-stressed films have been used as structural elements of the beams, while employing wet and dry etching systems to release the beams and make them suspended freely. The influence of the initial stress of the deposited films and etching release process has been investigated by charactering the final deflection profile of the released structures. The optical characterisation of the static deflection profile has shown that the suspended beams made from compressive-stressed thin films exhibit larger vertical buckling than that made from tensile-stressed films. Finite element models have been developed to verify the experimentally observed behaviour of the released structures. An optimised model has been created to predict accurately the buckling behaviour of the suspended beams by considering the effects of compressive residual stress and an external load applied at different boundary conditions of the beam. An aspect ratio of vertical deflection to the beam length of 1:48 has been achieved for suspended beams made from tensile stressed-films and released in the wet etching process.

Finally, the outcomes of the as-deposited films stress and static deflection profile measurements have been considered for the optimisation of the design and fabrication process of tantalum-based tunable resonators. An array of straight and long suspended microbeams with lengths of $1 - 3.4 \text{ mm}$ has been realised successfully by controlling the fabrication process-induced stress and minimising the static vertical deflection to beam length aspect ratio. The optimised design includes a large bottom actuation electrode that enables the resonator to be driven into resonance and have

its resonant frequency tuned electrostatically. Numerical and analytical models have been created to investigate the effect of beam length and any possible stress that might develop in the resonator material on the resonant frequency. The resonators have achieved a low frequency response of 1.4 kHz, which is within the audible range, and a substantial increase in the vibration amplitude to $\sim 2.5 \mu\text{m}$. Another outstanding feature of the devices realised in this work is that the actuation voltage required for their operation is relatively small (1 – 5 V). Moreover, the resonant frequency of the devices has been tuned within the audio range; hence the frequency selectivity characteristic has been obtained for the developed devices. Therefore, it can be concluded that the proof-of-principle demonstration of the use of tantalum-based resonators for audio applications has been achieved.

7.2 Graphene-based Resonators

In addition to the MEMS-based resonators of tantalum, mechanical resonators based on an atomically-thin membrane of the 2D material of graphene have been developed. The exceptional mechanical properties of graphene have motivated the use of graphene as a structural material for large-area resonators. Besides being one of the thinnest, lightest and strongest materials to be discovered, graphene has a striking stretching capacity of 20 -25 % of its length. Such a high flexibility enables the graphene membrane to bend substantially without sustaining damage or inducing deleterious defects. A major motivation for developing graphene-based resonators for microphone-like devices is that ultra-thin membranes of graphene are extremely sensitive to any applied stimulus, which could result in enhancing the sensitivity and signal-to-noise ratio of the resonator.

The practical use of graphene properties has been demonstrated by developing a simple route to transfer chemically vapour deposited graphene from its metal growth substrate to a substrate of interest. Firstly, shallow cavities with a depth of 2 μm have been employed as target substrates for graphene-based resonators. Wet and dry transfer processes have been used. From fabrication point of view, it has been found that such transfer processes are somewhat destructive, as different forms of deformation such as wrinkling, folding, ridging and cracking have been induced in the transferred films. Despite the fact that the wet-transfer technique is less detrimental to the membrane than the dry-transfer one, stiction-related damage due to solvents used is one of the drawbacks of the wet-transfer process. However, it has been found that the wet-transfer process is relatively more controllable than its dry counterpart; that is, the wet-transferred membranes have been observed to be less deformable than the dry-transferred membranes.

The challenges observed in the shallow cavity devices have been addressed, and an optimised design has been developed. Instead of using shallow cavities, a simple design based on deep cavities (i.e. a depth of 380 μm) has been proposed and verified experimentally. As the entire layer of the silicon substrate has been etched completely, the transferred membranes have been observed to be suspended freely on circular and square cavities without incurring deleterious mechanical deformation or developing upwards or downwards bending. It has been found that the developed process allows millimetre-scale membranes of a graphene sheet and a thin-film of PMMA to be transferred onto circular cavities with a diameter of 3.5 mm and square cavities with a side length of 3 mm. The distinguishable feature of the demonstrated fabrication technique is the ability to produce high yield and non-ruptured suspended membranes with exceptional diameter (side length) to

thickness aspect ratios of $\sim 10,000$. Due to the extremely large-area of the transferred membranes, the graphene-based resonators have achieved successfully resonant frequencies within the audio range. To provide a sufficient mechanical support to the graphene sheet during the transfer process, a thin layer of polymeric films of PMMA has been attached to the graphene membrane. As a result, the final structural element of the fabricated resonators has been realised in a bilayer membrane form.

The optimised design of graphene-based resonators described in this thesis has established clearly the potential use of electrothermal actuation as an effective driving mechanism. One of the gained advantages of building a mechanical resonator from a bilayer structure, in which the two materials have different mechanical and thermal properties, is that such a structure enables the use of electrothermal transduction to drive the resonators into resonance. Therefore, the dynamic behaviour of the circular and square resonators has been investigated electrothermally by driving the bilayer structures with a combination of AC and DC actuation voltages. For such measurements, several actuation electrodes have been implemented to examine the influence of the actuation configuration on the resonant frequency and the amplitude of vibration. The actuation results have revealed that these bilayer structures are more likely to behave as membranes rather than conventional plates, in agreement with analytical membrane and plate models.

The demonstrated devices have shown that, electrothermal actuation can also be used to tune the resonant frequency of the bilayer membranes and increase their amplitude of vibration with a relatively small tuning voltage of 1 – 9 V. Importantly, the tuning characterisation has revealed a significant impact of the range of the applied voltage (i.e. 1 – 5 V or 5 – 9 V) on the frequency tuning

response of the fabricated devices. As the applied tuning voltages increases, a downward shift of the resonant frequency accompanied by an increase of the vibration amplitude have been observed. Although both circular and square membranes have exhibited resonant frequencies within the audio range, the square membranes have shown better tuning sensitivity than the circular ones for different DC tuning voltage ranges. For different AC tuning voltage ranges, both types of membranes have been exhibited almost similar increases in tuning sensitivity. In conclusion, resonators based on ultra-thin, ultra-large, and durable bilayer membranes tunable to audio frequencies (~ 4.5 kHz) have been realised successfully, thus demonstrating the ability of graphene-based resonators to be used in hearing aids and MEMS microphones.

7.3 Scope of future work

There are still many research aspects where the work described here in this thesis can be improved further. Potential future work should be focused on extending the already accomplished research and addressing the main challenges that face the development of reliable mechanical resonators for acoustic sensing applications. Aspects related to the design, materials, fabrication, characterisation and testing could be the subject of further investigation and analysis.

7.3.1 Design of resonant element

In the case of tantalum-based resonators, the optimised fabrication process can be used to fabricate a membrane structure instead of beam-like structures. The doubly clamped beams resonators performed in this work have achieved a certain range of audio frequencies (i.e. < 10 kHz for the fundamental resonant mode). For hearing assistive applications, it is sometimes important to cover the full audible range. It is expected, therefore, that membrane-based transducers of tantalum might be more practical for artificial cochlear implants and other hearing aid devices. The design of the membrane, however, has to be improved and optimised in such a manner that the full spectra of audio frequencies dynamic range is covered. It is also possible to manipulate the length and thickness parameters of the beams-based resonators, so that the tunability range and tuning sensitivity can be improved further. Similar to the design of graphene-based resonators, tantalum-based resonators can be formed into circular and square membranes structures, and hence the resonator can be used as a microphone.

7.3.2 Graphene microphone

For graphene-based resonators, it could be of great importance to reconsider the design of the cavities used in this work. Although the currently-developed design has led to ultra-large and undeformed membranes, the membranes can be only actuated electrothermally. In fact, the resonators can be driven acoustically, but the vibrational signals cannot be processed further according to the developed design. For example, the design does not include bottom sensing electrode, and hence the vibration cannot be sensed capacitively in a similar way to commercial microphones. One possible way to overcome these challenges could be the optimisation of the design

by creating shallow cavities with a depth of a few micrometres. The transfer/fabrication process has to be optimised to ensure that the membrane can be suspended without incurring mechanical bending. Moreover, a piezoelectric layer can be deposited on the membrane surface, thus enabling the actuation of the resonator and sensing its signal piezoelectrically.

Bibliography

- [1] G. E. Moore, “Cramming more components onto integrated circuits,” *Proceedings of the IEEE*, vol. 86, pp. 82–85, Jan 1998.
- [2] International Technology Roadmap for Semiconductors, “<http://www.itrs2.net/>,” 2018.
- [3] J. W. Judy, “Microelectromechanical systems (MEMS): Fabrication, design and applications,” *Smart Materials and Structures*, vol. 10, pp. 1115–1134, Dec 2001.
- [4] T. M. Adams and R. A. Layton, *Introductory MEMS: Fabrication and applications*. Boston, MA: Springer US, 2010.
- [5] H. G. Craighead, “Nanoelectromechanical Systems,” *Science*, vol. 290, pp. 1532–1535, Nov 2000.
- [6] Sensors and Integrated Microsystems Laboratory, “<https://uwaterloo.ca/sensors-integrated-microsystems-lab/research/hars>” 2018.
- [7] Microfabrication inspired by Lego, “<https://www.nanowerk.com/spotlight/spotid=32887.php>,” 2018.
- [8] E. Mehdizadeh, V. Kumar, and S. Pourkamali, “Sensitivity enhancement of lorentz force MEMS resonant magnetometers

- via internal thermal-piezoresistive amplification,” *IEEE Electron Device Letters*, vol. 35, pp. 268–270, Feb 2014.
- [9] A. Fruehling, R. Tung, A. Raman, and D. Peroulis, “In situ monitoring of dynamic bounce phenomena in RF MEMS switches,” *Journal of Micromechanics and Microengineering*, vol. 23, p. 115007, Nov 2013.
- [10] H. Hu, H. Cho, S. Somnath, A. F. Vakakis, and W. P. King, “Silicon nano-mechanical resonators fabricated by using tip-based nanofabrication,” *Nanotechnology*, vol. 25, p. 275301, Jul 2014.
- [11] R. Abdolvand, B. Bahreyni, J. E. Lee, and F. Nabki, “Micromachined resonators: A review,” *Micromachines*, vol. 7, p. 160, Sep 2016.
- [12] H. C. Nathanson, W. E. Newell, R. A. Wickstrom, and J. R. Davis, “The Resonant Gate Transistor,” *IEEE Transactions on Electron Devices*, vol. ED-14, pp. 117–133, Mar 1967.
- [13] H. Yamaguchi, “GaAs-based micro/nanomechanical resonators,” *Semiconductor Science and Technology*, vol. 32, p. 103003, Oct 2017.
- [14] R. Salut, C. Gesset, G. Martin, B. Assouar, P. Bergonzo, R. Boudot, O. Elmazria, and S. Ballandras, “Fabrication of a 3 GHz oscillator based on Nano-Carbon-Diamond-film-based guided wave resonators,” *Microelectronic Engineering*, vol. 112, pp. 133–138, Dec 2013.
- [15] E. A. Laird, F. Pei, W. Tang, G. A. Steele, and L. P. Kouwenhoven, “A high quality factor carbon nanotube mechanical resonator at 39 GHz,” *Nano Letters*, vol. 12, pp. 193–197, Jan 2012.

-
- [16] M. J. Wittbrodt, C. R. Steele, and S. Puria, “Developing a physical model of the human cochlea using microfabrication methods,” *Audiology and Neurotology*, vol. 11, no. 2, pp. 104–112, 2005.
- [17] S. Kim, W. J. Song, J. Jang, J. H. Jang, and H. Choi, “Mechanical frequency selectivity of an artificial basilar membrane using a beam array with narrow supports,” *Journal of Micromechanics and Microengineering*, vol. 23, p. 095018, Sep 2013.
- [18] J. Jang, S. Kim, D. J. Sly, S. J. O’Leary, and H. Choi, “MEMS piezoelectric artificial basilar membrane with passive frequency selectivity for short pulse width signal modulation,” *Sensors and Actuators, A: Physical*, vol. 203, pp. 6–10, Dec 2013.
- [19] S. Kim, W. J. Song, J. Jang, J. H. Jang, and H. Choi, “Characterization and modeling of an acoustic sensor using AlN thin-film for frequency selectivity,” *Electronic Materials Letters*, vol. 10, pp. 299–303, Jan 2014.
- [20] H. Shintaku, T. Nakagawa, D. Kitagawa, H. Tanujaya, S. Kawano, and J. Ito, “Development of piezoelectric acoustic sensor with frequency selectivity for artificial cochlea,” *Sensors and Actuators, A: Physical*, vol. 158, pp. 183–192, Mar 2010.
- [21] Y. Jung, J. H. Kwak, Y. H. Lee, W. D. Kim, and S. Hur, “Development of a multi-channel piezoelectric acoustic sensor based on an artificial basilar membrane,” *Sensors (Switzerland)*, vol. 14, pp. 117–128, Dec 2013.
- [22] H. Shintaku, T. Kobayashi, K. Zusho, H. Kotera, and S. Kawano, “Wide-range frequency selectivity in an acoustic

- sensor fabricated using a microbeam array with non-uniform thickness,” *Journal of Micromechanics and Microengineering*, vol. 23, p. 115014, Nov 2013.
- [23] Y. Ning, A. Mitchell, and R. Tait, “Fabrication of a silicon micromachined capacitive microphone using a dry-etch process,” *Sensors and Actuators A: Physical*, vol. 53, pp. 237–242, May 1996.
- [24] A. Torkkeli, O. Rusanen, J. Saarilahti, H. Seppä, H. Sipola, and J. Hietanen, “Capacitive microphone with low-stress polysilicon membrane and high-stress polysilicon backplate,” *Sensors and Actuators, A: Physical*, vol. 85, pp. 116–123, Aug 2000.
- [25] B. A. Ganji and B. Y. Majlis, “Design and fabrication of a new MEMS capacitive microphone using a perforated aluminum diaphragm,” *Sensors and Actuators, A: Physical*, vol. 149, pp. 29–37, Jan 2009.
- [26] Hearing Aids Market - Global Outlook and Forecast 2018-2023, “https://www.researchandmarkets.com/research/ddp82p/9_billion?w=12” 2018.
- [27] Microphone Market worth 1.81 Billion by 2020, “<https://www.marketsandmarkets.com/PressReleases/microphones.asp>,” 2018.
- [28] B. O. Olusany, K. J. Neumann, and J. E. Saunders, “La carga global de la deficiencia auditiva incapacitante: Una llamada a la acción,” *Bulletin of the World Health Organization*, vol. 92, pp. 367–373, May 2014.

-
- [29] World Health Organization, “Neglected Tropical Diseases, http://www.who.int/neglected_diseases/diseases/en/,” 2018.
- [30] M. K. Cosetti and S. B. Waltzman, “Cochlear implants: Current status and future potential,” *Expert Review of Medical Devices*, vol. 8, pp. 389–401, May 2011.
- [31] Y. Brand, P. Senn, M. Kompis, N. Dillier, and J. H. Allum, “Cochlear implantation in children and adults in Switzerland,” Feb 2014.
- [32] R. D. White and K. Grosh, “Microengineered hydromechanical cochlear model,” *Proceedings of the National Academy of Sciences of the United States of America*, vol. 102, pp. 1296–1301, Feb 2005.
- [33] E. H. Lin, M. Von Korff, D. Peterson, E. J. Ludman, P. Ciechanowski, and W. Katon, “Population targeting and durability of multimorbidity collaborative care management,” *American Journal of Managed Care*, vol. 20, pp. 887–893, Jul 2014.
- [34] S. J. Elliott and C. A. Shera, “The cochlea as a smart structure,” *Smart Materials and Structures*, vol. 21, p. 064001, Jun 2012.
- [35] A. Heredia, R. Ambrosio, M. Moreno, C. Zuñiga, A. Jiménez, K. Monfil, and J. D. La Hidalga, “Thin film membrane based on a-SiGe: B and MEMS technology for application in cochlear implants,” *Journal of Non-Crystalline Solids*, vol. 358, pp. 2331–2335, Sep 2012.
- [36] T. Xu, M. Bachman, F. G. Zeng, and G. P. Li, “Polymeric micro-cantilever array for auditory front-end processing,”

- Sensors and Actuators, A: Physical*, vol. 114, pp. 176–182, Sep 2004.
- [37] Y. Kim, J.-S. Kim, and G.-W. Kim, “A Novel Frequency Selectivity Approach Based on Travelling Wave Propagation in Mechanoluminescence Basilar Membrane for Artificial Cochlea,” *Scientific Reports*, vol. 8, no. 1, p. 12023, 2018.
- [38] M. Papila, R. T. Haftka, T. Nishida, and M. Sheplak, “Piezoresistive microphone design Pareto optimization: Tradeoff between sensitivity and noise floor,” *Journal of Microelectromechanical Systems*, vol. 15, pp. 1632–1643, Dec 2006.
- [39] M. L. Kuntzman, J. Gloria Lee, N. N. Hewa-Kasakarage, D. Kim, and N. A. Hall, “Micromachined piezoelectric microphones with in-plane directivity,” *Applied Physics Letters*, vol. 102, p. 054109, Feb 2013.
- [40] M. C. Killion, “Noise of ears and microphones,” *The Journal of the Acoustical Society of America*, vol. 59, pp. 424–433, Feb 1976.
- [41] J. H. Song, H. M. Gu, H. J. Park, and S. S. Lee, “Optical microphone based on a reflective micromirror diaphragm,” *Microwave and Optical Technology Letters*, vol. 48, pp. 707–709, Apr 2006.
- [42] T. Tajima, T. Nishiguchi, S. Chiba, A. Morita, M. Abe, K. Tanioka, N. Saito, and M. Esashi, “High-performance ultra-small single crystalline silicon microphone of an integrated structure,” *Microelectronic Engineering*, vol. 67-68, pp. 508–519, Jun 2003.

-
- [43] E. D. Munz, *Psychotherapie in der Psychiatrie*, vol. 36. Wiley-VCH Verlag & Co. KGaA, 2017.
- [44] C. Zhao, M. H. Montaseri, G. S. Wood, S. H. Pu, A. A. Seshia, and M. Kraft, “A review on coupled MEMS resonators for sensing applications utilizing mode localization,” *Sensors and Actuators, A: Physical*, vol. 249, pp. 93–111, Oct 2016.
- [45] H. Benaroya, N. Mark, and Han Seon, *Mechanical Vibration: Analysis, Uncertainties, and Control, Fourth Edition*. 2017.
- [46] J. A. Pelesko and D. H. Bernstein, *Modeling MEMS and NEMS*. Chapman & Hall/CRC, 2003.
- [47] S. S. Rao, *Vibration of Continuous Systems (2007)*. Wiley, 2007.
- [48] A. P. Stebner, C. E. Wehrenberg, B. Li, G. C. Randall, K. K. John, G. A. Hudish, B. R. Maddox, M. Farrell, H. S. Park, B. A. Remington, M. Ortiz, and G. Ravichandran, “Strength of tantalum shocked at ultrahigh pressures,” *Materials Science and Engineering A*, vol. 732, pp. 220–227, Aug 2018.
- [49] Y. Liu, C. Bao, D. Wismeijer, and G. Wu, “The physicochemical/biological properties of porous tantalum and the potential surface modification techniques to improve its clinical application in dental implantology,” Apr 2015.
- [50] Craig, Bruce D, D. S. Anderson, B. D. Craig, and a.S.M. International, *Handbook of corrosion data*. ASM International, 1995.
- [51] F. G. Cox, “Anti-Corrosion Methods and Materials CORROSION RESISTANCE OF TANTALUM: Applications in the Chemical Industry For Authors Applications in the

- Chemical Industry,” *Anti-Corrosion Methods and Materials*, vol. 7, no. 08, pp. 69–7405, 1960.
- [52] M. M. Biener, J. Biener, A. M. Hodge, and A. V. Hamza, “Dislocation nucleation in bcc Ta single crystals studied by nanoindentation,” *Physical Review B - Condensed Matter and Materials Physics*, vol. 76, no. 16, pp. 1–6, 2007.
- [53] S.-Y. Jang, S.-M. Lee, and H.-K. Baik, “Tantalum and niobium as a diffusion barrier between copper and silicon,” *Journal of Materials Science: Materials in Electronics*, vol. 7, pp. 271–278, Aug 1996.
- [54] H. Ono, T. Nakano, and T. Ohta, “Diffusion barrier effects of transition metals for Cu/M/Si multilayers (M=Cr, Ti, Nb, Mo, Ta, W),” *Applied Physics Letters*, vol. 64, pp. 1511–1513, Mar 1994.
- [55] K. Holloway, P. M. Fryer, C. Cabral, J. M. Harper, P. J. Bailey, and K. H. Kelleher, “Tantalum as a diffusion barrier between copper and silicon: Failure mechanism and effect of nitrogen additions,” *Journal of Applied Physics*, vol. 71, pp. 5433–5444, Jun 1992.
- [56] S. Myers, J. Lin, R. M. Souza, W. D. Sproul, and J. J. Moore, “The β to α phase transition of tantalum coatings deposited by modulated pulsed power magnetron sputtering,” *Surface and Coatings Technology*, vol. 214, pp. 38–45, Jan 2013.
- [57] Y. Iimura, “Low-stress tantalum absorbers deposited by sputtering for x-ray masks,” *Journal of Vacuum Science & Technology B: Microelectronics and Nanometer Structures*, vol. 7, p. 1680, Nov 1989.

-
- [58] T. Schmitz, C. Hertl, E. Werner, U. Gbureck, J. Groll, and C. Moseke, “Oxygen diffusion hardening of tantalum coatings on cp-titanium for biomedical applications,” *Surface and Coatings Technology*, vol. 216, pp. 46–51, Feb 2013.
- [59] R. Latif, E. Mastropaolo, A. Bunting, R. Cheung, T. Koickal, A. Hamilton, M. Newton, and L. Smith, “Low frequency tantalum electromechanical systems for biomimetical applications,” *Journal of Vacuum Science & Technology B, Nanotechnology and Microelectronics: Materials, Processing, Measurement, and Phenomena*, vol. 29, p. 06FE05, Nov 2011.
- [60] E. Mastropaolo, R. Latif, E. Grady, and R. Cheung, “Control of stress in tantalum thin films for the fabrication of 3D MEMS structures,” *Journal of Vacuum Science & Technology B: Microelectronics and Nanometer Structures*, vol. 31, p. 06FD02, Oct 2013.
- [61] C. Lee, X. Wei, J. W. Kysar, and J. Hone, “Measurement of the elastic properties and intrinsic strength of monolayer graphene,” *Science*, vol. 321, pp. 385–388, Jul 2008.
- [62] A. Castellanos-Gomez, V. Singh, H. S. Van Der Zant, and G. A. Steele, “Mechanics of freely-suspended ultrathin layered materials,” *Annalen der Physik*, vol. 527, pp. 27–44, Jan 2015.
- [63] S. Timoshenko, D. H. Young, and W. J. Weaver, *Vibration problems in engineering*. Wiley, 1974.
- [64] F. Holzweissig, A. W. Leissa, *Vibration of Plates. (Nasa Sp-160). VII + 353 S. m. Fig. Washington 1969. Office of Technology Utilization National Aeronautics and Space Administration. Preis brosch. \$ 3.50*, vol. 51. Acoustical

- Society of America through the American Institute of Physics, 1971.
- [65] W. C. Chuang, H. L. Lee, P. Z. Chang, and Y. C. Hu, “Review on the modeling of electrostatic MEMS,” *Sensors*, vol. 10, no. 6, pp. 6149–6171, 2010.
- [66] Q. Zhou and A. Zettl, “Electrostatic graphene loudspeaker,” *Applied Physics Letters*, vol. 102, p. 223109, Jun 2013.
- [67] A. Balan, C. C. Chien, R. Engelke, and M. Drndic, “Suspended Solid-state Membranes on Glass Chips with Sub 1-pF Capacitance for Biomolecule Sensing Applications,” *Scientific Reports*, vol. 5, p. 17775, Nov 2015.
- [68] D. Todorović, A. Matković, M. Milićević, D. Jovanović, R. Gajić, I. Salom, and M. Spasenović, “Multilayer graphene condenser microphone,” *2D Materials*, vol. 2, p. 045013, Nov 2015.
- [69] M. Younis, *Sensing and Actuation Actuation in MEMS*, vol. 20. Springer US, 2011.
- [70] W. K. Schomburg, *Introduction to Microsystem Design*, vol. 1 of *RWTHedition*. Berlin, Heidelberg: Springer Berlin Heidelberg, 2011.
- [71] S. E. Zhu, R. Shabani, J. Rho, Y. Kim, B. H. Hong, J. H. Ahn, and H. J. Cho, “Graphene-based bimorph microactuators,” *Nano Letters*, vol. 11, pp. 977–981, Mar 2011.
- [72] S. Pal and H. Xie, “Fabrication of robust electrothermal MEMS devices using aluminum-tungsten bimorphs and polyimide thermal isolation,” *Journal of Micromechanics and Microengineering*, vol. 22, p. 115036, Nov 2012.

-
- [73] A. Al-mashaal, G. Wood, E. Mastropaolo, and R. Cheung, “Electrostatically driven long-microbeams for low-frequency applications,” *Electronics Letters*, vol. 54, pp. 372–374, Mar 2018.
- [74] D. Depla and B. R. Braeckman, “Quantitative correlation between intrinsic stress and microstructure of thin films,” *Thin Solid Films*, vol. 604, pp. 90–93, Apr 2016.
- [75] G. Abadias, E. Chason, J. Keckes, M. Sebastiani, G. B. Thompson, E. Barthel, G. L. Doll, C. E. Murray, C. H. Stoessel, and L. Martinu, “Review Article: Stress in thin films and coatings: Current status, challenges, and prospects,” *Journal of Vacuum Science & Technology A: Vacuum, Surfaces, and Films*, vol. 36, p. 020801, Mar 2018.
- [76] Y. Pauleau, “Generation and evolution of residual stresses in physical vapour-deposited thin films,” *Vacuum*, vol. 61, pp. 175–181, May 2001.
- [77] G. C. Janssen, “Stress and strain in polycrystalline thin films,” *Thin Solid Films*, vol. 515, pp. 6654–6664, Jun 2007.
- [78] G. Guisbiers, O. Van Overschelde, M. Wautelet, P. Leclerc, and R. Lazzaroni, “Fractal dimension, growth mode and residual stress of metal thin films,” *Journal of Physics D: Applied Physics*, vol. 40, pp. 1077–1079, Feb 2007.
- [79] Q. L. Ye and S. J. Yu, “Growth mechanism and edge effect of buckling patterns in elastic films deposited on stiff substrates,” *Philosophical Magazine Letters*, vol. 93, pp. 710–718, Dec 2013.
- [80] L. Liu, Y. Wang, and H. Gong, “Annealing effects of tantalum

- films on Si and SiO₂/Si substrates in various vacuums,” *Journal of Applied Physics*, vol. 90, pp. 416–420, Jul 2001.
- [81] L. Liu, H. Gong, Y. Wang, J. Wang, A. T. Wee, and R. Liu, “Annealing effects of tantalum thin films sputtered on [001] silicon substrate,” *Materials Science and Engineering C*, vol. 16, pp. 85–89, Oct 2001.
- [82] R. Hübner, M. Hecker, N. Mattern, V. Hoffmann, K. Wetzig, H. J. Engelmann, and E. Zschech, “Comparison of the annealing behavior of thin Ta films deposited onto Si and SiO₂ substrates,” in *Analytical and Bioanalytical Chemistry*, vol. 379, pp. 568–575, Springer-Verlag, Jun 2004.
- [83] M. H. Cheng, T. C. Cheng, W. J. Huang, M. N. Chang, and M. K. Chung, “Influence of oxygen diffusion on residual stress for tantalum thin films,” *Journal of Vacuum Science & Technology B: Microelectronics and Nanometer Structures*, vol. 25, p. 147, Jan 2007.
- [84] L. A. Clevenger, A. Mutscheller, J. M. Harper, C. Cabral, and K. Barmak, “The relationship between deposition conditions, the beta to alpha phase transformation, and stress relaxation in tantalum thin films,” *Journal of Applied Physics*, vol. 72, pp. 4918–4924, Nov 1992.
- [85] Y. Jin, J. Y. Song, S. H. Jeong, J. W. Kim, T. G. Lee, J. H. Kim, and J. Hahn, “Thermal oxidation mechanism and stress evolution In Ta thin films,” *Journal of Materials Research*, vol. 25, pp. 1080–1086, Jun 2010.
- [86] J. Lin, J. J. Moore, W. D. Sproul, S. L. Lee, and J. Wang, “Effect of negative substrate bias on the structure and properties of Ta coatings deposited using modulated pulse

- power magnetron sputtering,” in *IEEE Transactions on Plasma Science*, vol. 38, pp. 3071–3078, Nov 2010.
- [87] D. W. Hoffman and J. A. Thornton, “Internal stresses in Cr, Mo, Ta, and Pt films deposited by sputtering from a planar magnetron source,” *Journal of Vacuum Science and Technology*, vol. 20, pp. 355–358, Mar 1982.
- [88] J. Peng, V. Ji, W. Seiler, A. Tomescu, A. Levesque, and A. Bouteville, “Residual stress gradient analysis by the GIXRD method on CVD tantalum thin films,” *Surface and Coatings Technology*, vol. 200, pp. 2738–2743, Jan 2006.
- [89] G. Guisbiers, E. Herth, L. Buchaillot, and T. Pardoen, “Fracture toughness, hardness, and Young’s modulus of tantalum nanocrystalline films,” *Applied Physics Letters*, vol. 97, p. 143115, Oct 2010.
- [90] A. A. Navid and A. M. Hodge, “Controllable residual stresses in sputtered nanostructured alpha-tantalum,” *Scripta Materialia*, vol. 63, pp. 867–870, Oct 2010.
- [91] B. L. French and J. C. Bilello, “In situ observations of the real-time stress-evolution and delamination of thin Ta films on Si(100),” *Thin Solid Films*, vol. 446, pp. 91–98, Jan 2004.
- [92] J. A. Thornton and D. W. Hoffman, “Internal stresses in titanium, nickel, molybdenum, and tantalum films deposited by cylindrical magnetron sputtering,” *Journal of Vacuum Science and Technology*, vol. 14, pp. 164–168, Jan 1977.
- [93] P. Catania, R. A. Roy, and J. J. Cuomo, “Phase formation and microstructure changes in tantalum thin films induced by bias sputtering,” *Journal of Applied Physics*, vol. 74, pp. 1008–1014, Jul 1993.

-
- [94] R. W. Hoffman, “Stresses in thin films: The relevance of grain boundaries and impurities,” *Thin Solid Films*, vol. 34, pp. 185–190, May 1976.
- [95] H. Windischmann, “Intrinsic Stress in Sputter-Deposited Thin Films,” *Critical Reviews in Solid State and Materials Sciences*, vol. 17, pp. 547–596, Jan 1992.
- [96] T. Yoshihara and K. Suzuki, “Variation of internal stresses in sputtered Ta films,” *Journal of Vacuum Science & Technology B: Microelectronics and Nanometer Structures*, vol. 11, p. 301, Mar 1993.
- [97] K. Dahmen, M. Giesen, J. Ikonov, K. Starbova, and H. Ibach, “Steady-state surface stress induced in noble gas sputtering,” *Thin Solid Films*, vol. 428, pp. 6–10, Mar 2003.
- [98] J. Kalambe and R. Patrikar, “Design, fabrication, and characterization of electrostatically actuated microcantilever sensor for temperature detection,” *IEEE Sensors Journal*, vol. 15, pp. 1595–1601, Mar 2015.
- [99] L. Medina, R. Gilat, B. Ilic, and S. Krylov, “Experimental investigation of the snap-through buckling of electrostatically actuated initially curved pre-stressed micro beams,” *Sensors and Actuators, A: Physical*, vol. 220, pp. 323–332, Dec 2014.
- [100] J. J. Yao, “RF MEMS from a device perspective,” *Journal of Micromechanics and Microengineering*, vol. 10, pp. R9–R38, Dec 2000.
- [101] Z. Zhou, Y. Zhou, Y. Cao, and H. Mao, “Residual strain of a Cr film characterized by micromachined beams,” *Measurement Science and Technology*, vol. 18, pp. 3399–3402, Nov 2007.

-
- [102] W. Fang, C. H. Lee, and H. H. Hu, “On the buckling behavior of micromachined beams,” *Journal of Micromechanics and Microengineering*, vol. 9, pp. 236–244, Sep 1999.
- [103] R. Schönggrundner, R. Treml, T. Antretter, D. Kozic, W. Ecker, D. Kiener, and R. Brunner, “Critical assessment of the determination of residual stress profiles in thin films by means of the ion beam layer removal method,” *Thin Solid Films*, vol. 564, pp. 321–330, Aug 2014.
- [104] W. Fang and J. A. Wickert, “Determining mean and gradient residual stresses in thin films using micromachined cantilevers,” *Journal of Micromechanics and Microengineering*, vol. 6, pp. 301–309, Sep 1996.
- [105] W. S. Su, S. T. Lee, C. Y. Lin, M. C. Yip, M. S. Tsai, and W. Fang, “Control the Shape of Buckling Micromachined Beam using Plasma Chemistry Bonding Technology,” *Japanese Journal of Applied Physics*, vol. 45, pp. 8479–8483, Oct 2006.
- [106] E. Iwase, P.-C. Hui, D. Woolf, A. W. Rodriguez, S. G. Johnson, F. Capasso, and M. Lončar, “Control of buckling in large micromembranes using engineered support structures,” *Journal of Micromechanics and Microengineering*, vol. 22, p. 065028, Jun 2012.
- [107] F. Fachin, S. A. Nikles, J. Dugundji, and B. L. Wardle, “Analytical extraction of residual stresses and gradients in MEMS structures with application to CMOS-layered materials,” *Journal of Micromechanics and Microengineering*, vol. 21, p. 095017, Sep 2011.
- [108] D. Zhang and J. Chu, “Mechanical characterization of

- post-buckled micro-bridge beams by micro-tensile testing,” *Microsystem Technologies*, vol. 16, pp. 375–380, Nov 2010.
- [109] Y. T. Yu, W. Z. Yuan, D. Y. Qiao, and Q. Liang, “Evaluation of residual stresses in thin films by critical buckling observation of circular microstructures and finite element method,” *Thin Solid Films*, vol. 516, pp. 4070–4075, Apr 2008.
- [110] G. Szulczewski, S. Sanvito, and M. Coey, *A spin of their own*, vol. 8. CRC Press, 2009.
- [111] M. W. Pruessner, T. T. King, D. P. Kelly, R. Grover, L. C. Calhoun, and R. Ghodssi, “Mechanical property measurement of InP-based MEMS for optical communications,” *Sensors and Actuators, A: Physical*, vol. 105, pp. 190–200, Jul 2003.
- [112] L. B. Freund and S. Suresh, *Thin Film Materials*. Cambridge University Press, 2004.
- [113] D. Peroulis, S. P. Pacheco, K. Sarabandi, and L. P. Katehi, “Electromechanical considerations in developing low-voltage RF MEMS switches,” *IEEE Transactions on Microwave Theory and Techniques*, vol. 51, pp. 259–270, Jan 2003.
- [114] A. Garg, J. Small, X. Liu, A. K. Mahapatro, and D. Peroulis, “Impact of sacrificial layer type on thin-film metal residual stress,” 2009.
- [115] M. J. Kobrinsky, E. R. Deutsch, and S. D. Senturia, “Effect of support compliance and residual stress on the shape of doubly supported surface-micromachined beams,” *Journal of Microelectromechanical Systems*, vol. 9, pp. 361–369, Sep 2000.
- [116] T.-J. Peters and M. Tichem, “Fabrication and characterization of suspended beam structures for SiO₂

- photonic MEMS,” *Journal of Micromechanics and Microengineering*, vol. 25, p. 105003, Oct 2015.
- [117] W. Fang and J. A. Wickert, “Post buckling of micromachined beams,” *Journal of Micromechanics and Microengineering*, vol. 4, pp. 116–122, Sep 1994.
- [118] Z. Zhang, F. Chen, Z. Zhang, and H. Hua, “Vibration analysis of non-uniform Timoshenko beams coupled with flexible attachments and multiple discontinuities,” *International Journal of Mechanical Sciences*, vol. 80, pp. 131–143, 2014.
- [119] S. Krylov and N. Dick, “Dynamic stability of electrostatically actuated initially curved shallow micro beams,” *Continuum Mechanics and Thermodynamics*, vol. 22, pp. 445–468, Sep 2010.
- [120] S. Chowdhury, M. Ahmadi, and W. C. Miller, “Design of a MEMS acoustical beamforming sensor microarray,” *IEEE Sensors Journal*, vol. 2, pp. 617–627, Dec 2002.
- [121] S. Walser, C. Siegel, M. Winter, G. Feiertag, M. Loibl, and A. Leidl, “MEMS microphones with narrow sensitivity distribution,” *Sensors and Actuators, A: Physical*, vol. 247, pp. 663–670, Aug 2016.
- [122] H. Li, C. Tian, and Z. D. Deng, “Energy harvesting from low frequency applications using piezoelectric materials,” *Applied Physics Reviews*, vol. 1, p. 041301, Dec 2014.
- [123] H. Liu and W. T. Pike, “A micromachined angular-acceleration sensor for geophysical applications,” *Applied Physics Letters*, vol. 109, p. 173506, Oct 2016.
- [124] A. Al-Mashaal, A. Bunting, and R. Cheung, “Evaluation

- of residual stress in sputtered tantalum thin-film,” *Applied Surface Science*, vol. 371, pp. 571–575, 2016.
- [125] A. Al-Mashaal, E. Mastropaolo, A. Bunting, C. Dunare, and R. Cheung, “Fabrication and characterisation of suspended microstructures of tantalum,” *Journal of Micromechanics and Microengineering*, vol. 27, p. 015020, Jan 2017.
- [126] B. Lindroos, A. Lehto, T. Motooka, and M. Tilli, *Handbook of Silicon Based MEMS Materials and Technologies*. William Andrew/Elsevier, 2010.
- [127] V. Cimalla, F. Niebelschütz, K. Tonisch, C. Foerster, K. Brueckner, I. Cimalla, T. Friedrich, J. Pezoldt, R. Stephan, M. Hein, and O. Ambacher, “Nanoelectromechanical devices for sensing applications,” *Sensors and Actuators, B: Chemical*, vol. 126, pp. 24–34, Sep 2007.
- [128] S. Pamidighantam, R. Puers, K. Baert, and H. A. Tilmans, “Pull-in voltage analysis of electrostatically actuated beam structures with fixed-fixed and fixed-free end conditions,” *Journal of Micromechanics and Microengineering*, vol. 12, pp. 458–464, Jul 2002.
- [129] M. L. De Laat, H. H. Píñerez Garza, J. L. Herder, and M. K. Ghatkesar, “A review on in situ stiffness adjustment methods in MEMS,” *Journal of Micromechanics and Microengineering*, vol. 26, p. 063001, Jun 2016.
- [130] A. M. Elshurafa, K. Khirallah, H. H. Tawfik, A. Emira, A. K. Abdel Aziz, and S. M. Sedky, “Nonlinear dynamics of spring softening and hardening in folded-mems comb drive resonators,” *Journal of Microelectromechanical Systems*, vol. 20, pp. 943–958, Aug 2011.

-
- [131] H. C. Lee, W.-W. Liu, S.-P. Chai, A. R. Mohamed, A. Aziz, C.-S. Khe, N. S. Hidayah, and U. Hashim, "Review of the synthesis, transfer, characterization and growth mechanisms of single and multilayer graphene," *RSC Advances*, vol. 7, pp. 15644–15693, Mar 2017.
- [132] X. Wan, Y. Huang, and Y. Chen, "Focusing on energy and optoelectronic applications: A journey for graphene and graphene oxide at large scale," *Accounts of Chemical Research*, vol. 45, pp. 598–607, Apr 2012.
- [133] H. C. Lee, W.-W. Liu, S.-P. Chai, A. R. Mohamed, C. W. Lai, C.-S. Khe, C. Voon, U. Hashim, and N. Hidayah, "Synthesis of Single-layer Graphene: A Review of Recent Development," *Procedia Chemistry*, vol. 19, pp. 916–921, Jan 2016.
- [134] J. H. Warner, F. Schaffel, M. Rummeli, and A. Bachmatiuk, *Graphene : fundamentals and emergent applications*, vol. 17. Elsevier, 2013.
- [135] Z. Q. Li, E. A. Henriksen, Z. Jiang, Z. Hao, M. C. Martin, P. Kim, H. L. Stormer, and D. N. Basov, "Dirac charge dynamics in graphene by infrared spectroscopy," *Nature Physics*, vol. 4, pp. 532–535, Jul 2008.
- [136] J. Wang, F. Ma, W. Liang, and M. Sun, "Electrical properties and applications of graphene, hexagonal boron nitride (h-BN), and graphene/h-BN heterostructures," *Materials Today Physics*, vol. 2, pp. 6–34, Sep 2017.
- [137] M. Orlita, C. Faugeras, P. Plochocka, P. Neugebauer, G. Martinez, D. K. Maude, A. L. Barra, M. Sprinkle, C. Berger, W. A. De Heer, and M. Potemski, "Approaching the dirac point in high-mobility multilayer epitaxial

- graphene,” *Physical Review Letters*, vol. 101, p. 267601, Dec 2008.
- [138] C. N. Lau, W. Bao, and J. Velasco, “Properties of suspended graphene membranes,” *Materials Today*, vol. 15, pp. 238–245, Jun 2012.
- [139] A. H. C. Neto, F. Guinea, N. M. R. Peres, K. S. Novoselov, and A. K. Geim, “The electronic properties of graphene,” *Reviews of Modern Physics*, vol. 81, pp. 109–162, Jan 2007.
- [140] W. S. Lee and S. S. Lee, “Piezoelectric microphone built on circular diaphragm,” *Sensors and Actuators, A: Physical*, vol. 144, pp. 367–373, Jun 2008.
- [141] I. W. Frank, D. M. Tanenbaum, A. M. van der Zande, and P. L. McEuen, “Mechanical properties of suspended graphene sheets,” *Journal of Vacuum Science & Technology B: Microelectronics and Nanometer Structures*, vol. 25, no. 6, p. 2558, 2007.
- [142] H. Tomori, A. Kanda, H. Goto, Y. Ootuka, K. Tsukagoshi, S. Moriyama, E. Watanabe, and D. Tsuya, “Introducing nonuniform strain to graphene using dielectric nanopillars,” *Applied Physics Express*, vol. 4, p. 075102, Jun 2011.
- [143] A. A. Balandin, S. Ghosh, W. Bao, I. Calizo, D. Teweldebrhan, F. Miao, and C. N. Lau, “Superior thermal conductivity of single-layer graphene,” *Nano Letters*, vol. 8, pp. 902–907, Mar 2008.
- [144] K. S. Novoselov, A. K. Geim, S. V. Morozov, D. Jiang, Y. Zhang, S. V. Dubonos, I. V. Grigorieva, and A. A. Firsov, “Electric field in atomically thin carbon films,” *Science*, vol. 306, pp. 666–669, Oct 2004.

-
- [145] P. Avouris and C. Dimitrakopoulos, “Graphene: Synthesis and applications,” *Materials Today*, vol. 15, pp. 86–97, Mar 2012.
- [146] K. V. Emtsev, A. Bostwick, K. Horn, J. Jobst, G. L. Kellogg, L. Ley, J. L. McChesney, T. Ohta, S. A. Reshanov, J. Röhl, E. Rotenberg, A. K. Schmid, D. Waldmann, H. B. Weber, and T. Seyller, “Towards wafer-size graphene layers by atmospheric pressure graphitization of silicon carbide,” *Nature Materials*, vol. 8, pp. 203–207, Mar 2009.
- [147] D. A. Long, *Introductory Raman Spectroscopy*. John R. Ferraro, Kazuo Nakamoto and Chris W. Brown. Academic Press, Amsterdam, Second Edition, 2003. xiii + 434, vol. 36. Academic Press, 2005.
- [148] L. M. Malard, M. A. Pimenta, G. Dresselhaus, and M. S. Dresselhaus, “Raman spectroscopy in graphene,” *Physics Reports*, vol. 473, pp. 51–87, Apr 2009.
- [149] M. Wall, “The Raman Spectroscopy of Graphene and the Determination of Layer Thickness,” *Thermo scientific*, p. 5, 2011.
- [150] H. Wang and G. Yu, “Direct CVD Graphene Growth on Semiconductors and Dielectrics for Transfer-Free Device Fabrication,” *Advanced Materials*, vol. 28, pp. 4956–4975, Jul 2016.
- [151] A. V. Zaretski and D. J. Lipomi, “Processes for non-destructive transfer of graphene: widening the bottleneck for industrial scale production,” *Nanoscale*, vol. 7, pp. 9963–9969, May 2015.
- [152] Y. Chen, X. L. Gong, and J. G. Gai, “Progress and Challenges

- in Transfer of Large-Area Graphene Films,” *Advanced Science*, vol. 3, p. 1500343, Aug 2016.
- [153] J. S. Bunch, A. M. Van Der Zande, S. S. Verbridge, I. W. Frank, D. M. Tanenbaum, J. M. Parpia, H. G. Craighead, and P. L. McEuen, “Electromechanical resonators from graphene sheets,” *Science*, vol. 315, pp. 490–493, Jan 2007.
- [154] D. Davidovikj, J. J. Slim, S. J. Cartamil-Bueno, H. S. J. Van Der Zant, P. G. Steeneken, and W. J. Venstra, “Visualizing the Motion of Graphene Nanodrums,” *Nano Letters*, vol. 16, pp. 2768–2773, Apr 2016.
- [155] R. De Alba, F. Massel, I. R. Storch, T. S. Abhilash, A. Hui, P. L. McEuen, H. G. Craighead, and J. M. Parpia, “Tunable phonon-cavity coupling in graphene membranes,” *Nature Nanotechnology*, vol. 11, pp. 741–746, Jun 2016.
- [156] C. Chen, S. Lee, V. V. Deshpande, G. H. Lee, M. Lekas, K. Shepard, and J. Hone, “Graphene mechanical oscillators with tunable frequency,” *Nature Nanotechnology*, vol. 8, pp. 923–927, Nov 2013.
- [157] C. Chen, S. Rosenblatt, K. I. Bolotin, W. Kalb, P. Kim, I. Kymissis, H. L. Stormer, T. F. Heinz, and J. Hone, “Performance of monolayer graphene nanomechanical resonators with electrical readout,” *Nature Nanotechnology*, vol. 4, pp. 861–867, Dec 2009.
- [158] R. A. Barton, B. Ilic, A. M. Van Der Zande, W. S. Whitney, P. L. McEuen, J. M. Parpia, and H. G. Craighead, “High, size-dependent quality factor in an array of graphene mechanical resonators,” *Nano Letters*, vol. 11, pp. 1232–1236, Mar 2011.

-
- [159] P. KanJanaboos, X. M. Lin, J. E. Sader, S. M. Rupich, H. M. Jaeger, and J. R. Guest, “Self-assembled nanoparticle drumhead resonators,” *Nano Letters*, vol. 13, pp. 2158–2162, May 2013.
- [160] H. Schlicke, C. J. Schröter, and T. Vossmeier, “Electrostatically driven drumhead resonators based on freestanding membranes of cross-linked gold nanoparticles,” *Nanoscale*, vol. 8, pp. 15880–15887, Sep 2016.
- [161] X. Zhuang, A. Nikoozadeh, M. A. Beasley, G. G. Yaralioglu, B. T. Khuri-Yakub, and B. L. Pruitt, “Biocompatible coatings for CMUTs in a harsh, aqueous environment,” *Journal of Micromechanics and Microengineering*, vol. 17, pp. 994–1001, May 2007.
- [162] Y. Zhou and F. Amirouche, “Study of fluid damping effects on resonant frequency of an electromagnetically actuated valveless micropump,” *International Journal of Advanced Manufacturing Technology*, vol. 45, pp. 1187–1196, Dec 2009.
- [163] B. Vasić, M. M. Jakovljević, G. Isić, and R. Gajić, “Tunable metamaterials based on split ring resonators and doped graphene,” *Applied Physics Letters*, vol. 103, p. 011102, Jul 2013.
- [164] G. Liang, X. Hu, X. Yu, Y. Shen, L. H. Li, A. G. Davies, E. H. Linfield, H. K. Liang, Y. Zhang, S. F. Yu, and Q. J. Wang, “Integrated Terahertz Graphene Modulator with 100% Modulation Depth,” *ACS Photonics*, vol. 2, pp. 1559–1566, Nov 2015.
- [165] E. Mastropaolo, R. Latif, T. Koickal, A. Hamilton, R. Cheung, M. Newton, and L. Smith, “Bimaterial electromechanical

- systems for a biomimetical acoustic sensor,” *Journal of Vacuum Science & Technology B, Nanotechnology and Microelectronics: Materials, Processing, Measurement, and Phenomena*, vol. 30, p. 06FD01, Nov 2012.
- [166] S. Lee, C. Chen, V. V. Deshpande, G. H. Lee, I. Lee, M. Lekas, A. Gondarenko, Y. J. Yu, K. Shepard, P. Kim, and J. Hone, “Electrically integrated SU-8 clamped graphene drum resonators for strain engineering,” *Applied Physics Letters*, vol. 102, p. 153101, Apr 2013.